NORTHWESTERN UNIVERSITY

Advancing Melanin Structure and Function through Synthesis and Biomedical Application

A DISSERTATION

SUBMITTED TO THE GRADUATE SCHOOL
IN PARTIAL FULFILLMENT OF THE REQUIREMENTS

for the degree

DOCTOR OF PHILOSOPHY

Field of Chemistry

By

Naneki C. McCallum

EVANSTON, ILLINOIS

March 2021

Abstract

Melanin is a functional biopolymer most commonly associated with human skin pigmentation, where it serves as a radiation protection agent, shielding us from the harmful effects of UV radiation. However, melanin is also present in human ears, eyes, hair, and brains, serving a variety of functions. In fact, melanin has seemingly countless functions in the natural world, and is present in almost every type of organism on Earth. From bright colors found in bird feathers, to black fungal cell walls, melanin production has evolved as an ornamental and protective biomaterial capable of toxin adsorption, metal chelation, thermoregulation, radiation protection, and more.

Inspired by the possibilities of synthetic melanin constructs as functional biomaterials, we sought to synthesize, characterize, and test artificial analogues of melanin, using new and existing chemistries, and apply them as protection and coloration agents. We created a library of analogues of eumelanin, the common type of melanin in humans, with not only spherical but also rod-like morphology, mimicking a structure found in birds. These were biocompatible with human skin cells, despite having such drastically different morphologies than the natural system. We also synthesized mimics of fungal allomelanins which are chemically distinct from human melanins and showed that these allomelanins are biocompatible with human cells and can protect them from UV radiation. In an even more unusual application, we synthesized various morphologies of allomelanin particles with intrinsic and induced porosity, applied them as fabric coatings, and showed that they can adsorb harmful toxins which can irritate the skin, adding another approach to skin protection through protective clothing.

Melanin mimics was also tested to determine their use as artificial tanning and radiation protection agents, exploring monolayer cell culture, 3D reconstructed skin mimics, and intact skin.

The materials minimized the harmful effects of UV radiation when applied topically to human skin, and they also showed promise for mitigating the effects of UV and chemical injury in mice.

This work highlights the possibilities of artificial melanins as biocompatible, nature-inspired materials for skin protection from radiation and toxins, and paves a pathway for further investigation into melanin for a variety of applications.

Acknowledgement

First and foremost, I would like to thank my incredible advisor, Prof. Nathan Gianneschi, without whom I would not be here. I am thankful for the opportunity to work with Nathan not only in San Diego at UCSD but also at Northwestern. It has been the opportunity of my life to learn so much about chemistry, biochemistry, and materials science, and to be supported in all my endeavors and curiosities. Nathan is not only a brilliant scientist, but a superb human and friend, and I don't think I would have made it through graduate school without him. I will miss our Christmas parties, lab BBQs, camping trips, MURI meetings, and the entire Gianneschi Lab experience. I would also like to thank my committee members, Prof. Samuel Stupp and Prof. Milan Mrksich. Thank you also to Prof. William Dichtel who served on my preliminary committee at Northwestern.

I would also like to thank all my amazing collaborators throughout the years. Thank you to Prof. Bethany Perez-White for teaching me everything I know about keratinocytes and skin. Thank you to Prof. Kurt Lu for helping us broaden the scope of our melanin material applications in skin and for working so hard with us to apply for funding for further studies.

A big thank you to the Naval Research Laboratory, specifically Dr. Zheng Wang and Dr. Brandy White for assistance with fungal melanin and toxin studies. Thank you to Dr. Tristan Clemons, Dr. Steven Weigand, Prof. Samuel Stupp, and everyone at Argonne National Lab for their fantastic work on the complex SAXS experiments. Thank you to Florencia Son and Prof. Omar Farha for the porosity and gas measurements. I would also like to thank my whole MURI team- Prof. Matt Shawkey, Prof. Dimitri Deheyn, Prof. Michael Burkart, Prof. Jeffrey Rinehart, Prof. Ali Dhinojwala, and Prof. Arthi Jayaraman. Our twice-monthly meetings and thoughtful

discussions have taught me more than I could ever imagine. I would also like to graciously acknowledge support from the Air Force Office of Scientific Research through a MURI grant (FA9550-18-1-0142), and supplemental grant (FA9550-18-1-0477).

I would also like to thank my lab members for their collaborations, advice, knowledge, and friendships. Dr. Matthew Thompson is the backbone of the lab and I could not have survived without his guidance, chemical intuition, and wonderful Canadian spirit. He is the epitome of kindness as well as one of the smartest and most genuinely curious people I have ever known. Matt also plans the most amazing camping trips! I am also very thankful to all my other fantastic colleagues-turned-friends for this incredible journey- Dr. María Proetto for teaching me so much about cells and biochemistry and being a great friend, Dr. Ziying Hu for teaching me so many new techniques and for always putting a smile on my face in and out of the lab, Xuhao Zhou for being a fantastic close collaborator, Dr. Wei Cao for allowing our collaboration to flourish and for working with me on so many interesting melanin projects, Dr. Claudia Battistella for all the great collaborations and fun times, Zofia Siwicka for being a great bench neighbor, and for serving as the major catalyst for my exploration into porosity, Dr. Karthik Gnanasekaran for all his help on TEM imaging and MATLAB skills, Dr. Chris Forman for his assistance on everything under the sun, and invitingly cheery disposition, and Dr. Andrea Carlini for always making me laugh, and for great advice about chemistry and everything else. Lastly, thank you to all the other truly supportive and helpful past and present lab members and friends- Steven Nguyen, Swagat Sahu, Lisa Adamiak, Or Berger, and countless others not named here- all amazing people who have supported me at one time or another.

In addition, I would not have been able to perform this great work without the unbelievably generous and knowledgeable staff members at Northwestern. I thank BioCryo staff members Dr. Reiner Bleher, Eric Roth, and Charlene Wilke for assistance in electron microscopy training and sample prep, and for their incredible kindness and patience. Thank you to Dr. Jessica Hornick in the Biological Imaging Facility for her positive attitude, stellar training, and wealth of knowledge on everything related to light microscopy. I'd also like to thank Dr. Tirzah Abbott for training and assistance on everything SEM related, and for being such a pleasure to work with. Lastly, I must acknowledge Prof. Yeeseon Kwon from the NU Music Academy for her incredible kindness, patience, and passion, and for teaching me an entirely new language of thought.

It is also essential to mention all the people who came before and paved the way for my success in graduate school. Prof. Gary Carroll was my chemistry instructor at Santa Barbara City College, and the first person who believed in me, inspired me, and encouraged me in chemistry. I am also grateful for the years working for Prof. Robert Strongin at Portland State University, under the mentorship of Dr. Lovemore Hakuna. In addition, none of my positive undergraduate experiences would have been possible without my insanely supportive, kind, and intelligent friends Natasha Hippler and Dr. Tiffany Morrison, who spent countless late nights with me studying and preparing for chemistry club activities, all while eating way too many Subway sandwiches. I also want to thank everyone at UCSD who made my first few years of graduate school unforgettable. To my incredible group of friends who made me feel so loved and continue to impress me every day- Dr. Eunice Kim, Dr. Allie Chen, Dr. Jeff Mindrebo, Dr. Myles Drance, Dr. Matt Naticchia, Dr. Mitchell Christy, Dr. Dan Honigfort, Dr. Yanice Benitez, Dr. Jon Sauer, and Dr. Ben Dick-

you are the most amazing support system I could ever dream of, and I will always cherish our countless memories.

Lastly, I'd like to thank my amazing family. I appreciate my mother for always encouraging me to pursue higher education, and to never settle. I also thank my sister Kenzie and my brother Carson for their love and support, and my grandparents Tutu, Nana, Howard, Grandpa, and Grammie for always being my cheerleaders. Lastly, an immense thank you to my husband Douglas who has been my partner in life for the past 15 years. He has been my rock and my foundation, and has literally followed me around the country so that I could pursue my education. I could never make it up to him or repay him except to try to show him every day that his love and support means the world to me.

DEDICATION

To my family,

My loving husband Doug,

My friends who have supported me along the way,

and to all the little girls who dreamed of something bigger.

Table of Contents

List of Figures

Chapter 3: Porous Allomelanin Nanoparticles for Toxin and Gas Adsorption

Chapter 4: Novel Artificial Melanosomes of Diverse Morphologies: Eumelanin Analogues

Chapter 5: Skin Applications of Synthetic Melanins

List of Tables

Chapter 1. Introduction to Melanin- Nature's Multifunctional Biopolymer

1.1 Introduction

Melanin is an abundant biopolymer discovered in almost all kingdoms of life.[1] Impressively, it serves an unusually wide range of functions including structural coloration for sexual selection,[2] metal chelation,[3] toxin adsorption,[4, 5] radical quenching, radiation protection,[6] thermoregulation,[7, 8] and increasing material strength.[9, 10] Some of these unique features can be attributed to it possessing one of the highest refractive indices (~1.8-2.0) of any biological material, and its broadband absorption across the ultraviolet (UV), visible, and infrared (IR) spectrum due to an abundance of highly conjugated and aromatic subunits.[1] [11] Melanin is one of the most captivating biomaterials on Earth due to its abundance in almost every kingdom of life, its ability to take on numerous physical forms, and its functional diversity, therefore, it is of great interest to study melanin in depth and to recreate it synthetically. Synthetic melanin-based materials have numerous applications[12] such as in human health,[13, 14] energy,[15] and the environment,[16] and they also aid in understanding the natural world by investigating pure systems, how chemical enhancements improve or alter material function, and by prompting us to search for more exotic systems in nature.[17] It is with this inspiration that we seek to mimic various classes of melanin in the laboratory, and to apply them for protection from toxins and radiation.

The most well-known and familiar example of melanin is as a pigment in human skin, where it exists as a spherical nanoparticle and serves as a natural sunscreen. This abundant class of melanin is called eumelanin, and it serves as the basis for the vast majority of synthetic efforts

toward artificial analogues and their applications, most commonly utilizing polydopamine (PDA) as the synthetic melanin of choice. However, the diversity of melanins in nature extends far beyond eumelanin, and beyond solid spherical structures. Even within a single species, *Homo sapiens* for example, there can exist several classes of melanin, all serving different purposes in different parts of the body. Therefore, there is a need for further study not just of spherical or film-based PDA-based materials, but also of synthetic analogues and applications of other melanin chemistries and morphologies. This chapter will explore the different types of melanin found in nature and describe motivation for synthetic analogues that utilize PDA but also expand the range of chemistries and morphologies available, especially as mimics of fungal melanins. It will also apply these novel melanins to various *in vitro*, *in vivo*, and *ex vivo* studies for application in the protection of human and animal skin from toxins and UV radiation.

1.2 Classification and Synthesis of Melanin

Melanin is an abundant biomaterial found throughout the natural world. It consists of a series of monomeric species which are enzymatically oxidized to form highly crosslinked, high molecular weight polymers with various linkages, and is most commonly found in skin,[18] hair,[19, 20] feathers,[21] and in the cell walls of various organisms.[22] Melanin often exists in nature as nanoscale objects, and has been extensively reproduced and investigated using PDA as a model system.[23] Much is debated about the actual structure of polydopamine;[24] it is thought to be held together by a variety of interactions[25] such as covalent bonds,[24] hydrogen-bonding, cation-π,[26] and π-π interactions. The classification of melanin is also debated, but there are generally considered to be between three and five different classes of melanin.[27, 28] The most simplistic perspective is to consider three major classes of melanin: eumelanin, pheomelanin, and allomelanin.

Eumelanin is the most commonly studied melanin since it is the most biologically relevant to humans, occurring in our skin, hair, eyes,[29] ears,[30] and brain.[31] It is derived from the amino acid tyrosine, which is oxidized by the enzyme tyrosinase to the highly reactive intermediate dopaquinone, which then undergoes a series of reactions where it is ultimately converted to eumelanin. This process can be explained simplistically using the Raper-Mason pathway (Figure 1.1).[32]
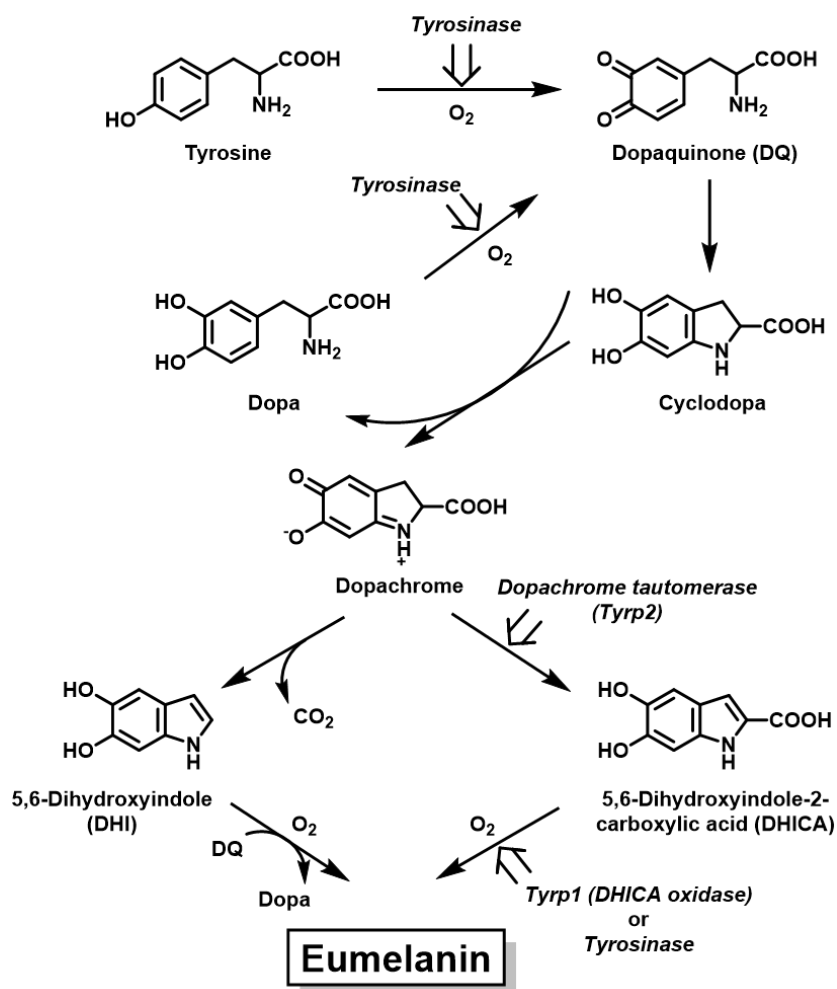
Figure 1.1 Raper-Mason pathway of eumelanin synthesis from tyrosine.[32]

Eumelanin mimics have been synthesized by the oxidation of various intermediates along this pathway, including dopamine (DA), 5,6-dihydroxyindole (DHI), dihydroxyindole carboxylic acid (DHICA), dopa- most commonly levodopa (L-DOPA), and other related monomers. Synthetic eumelanin has been investigated in numerous forms for a variety of uses- as gels,[33] films,[34] particles, coatings, injections, and numerous other examples.

Pheomelanin is synthesized *via* a similar pathway as eumelanin, starting with tyrosine, however its divergence begins with the incorporation of cysteine to form a sulfur-containing melanin rich with benzothiazine subunits. The resulting material imparts a reddish hue, evident in humans with red hair and fair skin, rooster feathers, and orangutan fur. Pheomelanin is also thought to form a seed for eumelanin growth in the brain to form a core-shell type structure.[35]

Allomelanin is very different class of nitrogen-free melanins which are commonly found in fungi, bacteria, and plants. Depending on the categorization, pyomelanin, a homogentisic acid (HGA)-based nitrogen-free melanin, can be aligned under this category, however, allomelanin will be discussed here exclusively in the context of DHN melanin. DHN melanin is named for one of its key precursors, dihydroxynaphthalene (DHN), specifically the 1,8-DHN isomer. This type of melanin originates from acetyl CoA and malonyl CoA pathways and is advantageous for its ability to protect organisms from radiation (Figure 1.2).[36] Fungal DHN melanins can comprise a significant portion of their overall melanin content, but the exact percentage has not yet been quantified. Studies have shown that DHN melanin does not exist in a pure state in the cell wall, rather it is incorporated with other cell wall components such as polysaccharides and chitin.[37, 38] Therefore, synthetic analogues are necessary to isolate the effects of DHN melanin, and to improve its properties. In future, complementary studies, one can also envision engineering organisms to
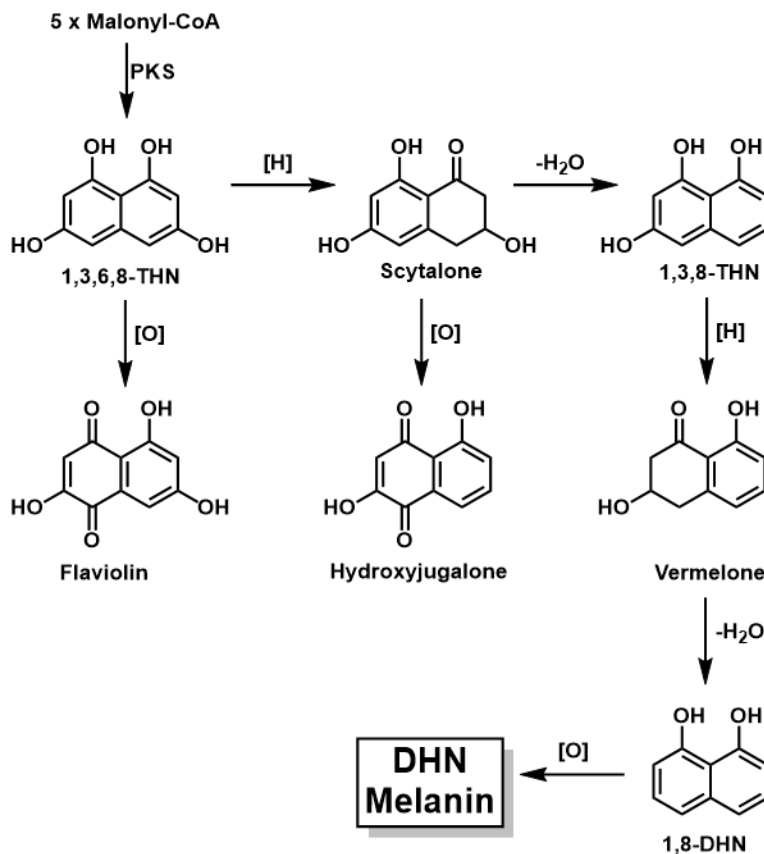
Figure 1.2 Fungal dihydroxynaphthalene (DHN) melanin biosynthesis pathway.[36]

express various amounts of DHN melanin, quantify this distribution, and to test the exact contribution of DHN melanin to its advantageous properties.

1.4 Chemical and Morphological Diversity in Melanin

We've just described that melanin has a diverse array of chemistries, however the diversity found in nature is not reflected in synthetic efforts. There is much less information on the synthesis of more exotic analogues and how they compare to the natural systems.[28] One recent example of an extensively characterized, exotic synthetic melanin highlights a very unusual analogue of pheomelanin, termed "selenomelanin" which substitutes sulfur for the heavier chalcogen selenium. However, these examples of more unusual melanin mimics are few and far between.

In addition to the rich range of melanin chemistries found in nature, there are many morphological differences which result in vastly different nano- and microstructures. However, there is a serious lack of melanin-based synthetic analogues of these unique structures, and there are very few examples of synthetic melanin particles which are not solid spheres or films. Some of the most unusual melanic structures are found in bird feathers as solid or hollow rods or spheres in various arrangements.[1, 39, 40] Several synthetic efforts have attempted to mimic these structures using various templating approaches. Efforts to synthesize rod-like morphologies have frequently used a gold nanorod template. Layer-by-layer assembly was used to make PDA-coated nanorods.[41] Sacrificial gold nanorods templates were etched to form hollow rods, but these were made from polystyrene and silica, not melanin.[42] The formation of hollow spheres has also utilized polystyrene; this time as the sacrificial template. These structures were found to exhibit a range of colors even as amorphous colloidal structures in various liquids.[43] In a similar manner, hollow PDA spheres were made into films which showed superior UV absorption than their solid counterparts.[44] However, to date, there are no examples of hollow melanin rods, template-free melanin spheres, well-defined hollow melanin spheres, or melanin platelets. Additionally, up until just this last month, there was no previous work on synthetic porous melanins, and this recent work was all performed by the Gianneschi lab.[45, 46] The studies presented herein attempt to address these deficiencies by exploring both templated and template-free processes.

1.3 Melanin as a Radiation Protection Agent

Radiation protection is one of the major characteristics of melanin. Human eumelanin is the most salient example of this, and efforts to mimic this process have shown success with

synthetic analogues affording adequate protection against UV radiation. Synthetic PDA nanoparticles provided protective effects both in human skin cells and in mice.[47, 48]

DHN melanin-containing fungal cells have been found in some of the harshest environments known, such as at the Chernobyl nuclear power plant, and on spacecraft. They thrive in environments with high radiation levels, giving their melanization process a special interest.[6, 49, 50] For this reason, fungal cells naturally expressing DHN melanin have been tested in several different contexts relevant to these unique adaptations. An interesting method for performing these studies utilizes *via* fungal ghosts: hollowed out, melanized fungal cell walls which have radiation protection capabilites.[49] DHN-containing mushrooms have also been administered orally to mice and provide radiation protection.[51] However, few synthetic efforts have endeavored to mimic allomelanin, with the most thorough, well-defined, and well-characterized examples illustrated in Chapter 2 and Chapter 3 of this work.

1.4 Melanin as a Toxin Adsorption Agent

Toxins abound in the environment, from natural algal toxins leading to shellfish poisoning,[52] and mycotoxins,[53] to man-made contributions such as pesticides, herbicides, byproducts of industrial processes such as heavy metals[54] and other pollutants, and chemical warfare agents.[55] Several species have evolved to respond to environmental toxins, and one avenue they exploit is the upregulation of melanin production. In butter clams, a correlation was shown between paralytic shellfish poison concentration and melanin concentration, with a site-specific concentration gradient suggestive of melanin acting as a protection mechanism against self-poisoning.[5] Turtle-headed sea snakes were also found to have darker, melanin-based coloration in polluted environments, suggesting their use of melanin as a toxin remediation agent.[4] In addition,

peppered moths rapidly evolved a heavily melanized mutant in a highly polluted environment.[56] Previous studies have also investigated the role of melanin uptake of heavy metals in aqueous solutions[57] and the correlation between higher melanization in mice and higher amounts of metal uptake.[58] However, very few efforts to use melanin as a toxin remediation agent for non-metal-based toxins or small molecules have been published to date,[59] and none utilizing synthetic melanin, until the investigations presented herein.[45, 46]

1.8 Summary

Melanin is a versatile biopolymer that not only serves many purposes in nature, but also has potential applications as a synthetic a material with diverse chemistry. This body of work serves to advance the study of melanin as a material which can be synthesized in the lab using a variety of chemical precursors, and utilized for protection from toxins and radiation. Inspired by the natural melanization process, we synthesized, characterized, and applied several different artificial analogues of melanin. This work highlights the possibilities of artificial melanins as biocompatible, nature-inspired materials for skin protection from radiation and toxins, and paves a pathway for further investigation into melanin for a variety of applications.

Chapter 2. Artificial Allomelanin Nanoparticles as Radiation Protection Agents in Human Skin Cells

This chapter is adapted from the following publication:

2.1 Introduction

Melanins are a group of natural pigments found in numerous organisms such as animals, plants and microorganisms.[60] They are best known for their role in human skin coloring, however they are also involved in various biological activities, such as sequestering metal ions,[61-63] quenching free radicals,[64-66] photoprotection[67-69] and neuroprotection.[70, 71] On the basis of the structure, melanins can be classified into five types: eumelanin,[72] pheomelanin,[73] neuromelanin,[74] pyomelanin[75] and allomelanin.[76, 77] In nature, eumelanin, pheomelanin and neuromelanin share chemical composition similarities originating from their formation from a 3,4-dihydroxyphenylalanine precursor. Most commonly, synthetic mimics of eumelanin have involved preparation of materials by oxidative polymerization of dopamine.[12, 78-81] In the last decade, polydopamine nanoparticles have rapidly expanded to many important applications, such as radiation protection,[82, 83] surface coating,[84] biological imaging[85, 86] and structural color.[87] Allomelanin refers to a group of melanins that consist of nitrogen-free precursors such as catechol and 1,8-dihydroxynaphthalene (1,8-DHN). Typically, allomelanins found in fungi utilize 1,8-DHN as the precursor, thus referred to as DHN-melanin. In fungi, both eumelanin and DHN-melanin

aid in survival in hostile environments[88, 89] by acting as essential components of the cell wall by increasing its rigidity, hydrophobicity, negative charge and reducing porosity.[90, 91] Furthermore, fungal melanins can protect these organisms from high doses of radiation, and in some cases gamma radiation has been shown to be beneficial to melanized fungi[49] with some species found on spacecraft and within the reactor at Chernobyl.[6, 49, 50, 92] Given the myriad functions of natural melanins and the inherent complexity of their chemical nature, synthetic efforts to generate mimics of each type provide promising routes for structure and function analysis of melanins. In many organisms and organ systems (*e.g.* in the human brain *versus* skin), mixtures of melanins with subtle variations in chemistry are found. Hence, in this paper, we describe reliable chemical synthetic routes to allomelanin as a first step, and describe how the resulting artificial allomelanin nanoparticles function as radiation protection agents in human skin cells *via* radical scavenging. Despite the potential of allomelanin in biomedical applications where radiation resistance is desirable, including as radiation protection agents used in tandem with gamma radiation treatments,[93] very little is known about the chemical structure. Some insight is now available given a recent study where synthetic DHN-melanin was prepared *via* a chemoenzymatic route.[94, 95] These initial studies described dimers, trimers, and tetramers through C-C bond formation analyzed by liquid chromatography mass spectrometry (LCMS). For study in biological systems, and to explore radical scavenging ability, we utilized a strategy for formulating uniform allomelanin nanoparticles (AMNPs). Here, we describe synthetic routes *via* oxidative oligomerization of 1,8-DHN using the chemical oxidizing agents $NaIO_4$ or $KMnO_4$ to access 100-300 nm AMNPs. These materials show similar free radical scavenging activity to ascorbic acid, a known antioxidant, with much higher activity than that of size-matched polydopamine-based synthetic melanin

nanoparticles (PDA-NPs). In addition, we demonstrate that AMNPs are non-toxic, and can be internalized by neonatal human epidermal keratinocytes (NHEK) resulting in the formation of microparasols, the protective perinuclear caps found in melanized human keratinocytes.[82] Artificial, synthetic allomelanin-based microparasols protect NHEK cells upon UV irradiation as detected by a quenching effect of reactive oxygen species (ROS) in cell culture.

2.2 Results and Discussion

2.2.1 Synthesis of Artificial Allomelanin Nanoparticles (AMNP)

AMNPs were synthesized *via* oxidative oligomerization of 1,8-DHN in aqueous solution at room temperature. Chemical synthesis was achieved using the oxidizing agents, $NaIO_4$ and $KMnO_4$, (Figure 2.1).[12]
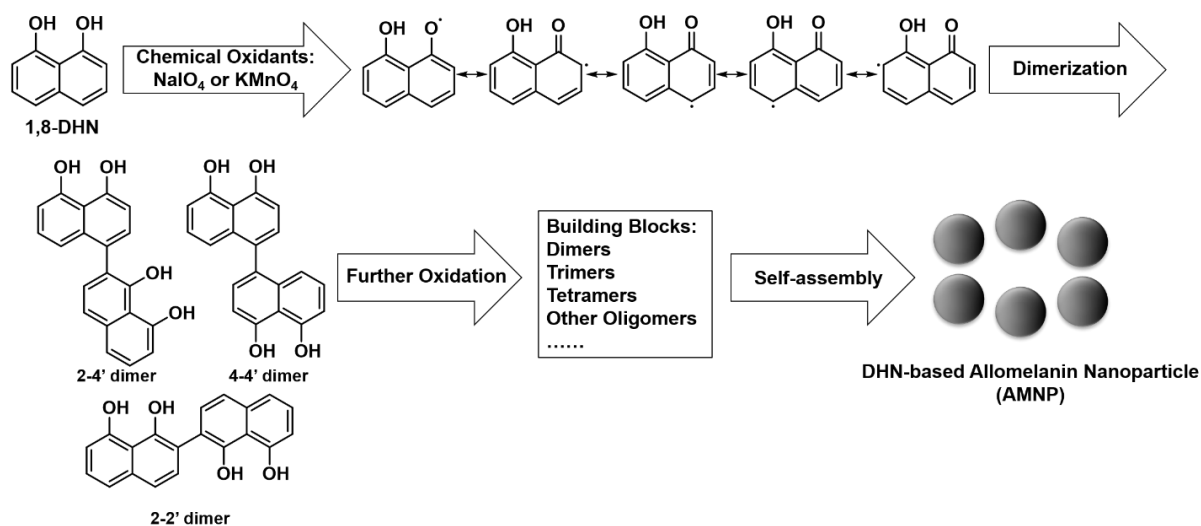
Figure 2.1 Schematic of synthesis of AMNPs. Oxidative oligomerization of 1,8-DHN was achieved using oxidizing agents $NaIO_4$ or $KMnO_4$. Resulting oligomers and polymers self-assemble to form AMNPs.

Briefly, 1,8-DHN (1.0 mg/mL) was dissolved in a mixture of acetonitrile and ultrapure water, followed by rapid injection of a 1 N $NaIO_4$ solution into the reaction mixture. When using $KMnO_4$ as the oxidizing agent, ultrapure water was exchanged for acetate buffer (0.1 M, pH = 3.7) to ensure the oxidative capability of $KMnO_4$. Immediately upon injection of the oxidizing agents, the colorless solution rapidly turned yellow, then gradually to dark gray. After 12 h, the resulting nanoparticles were purified through five centrifugation/redispersion processes in ultrapure water. Chemoenzymatic AMNPs were synthesized by laccase-mediated oxidation of 1,8-DHN.[94] AMNPs synthesized using $NaIO_4$, $KMnO_4$, and laccase were named AMNP-1, AMNP-2, and AMNP-3, respectively.
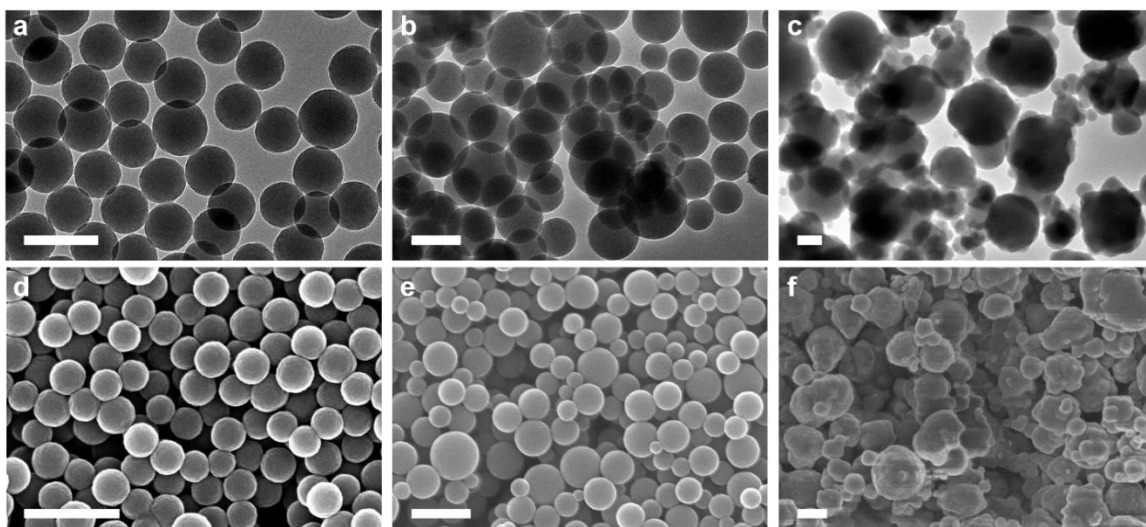
Figure 2.2 Morphology and size characterization of AMNPs by (a, b, c) TEM, scale bars 200 nm, and (d, e, f) SEM, scale bars 400 nm. Electron micrographs of (a, d) AMNP-1, (b, e) AMNP-2, and (c, f) AMNP-3.

AMNPs were characterized by transmission electron microscopy (TEM) and scanning electron microscopy (SEM) (Figure 2.2). AMNP-1, synthesized using $NaIO_4$, resulted in monodisperse spheres with an average diameter of 140±10 nm calculated from TEM micrographs.

The hydrodynamic diameter of AMNPs was measured using dynamic light scattering (DLS) (Figure 2.3), showing a diameter of 194 nm with a polydispersity index of 0.08 for AMNP-1. AMNP-2, synthesized using $KMnO_4$, resulted in higher dispersity spherical nanostructures with diameters between 100 nm and 300 nm by TEM and 227 nm with a polydispersity index of 0.09 by DLS.
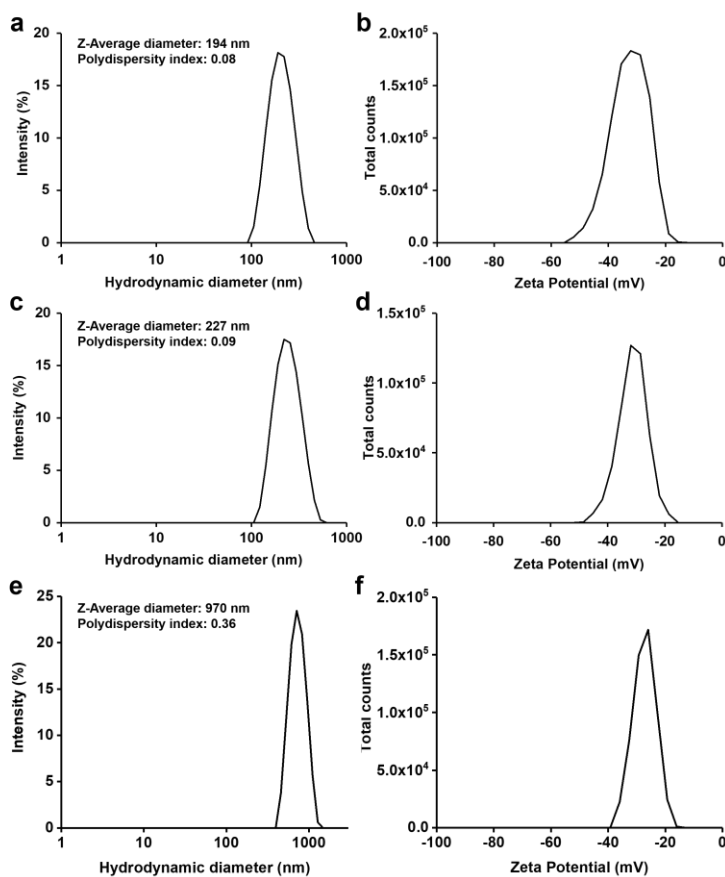
Figure 2.3 Average size of AMNPs was determined *via* dynamic light scattering in ultrapure water to be (a) 194 nm with a polydispersity index of 0.08 for AMNP-1; (c) 227 nm with a polydispersity index of 0.09 for AMNP-2; (e) 970 nm with a polydispersity index of 0.36 for AMNP-3. Zeta potential of (b) AMNP-1; (d) AMNP-2; (f) AMNP-3.

TEM micrographs reveal the poorly defined morphology of chemoenzymatically prepared AMNP-3 with DLS showing a similar range in sizes with a peak at 970 nm with a polydispersity index of

0.36. The zeta potentials for synthetic AMNPs show peaks at -31 mV, -33 mV and -27 mV for AMNP-1, AMNP-2, and AMNP-3, respectively, indicating high colloidal stability (Figure 2.3).
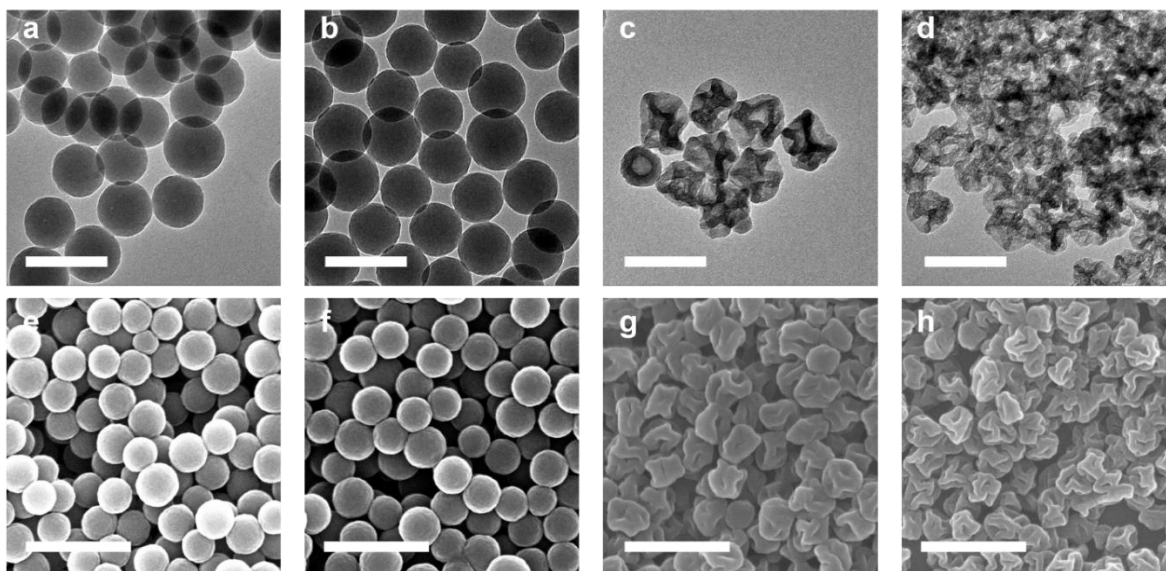
Figure 2.4 TEM micrographs of AMNP-1 with different molar ratios of $NaIO_4$ to 1,8-DHN monomer of (a) 0.2:1.0 (b) 0.5:1.0 (c) 1.0:1.0 (d) 1.5:1.0. Scale bars 200 nm. SEM micrographs of the corresponding AMNP-1 with molar ratios of $NaIO_4$ to 1,8-DHN of (e) 0.2:1.0 (f) 0.5:1.0 (g) 1.0:1.0 (h) 1.5:1.0. Scale bars 400 nm.

In addition, by changing the molar ratio of $NaIO_4$ to 1,8-DHN monomer, AMNP-1 morphology was altered (Figure 2.4). By screening various reaction conditions, it was discovered that adding a higher ratio of oxidizing agent, above 1.0:1.0, resulted in particles which resemble the shape of a walnut, having lower sphericity than those obtained with ratios below 1.0:1.0. TEM and SEM micrographs show spherical or "walnut-like" structures when $NaIO_4$ to 1,8-DHN molar ratios were changed from 0.2 to 1.5.

2.2.2 Characterization of AMNP

Fourier transform infrared spectroscopy (FTIR) was performed to investigate the chemical structure of AMNPs (Figure 2.5). All three AMNPs share the same characteristic peaks observed
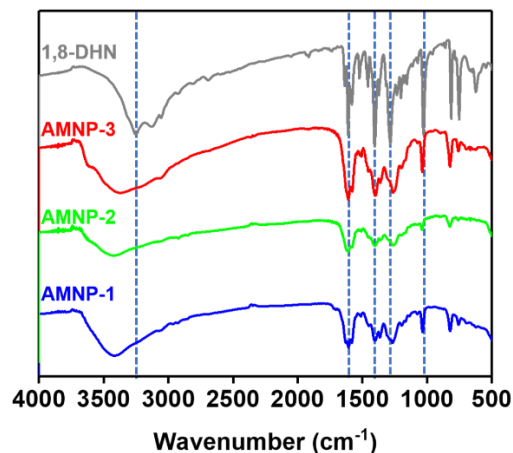
Figure 2.5 FTIR spectra of AMNP-1, AMNP-2, AMNP-3, and 1,8-DHN monomer.

for the 1,8-DHN monomer. The sharp peaks at 3120 cm^{-1}, 1611 cm^{-1}, 1402 cm^{-1}, 1284 cm^{-1}, and 1038 cm^{-1} correspond to aromatic C-H stretching, aromatic C=C stretching, C-OH bending, C-OH stretching, and aromatic C-H bending, respectively. The broad peaks in the 3200-3400 cm^{-1} range are attributed to the stretching of -OH groups on the naphthalene ring. After formation of AMNPs, the aromatic C-H bending peak at 753 cm^{-1} is strongly suppressed due to intermolecular crosslinking of the naphthalene rings. AMNP-1 and AMNP-2 show a broad absorption in the UV, peaking at ~ 350 nm, while AMNP-3 shows a broader, red-shifted absorption, with a maximum at approximately 430 nm (Figure 2.6).
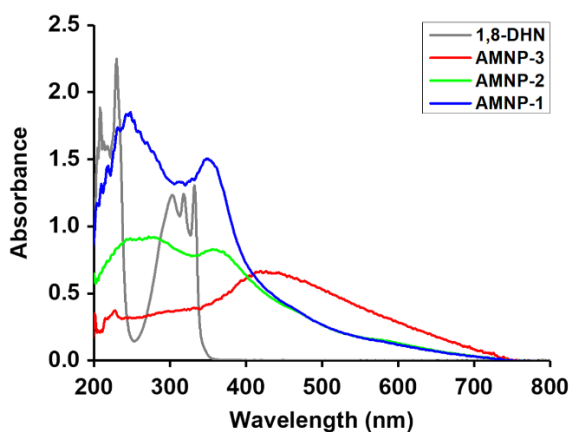
Figure 2.6 UV-Vis spectra of AMNPs and 1,8-DHN monomer.

Compared to the absorption of the 1,8-DHN monomer, all three types of AMNPs show a bathochromic shift which may indicate an expansion of the conjugated system due to the oxidative coupling as well as strong π–π-stacking interactions between the molecules.[96]

High-performance liquid chromatography (HPLC) was used to determine the chemical makeup of AMNP-1 and AMNP-2. It was discovered that upon treatment of the freshly synthesized particles with acetonitrile (ACN), they dissolved and could be subjected to further analysis.
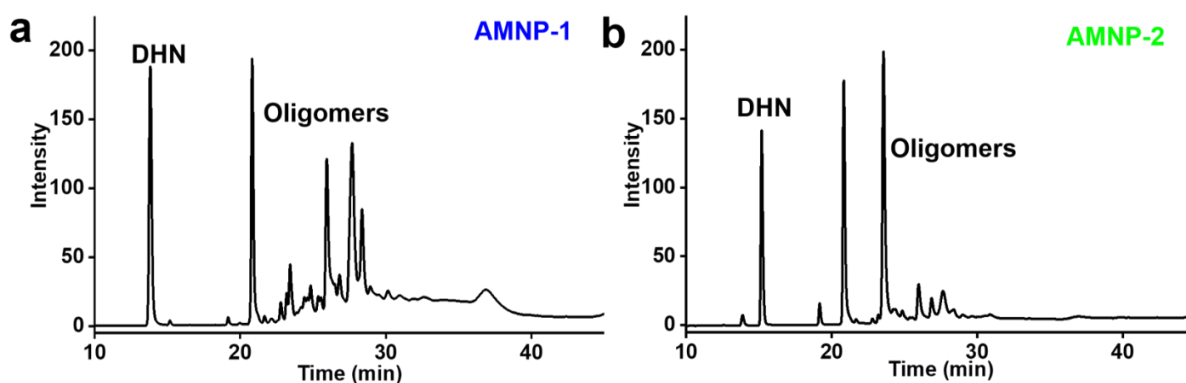
Figure 2.7 HPLC spectrum of (a) AMNP-1 with 0.5 molar ratio of $NaIO_4$ to DHN (retention time at 14.0 min corresponds to DHN monomer); (b) AMNP-2 with 0.2 molar ratio of $KMnO_4$ to DHN (retention time at 15.0 min corresponds to DHN monomer). AMNP-3 could not be dispersed in any of the organic solvents tested.

The small molecules and oligomers therein were analyzed by HPLC using an ACN/water gradient, and the results indicated that the particles consisted of a mixture of monomer, dimers, and low order oligomers (Figure 2.7). Interestingly, the distribution of chemical species was different for AMNP-1 and AMNP-2, which could be indicative of different reaction kinetics due to differences in reactivity between $KMnO_4$ and $NaIO_4$, although we note that these oxidants have very similar reduction potentials. AMNP-3 could not be dissolved using ACN or other organic solvents,

indicating a higher degree of polymerization, consistent with the broad, red-shifted absorption spectrum shown in Figure 2.6.
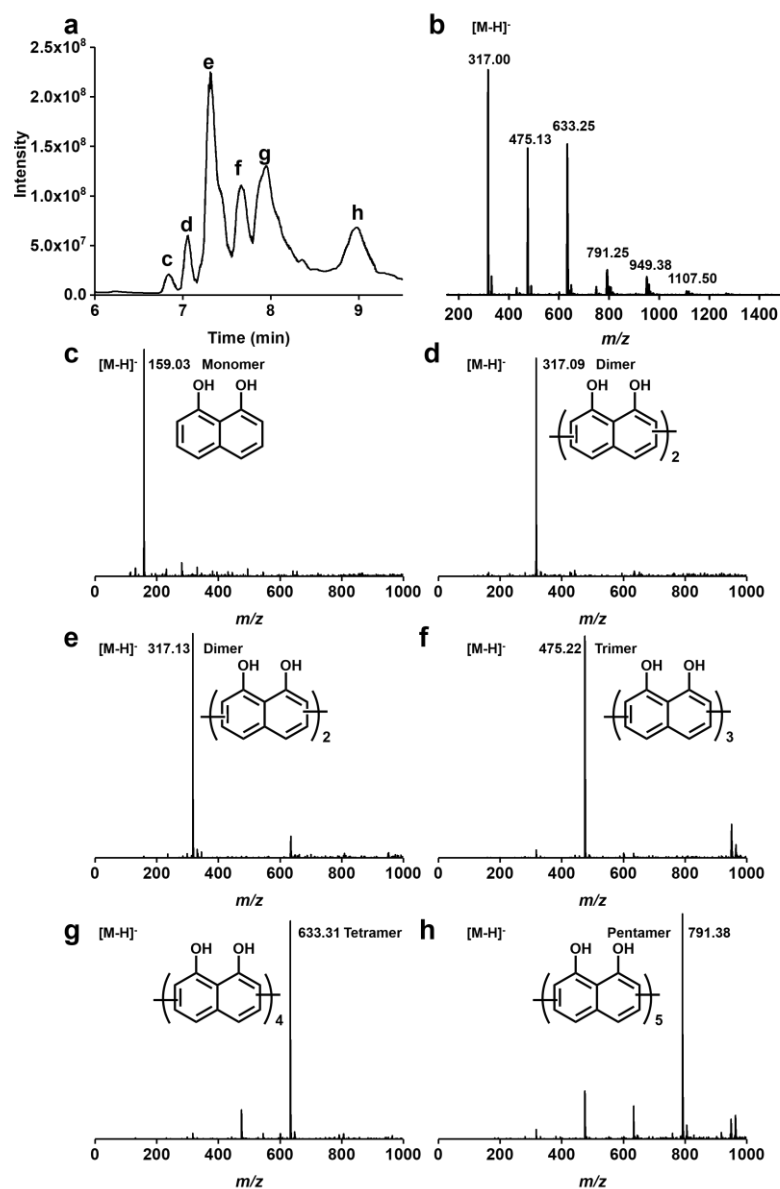
Figure 2.8 (a) LC spectrum of AMNP-1 with a 0.5:1.0 molar ratio of NaIO$_4$ to DHN; ESI-MS spectra of (b) AMNP-1 in negative mode; (c) monomer, t = 6.83 min; (d) dimer, t = 7.05 min; (e) dimer, t = 7.31 min; (f) trimer, t = 7.66 min; (g) tetramer, t = 7.96 min; and (h) pentamer, t = 8.98 min.

For further elucidation of the chemical species, electrospray ionization mass spectrometry (ESI-MS) and LCMS were performed and revealed that that monomer and oligomers could be separated and assigned, with the most abundant oligomer being a dimer at *m/z* 317, with pentamers detectable (Figure 2.8). In a complementary mass spectrometry study, matrix-assisted laser desorption ionization-time-of-flight (MALDI-TOF) mass spectra of AMNPs were obtained (Figure 2.9). These display a distribution of oligomers that are separated by 158 Da, corresponding to the "in-chain" DHN unit.
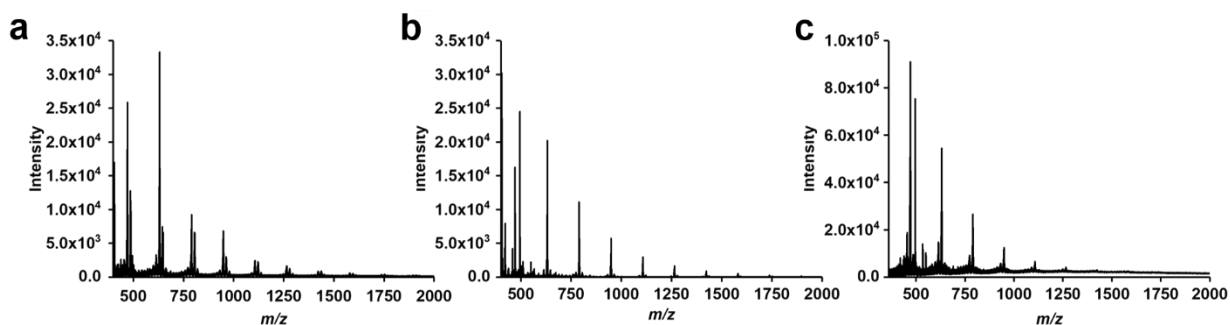
Figure 2.9 MALDI-TOF spectra of (a) AMNP-1; (b) AMNP-2; and (c) AMNP-3 in reflectron, negative mode.

Oligomers with repeating units up to 12 can be observed for AMNP-1 and AMNP-2. For AMNP-3, either low molecular weight oligomers or the fragments of high molecular weight oligomers could be observed.

The above analyses suggest that oligomerization of AMNPs involves intermolecular C-C coupling, further oxidation to form oligomers, and non-covalent self-assembly to form nanoparticles.[94] Therefore, the 1,8-DHN monomer was first oxidized to form a 1,8-DHN radical. This radical has several resonance structures leading to coupling through C-C bonds to form appropriate dimers. Considering the resonance structures, the coupling reaction happens mainly

between C2, C7, C4, and C5 to form three types of dimers: 2-2', 4-4', and 2-4' dimers. Further oxidation and oligomerization of these dimers results in oligomers of the 1,8-DHN monomer which self-assemble to form spherical nanoparticles through the hydrogen bonding of -OH groups and π-π stacking of naphthalene rings (Figure 2.1).

Melanin pigments extracted from several species of fungi have shown the ability to perform as natural antioxidants which can scavenge free-radicals (reactive nitrogen and oxygen species).[97] AMNPs were initially characterized by EPR to confirm the existence of free-radicals. Next, the antioxidant properties of AMNPs were investigated using the 2,2-diphenyl-1-(2,4,6-trinitrophenyl) hydrazyl (DPPH) assay (Figure 2.10).[97]
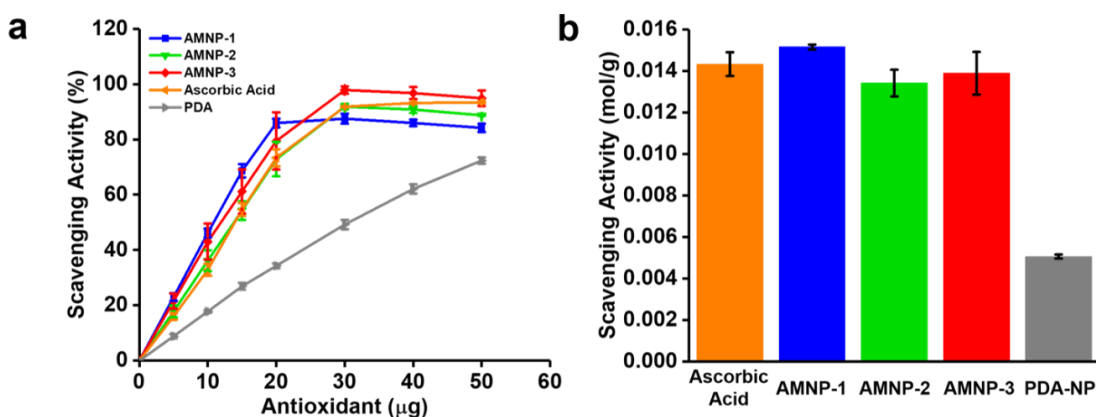
Figure 2.10 Radical scavenging by AMNPs compared to PDA-NPs and ascorbic acid. (a) DPPH radical scavenging activity of antioxidants. (b) Calculated amount of quenched DPPH per gram of antioxidant.

The scavenging activity was determined by monitoring the decrease in absorbance at 516 nm, indicative of the free radical DPPH. DPPH is reduced through an electron transfer from the antioxidant material, and the radical scavenging activity can be evaluated using UV-Vis spectroscopy. All materials were freshly prepared prior to performing the DPPH assay, and the PDA-NPs were size-matched to those of AMNP-1. Free-radical scavenging activity of PDA-NPs

and ascorbic acid, a known antioxidant, were included for comparison to that of the AMNPs (Figure 2.10a). Scavenging activity for all three types of AMNPs was significantly higher than for PDA-NPs per gram of material (Figure 2.10b). Based on these results, AMNPs show a much higher antioxidant activity than that of PDA-NPs, with similar activity to ascorbic acid. The radical scavenging activity of walnut-like AMNP-1 was also tested, observing a trend of decreasing radical scavenging activity, which could be attributed to a higher degree of oligomerization from over-oxidation of the particles.

2.2.3 *In vitro* Assessment of AMNP Uptake and Radiation Protection in Human Skin Cells

Cell studies were performed to understand and probe the cellular compatibility and protective nature of AMNPs. PDA-NPs have been shown to serve as melanin mimics that are internalized by primary adult human keratinocytes to form perinuclear structures which serve as protective agents for the cells.[82] Here, we utilized primary neonatal human epidermal keratinocyte (NHEK) cells to test whether AMNPs, which are chemically different from natural eumelanin and PDA, could be internalized by human cells in the same manner as eumelanin and eumelanin mimics. Our ability to acquire a steady source of fresh tissue to isolate primary cells enabled us to obtain cells from different donors, increasing our sample size, thereby allowing for more rigor in our experiments. Furthermore, the NHEK cells were readily amenable to differentiation, which allowed for assessment of the penetration of AMNPs into more complex and developed cell cultures. In initial uptake studies, undifferentiated NHEK cells were grown in monolayer and incubated with AMNPs, PDA-NPs, or silica nanoparticles. PDA-NPs were used for comparison to previous studies showing the biocompatibility and radiation protected effects of PDA,[82] and the silica nanoparticles served as non-toxic, non-melanin-based control particles of similar size and
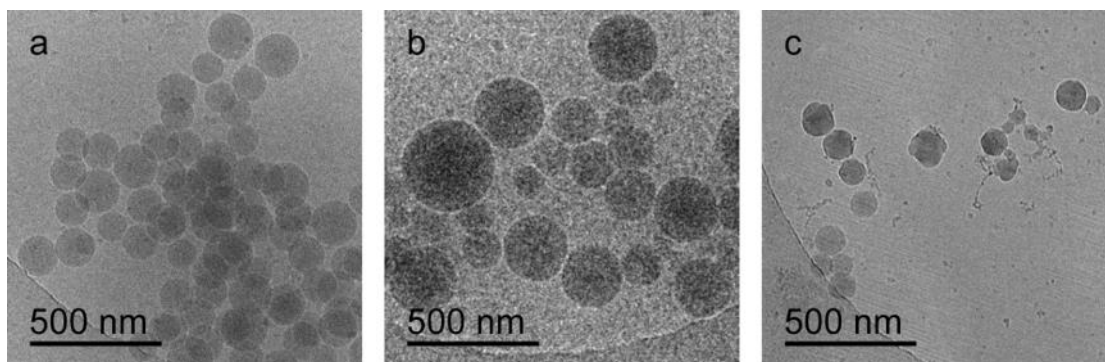
Figure 2.11 Cryo-TEM of AMNPs in cell media, (a) AMNP-1; (b) AMNP-2; and (c) AMNP-3. Particles were incubated in cell culture media at 0.04 mg/mL for 48 hours, then 4 µL of suspended AMNP particles was vitrified and imaged.

negative zeta potential to AMNPs. We also performed cryogenic TEM (cryo-TEM) on AMNPs to ascertain the stability of the particles in cell media (Figure 2.11). The particles remained as discrete objects after incubation with cell media at 0.04 mg/mL for 48 hours, showing good colloidal stability even in complex milieu. After treatment of NHEK cells with 0.04 mg/mL of silica, AMNP, or PDA nanoparticles for 24 hours, we observed no appreciable cytotoxicity as compared to the vehicle-treated control using the MTT cell viability assay (Figure 2.12). The MTT assay is a colorimetric assay which determines the ability of cells to reduce an MTT dye from its tetrazole (yellow) form to a formazan (purple) form through the action of mitochondrial reductase. The absorbance of the formazan product is quantified by a plate reader, and assesses the overall metabolic activity of the cell. The concentration of melanin used for this experiment was chosen as the near maximum amount that the cells can internalize before becoming coated on their surfaces, which results in imaging becoming quite difficult due to the presence of large regions of black material. In addition, concentrations above 0.04 mg/mL leave excess material in the culture medium, prohibiting accurate correlation between the concentration of material in the cells, and cytotoxic (or other) effects.
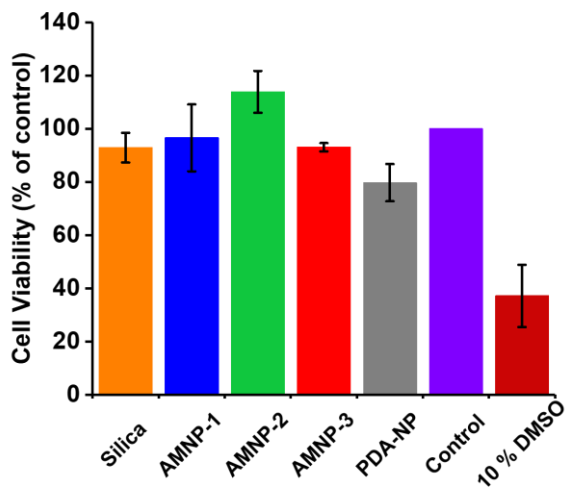
Figure 2.12 Cell viability of NHEK cells incubated for 24 hours with 0.04 mg/mL of AMNPs, PDA-NPs, silica nanoparticles, or the vehicle (water) as a control, and assessed using the MTT assay. All values are relative to the control, normalized to 100%.

Cellular uptake of AMNPs resulted in trafficking of particles to the perinuclear region to form cap-like structures (also called microparasols), which are visibly similar to those formed after incubation with PDA-NPs (Figure 2.13). This result is unexpected given the differences in chemistry between dopamine and 1,8-DHN precursors, and the lack of nitrogen in AMNPs. It was previously not known whether a synthetic fungal melanin analogue would be biocompatible with human skin cells, but these results suggest that the surface chemistry is perhaps sufficient to be recognized as melanin. Both PDA and DHN-based melanin analogues contain aromatic hydroxyl groups in various redox and protonation states, with correspondingly similar negative zeta potentials. The perinuclear structures are most apparent in transmitted light images where the caps appear black. They form condensed structures around the nuclei in bright-field and fluorescence merged images. At higher concentrations, caps begin to form 360° around the nucleus, however, at concentrations below 0.04 mg/mL they are commonly asymmetric and localized to one side of the nucleus, as in naturally melanized human keratinocytes.[98, 99]
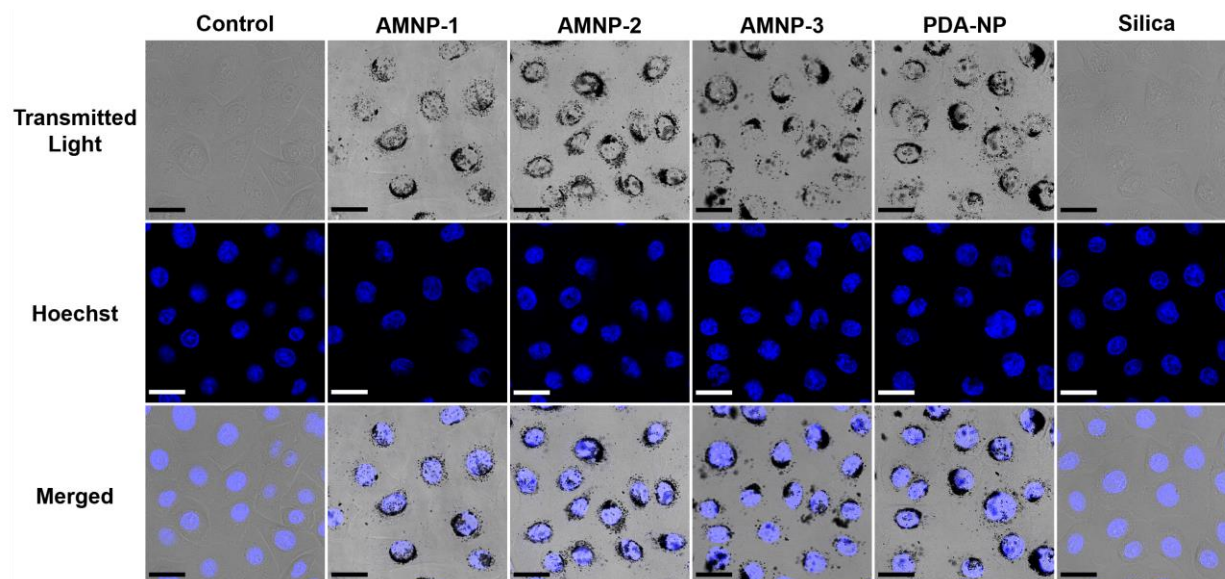
Figure 2.13 Confocal microscopy of NHEK cells incubated with 0.04 mg/mL of particles for 48 hours. Microparasol formation is apparent as black crescents in the perinuclear region of each cell in the transmitted light images. Nuclei are labeled with Hoechst (blue). Scale bars 25 μm.

To visualize the structures formed around the nuclei at high magnification and resolution, cells were grown in a monolayer, treated with nanoparticles, embedded in resin, and sectioned for scanning TEM (STEM) imaging (Figure 2.14). Images were acquired using a high-angle annular dark field (HAADF) detector and the contrast inverted to maintain the appearance of conventional bright-field TEM. All AMNPs formed perinuclear caps, visible at lower magnification (Figure 2.14a), and more detailed at higher magnification (Figure 2.14b), in a similar fashion to PDA-NPs. These results were consistent with the structures visible in the confocal microscopy images. After treatment with silica nanoparticles, we observed a distribution of particles packaged in vesicles throughout the cell, distinct from the localized, asymmetric caps formed from the synthetic melanin particles, indicating that keratinocytes have the ability to discern whether or not the nanomaterials they are internalizing are sufficiently "melanin-like."
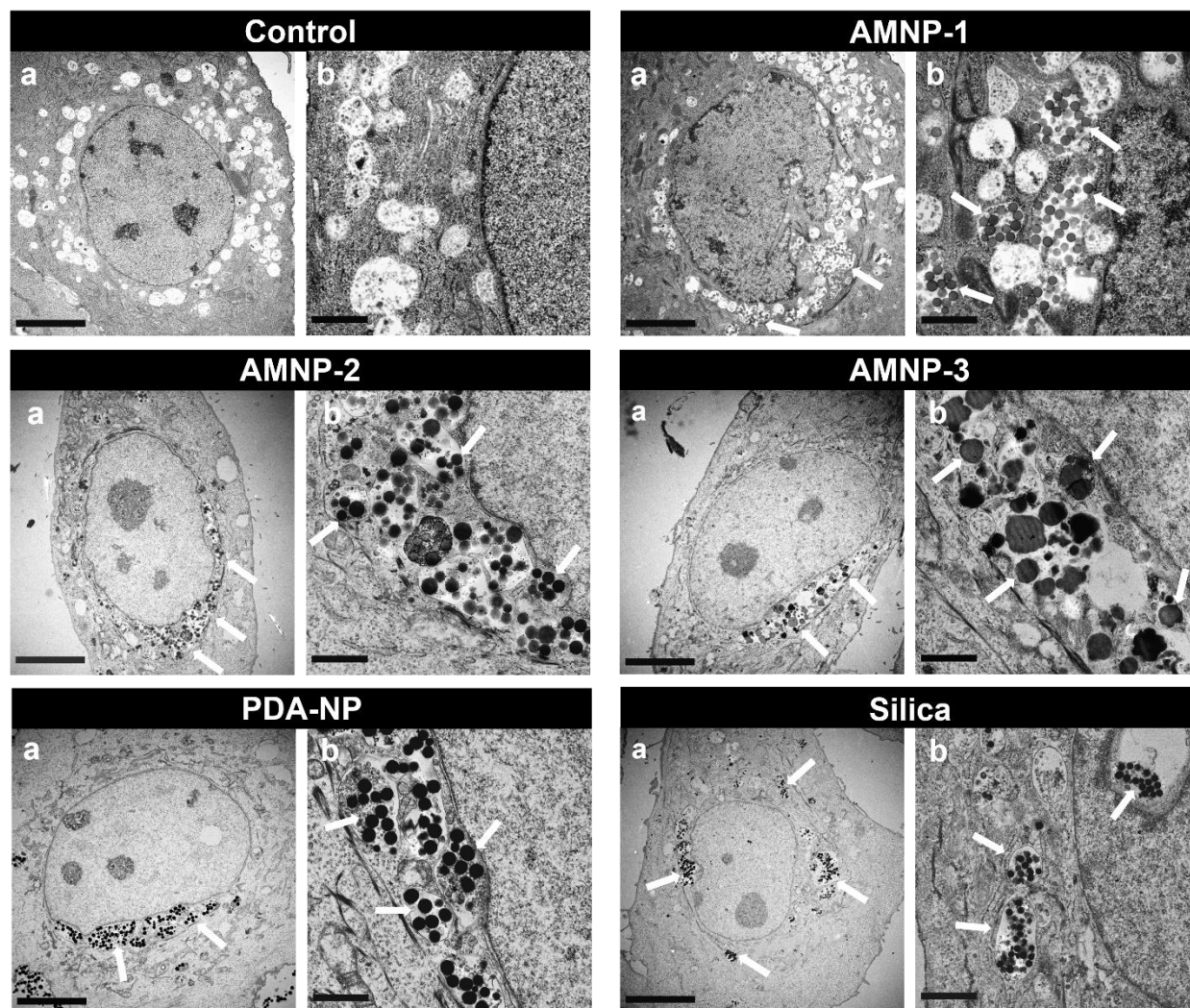
Figure 2.14 STEM micrographs of monolayer NHEK cells treated with the vehicle or 0.04 mg/mL AMNPs, PDA-NPs, or silica nanoparticles for 48 hours, resin-embedded, and sectioned to 60 nm thick. Images were acquired using an HAADF detector and contrast inverted to simulate traditional bright-field TEM images. Scale bars 5 μm (a, lower magnification) and 1 μm (b, higher magnification). Arrows point to nanoparticles inside the cells.

NHEK cells in confluent monolayers were also exposed to high calcium media (1.2 mM) for 24 hours to partially induce epidermal differentiation (Figure 2.15). Calcium is one of the most well studied and most important triggers for epidermal differentiation.[100] A sudden, sustained increase in calcium concentration (>1.0 mM) causes a host of biological changes which trigger the cells to produce different types of keratins and to form close cell-cell contacts which are involved
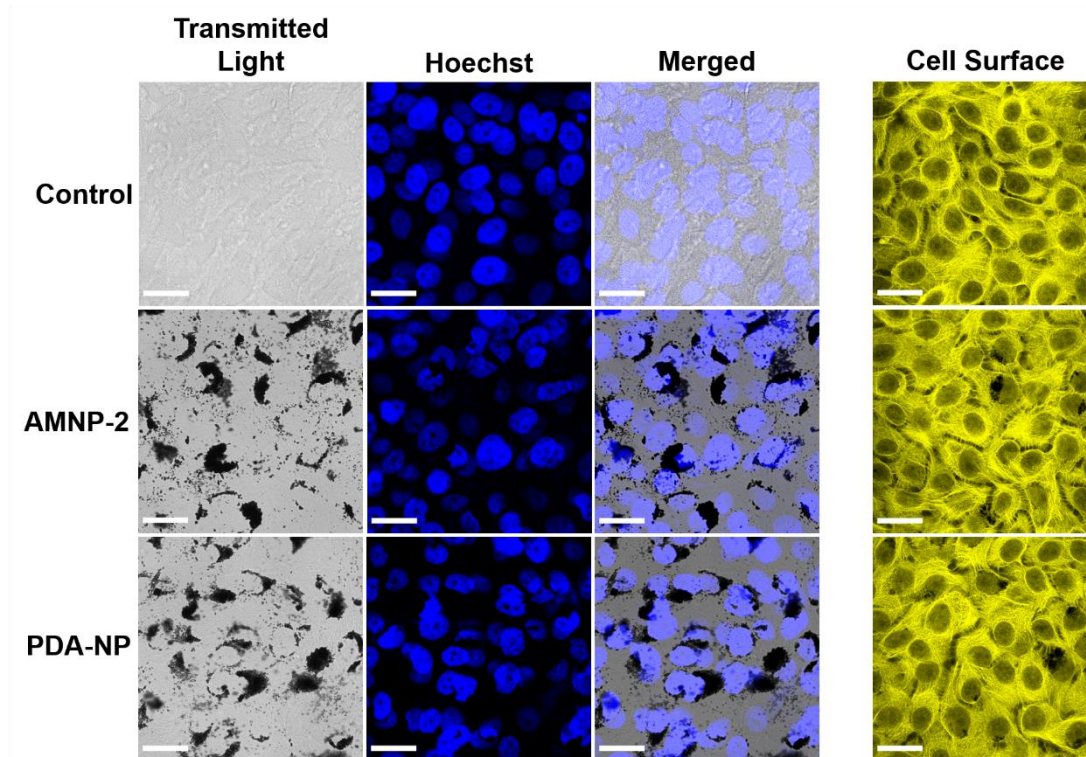
Figure 2.15 NHEK cells were differentiated in 1.2 mM $CaCl_2$ for 24 hours and then incubated with the vehicle, or 0.04 mg/mL AMNP-2 or PDA-NP. Perinuclear caps are apparent as black crescents in the transmitted light images. Nuclei are stained with Hoechst (blue). Images show a single section through the center of the cell layer (left three columns). The cells were also stained with CellTracker™ Orange CMRA dye (yellow, rightmost column). Scale bars 25 µm.

in adhesion and signaling. We wanted to probe whether AMNPs could penetrate more complex cell cultures than sub-confluent monolayers of undifferentiated cells, which are readily accessible to incoming materials. After a confluent monolayer of NHEK cells were calcium switched to 1.2 mM for 24 hours, they were then incubated with the vehicle, or 0.04 mg/mL AMNP-2 or PDA-NP. When viewing the surface of the cell culture, tight packing and cell-cell contacts were visible, with little melanin material detectable (Figure 2.15, rightmost column). However, by imaging a section through the center of the cells using confocal microscopy, perinuclear caps were apparent as black crescents in the transmitted light images (Figure 2.15, first and third columns).

This result illustrates that these synthetic melanins can penetrate more complex cell architectures and provides some insight for future studies where penetration of the skin is desired. It is important to note though that these partially differentiated cultures do not possess the complex layering of the fully formed epidermis, and any extrapolation of this system to intact skin is not advised. Nevertheless, these results provide additional information that suggests that these materials are favorably internalized by keratinocytes in more than one type of environment and may be useful for applications using more complex models than those typically shown in the literature. Given the promising uptake studies, we endeavored to test whether these melanized cells were conferred additional protection from UV radiation.
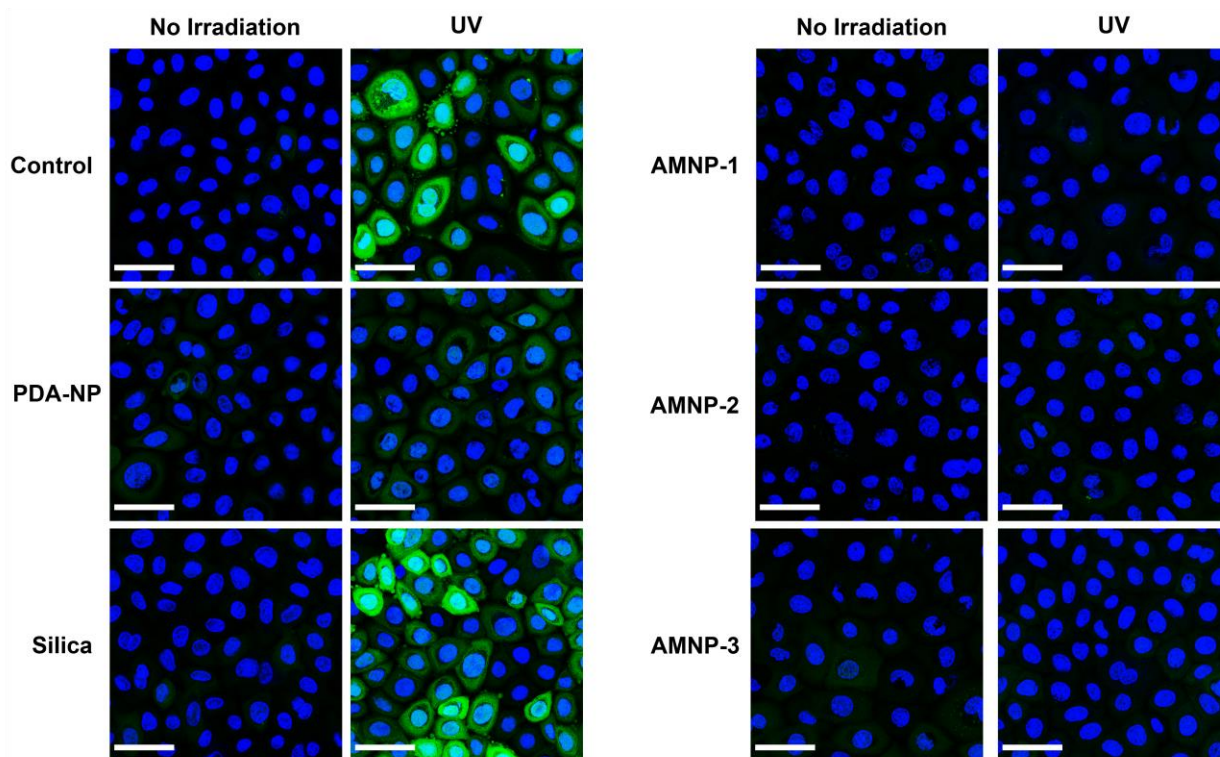
Figure 2.16 Oxidative stress was assessed *via* the ROS-activated CM-H$_2$DCFDA dye (green). NHEK cells were incubated for 3 days with 0.02 mg/mL of AMNP-1, -2 and -3, PDA-NPs, silica nanoparticles, or the vehicle (water), treated with the dye, subjected to 365 nm UV irradiation, and imaged live. Nuclei were stained with Hoechst (blue). Scale bars 25 µm.

To assess cellular protection ability, cells were treated for 3 days with either the vehicle or 0.02 mg/mL AMNPs, PDA-NPs or silica nanoparticles. They were subsequently incubated with 5/6-chloromethyl-2',7'-dichlorodihydrofluorescein diacetate (CM-H$_2$DCFDA), a pro-fluorescent dye that is ROS-responsive, and then directly exposed to 365 nm UV light with an irradiance of 2.25 mW/cm^2 for 2 minutes (Figure 2.16). The control (vehicle-treated) and silica-treated cells showed a higher signal in the CM-H$_2$DCFDA channel than the AMNP- or PDA-NP-treated cells, indicating that AMNPs serve as effective antioxidants inside the cells. These encouraging results illustrate that AMNPs could have potential to serve as radiation agents that could be one day used as a type of bio-inspired, non-toxic sunscreen or antioxidant for the mitigation of ROS generated by other types of skin damage.

2.3 Conclusion

In summary, we have developed methods for synthesizing artificial AMNPs from the precursor 1,8-DHN by oxidative oligomerization. We demonstrated the ability to access different morphologies of AMNPs by tuning the type and amount of oxidizing agent. For example, we obtained uniform spherical and "walnut-like" AMNPs using NaIO$_4$. AMNPs were characterized by UV-Vis, FTIR, mass spectrometry, solid-state NMR, and EPR, showing similar chemical makeup for each type of oxidant used. We observed by LCMS that the formation of AMNPs involves covalent coupling to form oligomers, followed by non-covalent self-assembly of oligomers to form AMNPs, observable by SEM, TEM and DLS. Furthermore, AMNPs were found to exhibit reversible redox activity and good radical scavenging abilities compared to PDA-NPs. In addition, these nitrogen-free melanins, not naturally found in humans, are not only biocompatible but are recognized, internalized, and packaged by NHEK cells as protective

perinuclear cap-like structures. Cells treated with AMNPs and subsequently exposed to UV irradiation show a decreased signal from an ROS-activated fluorophore, indicating that AMNPs are effective radical quenchers not only by themselves, but also *in vitro* in human cells. With a synthetic route in hand, and initially promising data showing radical scavenging and radiation protection, we propose AMNPs as of potential utility in sunscreens and in protective coatings.

2.4 Experimental Details

Reagents. 1,8-Dihydroxynaphthalene (1,8-DHN) (95+%) was purchased from Matrix Scientific. Dopamine hydrochloride (99%) was purchased from Alfa Aesar. Tetraethyl orthosilicate (TEOS) (98%) and sodium phosphate monobasic dihydrate (98%) were purchased from Acros Organics. Laccase from *Trametes versicolor* ($\geq$0.5 U/mg), 2,2-Diphenyl-1-(2,4,6-trinitrophenyl) hydrazyl (DPPH), ammonium hydroxide solution (28-30%), sodium phosphate dibasic ($\geq$99.0%), chitosan (molecular weight, 50,000-190,000 Da), 1,1'-ferrocenedimethanol (Fc) (97%) and hexaammineruthenium(II) chloride ($Ru(NH_3)_6Cl_3$) (99.9%) were purchased from Sigma-Aldrich. Sodium hydroxide (NaOH) (extra pure), potassium permanganate ($KMnO_4$) (99%), sodium periodate ($NaIO_4$) (99.8%), HPLC-grade acetonitrile (CH_3CN) ($\geq$99.99%), acetic acid (HOAc) ($\geq$99.7%), sodium acetate trihydrate ($NaOAc\cdot3H_2O$) (99%), sodium dithionite (laboratory grade), and all other chemical reagents were purchased from ThermoFisher Scientific unless otherwise noted. Ethanol (200 proof) was purchased from Flinn Scientific. All chemicals were used as received. Ultrapure water was purified using a Branstead GenPure xCAD Plus system from ThermoFisher Scientific and used in all experiments. All grids for transmission electron microscopy (TEM) and scanning electron microscopy (SEM) were purchased from Electron Microscopy Sciences (EMS) unless otherwise noted. Cryogenic TEM (cryo-TEM) was performed

on QUANTIFOIL® Q250-CR2 holey carbon copper grids. Cell sections were imaged on 1-2 mm slotted copper formvar/carbon grids. Lacey carbon, 300 mesh, copper grids were purchased from Ted Pella. Grids were surface plasma treated using a PELCO easiGlow glow discharge cleaning system. Cell viability was performed using the thiazolyl blue tetrazolium bromide (MTT) reagent (98%) from Sigma Aldrich. Neonatal human epidermal keratinocyte (NHEK) cells were donated by the Bethany Perez-White Lab at Northwestern University Feinberg School of Medicine. All other cell culture reagents were acquired from ThermoFisher Scientific.

Instrumentation. SEM images were acquired on a Hitachi S4800-II cFEG SEM and a Hitachi SU8030. Dry state TEM of nanoparticles was conducted on a Hitachi HT-7700 biological TEM at an acceleration voltage of 120 kV. Cryo-TEM experiments were performed on a JEOL ARM300F (300 kV) with a cryo holder and transfer station (Gatan Inc., USA) operating at ~ – 170 °C. UV-Vis spectra were recorded using a NanoDrop 2000c UV-Vis spectrophotometer. Fourier transform infrared spectrometry (FTIR) spectra were obtained on a Nexus 870 spectrometer (Thermo Nicolet). Electrospray ionization mass spectrometry (ESI-MS) spectra were acquired on a Bruker AmaZon SL. Liquid chromatography–mass spectrometry (LCMS) experiments were conducted on a Bruker AmaZon X. Analytical high-performance liquid chromatography (HPLC) analysis was performed on a Jupiter 4u Proteo 90A Phenomenex column (150 x 4.60 mm) using a Hitachi-Elite LaChrom L-2130 pump equipped with UV-Vis detector (Hitachi-Elite LaChrom L-2420). Matrix-assisted laser desorption ionization-time-of-flight mass spectrometry (MALDI-TOF MS) spectra were obtained on a Bruker AutoFlex-III. Hydrodynamic diameters and zeta potentials were measured on a Zetasizer. Cell viability assays were read on a Biotek Synergy Neo2 plate reader. Confocal images were obtained on a Leica SP5 laser scanning

confocal microscope. Resin-embedded cells were microtomed using a Leica EM UC7/FC7 cryo-ultramicrotome and imaged on a Hitachi HD2300 STEM microscope with a high-angle annular dark field (HAADF) detector at an acceleration voltage of 80kV. Cell irradiation was performed with a UVP 8W, 365 nm UVLS-28 EL Series lamp.

MALDI-TOF Sample Preparation. MALDI-TOF measurements were performed on a Bruker AutoFlex-III time of flight instrument, operating in negative reflectron mode. AMNPs were suspended in ultrapure water to reach a final concentration of 0.01 mM. This solution was mixed with a saturated solution of the matrix (2,5-dihydroxybenzoinc acid, DHB) in water (50:50 volume ratio). This suspension was deposited on the stainless-steel sample holder and air-dried. Mass spectra were obtained by averaging the ions from 5,000 laser shots.

2.4.1 Synthesis of Artificial DHN-based Allomelanin Nanoparticles

AMNP were prepared by oxidative oligomerization of 1,8-DHN in a solution containing sodium periodate ($NaIO_4$) or potassium permanganate ($KMnO_4$) at room temperature, open to ambient air.

AMNP-1: 20 mg of 1,8-DHN was dissolved in 19.00 mL of ultrapure water and 1.00 mL acetonitrile. 124.9 µL of 1 N $NaIO_4$ was added to the mixture. After 12 h, AMNPs were retrieved by centrifugation (11,000 rpm, 10 min) and washed with ultrapure water five times.

AMNP-2: 20 mg of 1,8-DHN was dissolved in 12.06 mL of 0.1 M HOAc-NaOAc buffer solution (pH= 3.7) and 1.27 mL acetonitrile. 106.6 µL of 1 N $KMnO_4$ was added to the mixture. After 12 h, AMNPs were retrieved by centrifugation (11,000 rpm, 10 min) and washed with ultrapure water five times.

AMNP-3 was prepared by laccase-mediated oligomerization of 1,8-DHN under acetate buffer solution at room temperature.[94] Briefly, 30 mg 1,8-DHN was dissolved in 17.10 mL of 0.1 M HOAc-NaOAc buffer solution (pH= 5.0) and 1.90 mL acetonitrile. Laccase from *Trametes versicolor* (0.66 EU mg^{-1}) dissolved in 1.00 mL of 0.1 M HOAc-NaOAc buffer was added to the mixture. Ambient air was bubbled into the solution for the first 5 min of the reaction, and then the reaction was completed open to ambient air over a period of 24 h. The reaction was quenched by 60 μL of a saturated sodium dithionite solution. AMNPs were retrieved by centrifugation (11,000 rpm, 10 min) and washed with ultrapure water five times.

2.4.2 Synthesis of Polydopamine (PDA) and Silica Nanoparticles

PDA-NPs were synthesized through the oxidation and self-polymerization of dopamine in a solution consisting of water and sodium hydroxide at room temperature.[82] Typically, 150 mL of ultrapure water was fully mixed with 300 mg dopamine hydrochloride under stirring at room temperature for about 15 mins. Subsequently, 1.45 mL of 1 M NaOH was quickly injected into this solution. It was observed that the solution color turned to pale yellow immediately and then gradually changed to black. After 24 h, the targeted PDA-NPs were separated by centrifugation (10,000 rpm, 10 min) and washed with ultrapure water three times.

Silica nanoparticles were synthesized using the modified Stöber method, which utilizes a stepwise silica seed and growth synthesis.[101] Specifically, the silica precursor, tetraethyl orthosilicate (TEOS, 0.48 mL) was mixed with ethanol (8 mL) while stirring for 10 min. Then, a mixture consisting of an ammonium hydroxide solution (28-30%, 0.7 mL), ethanol (8 mL) and ultrapure water (1.2 mL), was continuously added dropwise into the above precursor solution. The silica seeds grew at room temperature under constant stirring for six hours, were collected by

centrifugation (12,000 rpm, 10 min), and were washed with ultrapure water four times. The as-prepared silica seeds (12.6 mg) were dispersed in water (0.6 mL) by sonication, and then mixed with ethanol (4 mL) and ammonium hydroxide (28-30%, 0.4 mL). A solution mixture containing TEOS (0.24 mL) and ethanol (4 mL) was added into the above silica seed solution and reacted under constant stirring for another 85 min. The resulting silica nanoparticles were collected using centrifugation (10,000 rpm, 7 min), and washed with ultrapure water four times.

2.4.3 DPPH Assay for Antioxidant Activity of AMNPs

DPPH radical scavenging activity of AMNPs was measured according to the literature.[97] Briefly, 0.2 mM of DPPH solution in 95% ethanol was prepared before use, and then 100 μL of AMNPs dispersed in water was mixed with 1.8 mL of the DPPH solution. The total amount of AMNPs was varied from 5 to 50 μg in each solution. The scavenging activity was evaluated by monitoring the absorbance decrease at 516 nm after it remained in the dark for 20 min. DPPH radical scavenging activity was calculated as I = [1 - (Ai - Aj)/Ac] * 100%, where Ac is the absorbance of DPPH solution without AMNPs samples, Ai is the absorbance of the samples of AMNPs mixed with DPPH solution, and Aj is the absorbance of the samples of AMNPs themselves without DPPH solution. PDA-NPs were used for comparison and ascorbic acid was used as a positive control. The amount of quenched DPPH per gram of antioxidant was calculated by first obtaining the slope from a linear fit of the scavenging activity. The absolute value of this slope represents the absorbance of quenched DPPH per gram of antioxidant. After making a standard curve of DPPH to convert absorbance to moles, the scavenging activity (mol/g) was obtained for each antioxidant.

2.4.4 Cell Culture and Viability Assay

Primary neonatal epidermal keratinocyte (NHEK) cells were isolated from freshly excised neonatal foreskins and gifted by the Perez-White lab at Northwestern Feinberg School of Medicine. Tissue was collected under a protocol approved by the Northwestern University Institutional Review Board (IRB# STU00009443). Patients' consent for neonatal foreskin tissue (for primary keratinocyte isolation) were not required as these tissues are de-identified and considered discarded material per IRB policy. To isolate the cells, the tissue was treated overnight with dispase and then incubated with 0.25% trypsin with 1 mM EDTA for 10 min at 37 °C. The trypsin was neutralized with FBS, the cells suspended in phosphate-buffered saline (PBS), filtered through a 40 μm sieve, and then centrifuged at 1,000 rpm for 5 minutes. The cell pellets were resuspended in, and subsequently maintained in, M154 medium supplemented with human keratinocyte growth supplement (HKGS), 10 μg/mL gentamicin, 0.25 μg/mL amphotericin B, and 0.07 mM $CaCl_2$, and maintained at 37 °C with 5% CO_2. For differentiation, the cells were plated to confluence in complete media with 0.07 mM $CaCl_2$ for 24 hours, switched to complete media with 0.03 mM $CaCl_2$ for 24 hours, and then switched to media with 1.2 mM $CaCl_2$ (without HKGS) for 24 hours before incubation of the nanoparticles.

For cell viability assays, NHEK cells were maintained at 37 °C with 5% CO_2 in a non-differentiated state. They were incubated with AMNPs, PDA-NPs, or silica nanoparticles at a final concentration of 0.04 mg/mL, the vehicle (sterile water, 2 μL), or 10% DMSO for 24 hours. After 24 hours, they were rinsed with DPBS and then incubated with thiazolyl blue tetrazolium bromide (MTT) at a final concentration of 0.5 mg/mL for 4 hours. The solution was carefully removed and the MTT crystals were dissolved in DMSO and incubated for 15 minutes at 37 °C. Absorbance at

590 nm was recorded and all treatment values were calculated as a percentage of the controls, which were normalized to 100%.

Perinuclear cap formation was imaged using live cells in a humidity controlled chamber maintained at 37 °C and supplemented with 5% CO_2 using a Leica SP5 laser scanning confocal system.

2.4.5 TEM/STEM Imaging

NHEK cells were grown on 13 mm Thermanox™ coverslips and fixed in 0.1 M sodium phosphate or PIPES buffer with 2.5% glutaraldehyde and 2% paraformaldehyde. After a fresh exchange of fixative, the cells were microwave processed using a Pelco Biowave. The samples were post-fixed with 1% OsO_4 in water or 1% OsO_4 in imidazole followed by 1% uranyl acetate. Dehydration occurred with a graded series of ethanol and acetone prior to infiltration with EMBed812 epoxy resin. The cells were embedded flat in upturned BEEM® capsules and the resin polymerized at 60 °C for 48 hours prior to ultramicrotomy in a Leica EM UC7 Ultramicrotome. Ultra-thin sections (60 nm) were post-stained with uranyl acetate and Reynolds lead citrate. Micrographs were obtained on a Hitachi HD2300 cFEG STEM with an HAADF detector at 80 kV. Finally, image contrast was inverted to simulate traditional bright-field TEM images.

For cryogenic TEM images of AMNPs in cell media, 4 µL of suspended AMNP particles was vitrified using a Vitrobot Mark III (ThermoFisher Scientific) operating at 8 °C with > 95% relative humidity. TEM grids were surface plasma treated before the vitrification procedure.

2.4.6 Reactive Oxygen Species (ROS) Assay

NHEK cells were incubated with 0.02 mg/mL AMNPs, PDA-NPs, or silica nanoparticles for 3 days, rinsed with DPBS, and then incubated with 4 μM CM-H$_2$DCFDA in DPBS for 45 minutes at 37 °C. The cells were rinsed with DPBS and then allowed a 10-minute recovery time in complete growth medium at 37 °C. The cells were then subjected to irradiation by a 365 nm, 8 W lamp with an irradiance of 2.25 mW/cm^2 for 2 minutes at a height of 18 mm. Hoechst 33342 was added to each well, incubated for 15 minutes at room temperature, and then the cells were imaged live. A Thorlabs S120VC standard photodiode power sensor was used to determine the irradiance of the lamp

Chapter 3. Porous Allomelanin Nanoparticles for Toxin and Gas Adsorption

3.1 Introduction

Melanin is a versatile pigment found in almost every type of organism on Earth.[1] It serves a variety of known functions in nature such as radiation protection,[6] metal chelation,[102] thermoregulation,[7] and structural coloration.[21] Melanins have also been shown to exhibit more exotic properties such as toxin adsorption in melanic seasnakes[4] and butter clams.[5] For the past decade, the interest in synthetic melanin, specifically human eumelanin, has grown significantly, with the vast majority of studies centered almost entirely around the oxidative polymerization of dopamine to form polydopamine (PDA).[12, 103-105] This inspired us to explore the richer chemistry of melanin beyond PDA for access to new types of function. Specifically, here, we focus on allomelanin-derived 1,8-dihydroxynaphthalene (1,8-DHN), a monomer that is utilized in nature by fungi. Allomelanins, the nitrogen-free family of melanins, are present in nature not as a pure substance, but as a complex material associated with polysaccharides and proteins, although this composition has yet to be quantified.[37, 38] Therefore, an artificial mimic provides an approach

towards pure materials for understanding the unique properties of allomelanin itself. Synthetic allomelanin mimics have only recently been synthesized, using chemoenzymatic and chemical synthetic methods to oligomerize and polymerize 1,8-DHN.[94, 106, 107] The latter affords discrete, spherical particles with low dispersity and with excellent radical scavenging properties.[107] With a straightforward, high-yielding synthesis in hand, we reasoned, based on the chemical structure of the oligomers and polymers generated from 1,8-DHN, that the materials could likely exhibit intrinsic microporosity. This would also suggest that this could be the case for allomelanin produced by organisms. Indeed, structural analogues in synthetic systems include polymers of intrinsic microporosity (PIMs) which have previously utilized naphthalene diol-type co-monomers to afford materials with surface areas of up to 440 m^2/g–540 m^2/g.[108] For PIMs,[109,110,18] the voids created by inefficient packing of the resulting macromolecules gives rise to microporosity and this property could very well provide organisms generating such materials in the form of melanin pigments an evolutionary advantage.

Herein, we report a biomimicry approach to develop synthetic porous materials. We show that amorphous, tunable, high porosity allomelanin nanoparticles can be readily synthesized in a facile manner with minimal reagents. The resulting materials can be used for gas and toxin adsorption, inspiring the intriguing possibility that organisms use 1,8-DHN to generate porous functional materials.

3.2 Results

3.2.1 Preparation of Porous Allomelanin Nanoparticles (AMNP)

Preparation of Spherical/"Solid" Allomelanin Nanoparticles (S-AMNP). Artificial allomelanin was synthesized by oxidative polymerization using 1,8-dihydroxynapthalene (1,8-

DHN) as a precursor. Synthetic allomelanin initially forms as a mixture of mainly dimers and low molecular weight oligomers as oxidative polymerization from 1,8-DHN proceeds over 20 hours (Figure 3.1).[94, 107] This mixture of dimers, trimers and higher order oligomers assemble to form spherical ("Solid") particles (S-AMNP) spontaneously in solution (Figure 3.2). Bright-field, scanning transmission electron microscopy (BF-STEM) reveals uniform, spherical structures (Figure 3.2b,g,l). High-angle annular dark-field STEM (HAADF-STEM) was also performed to view the particles at higher resolution (Figure 3.2c,h,m). Particle surfaces are visible by scanning
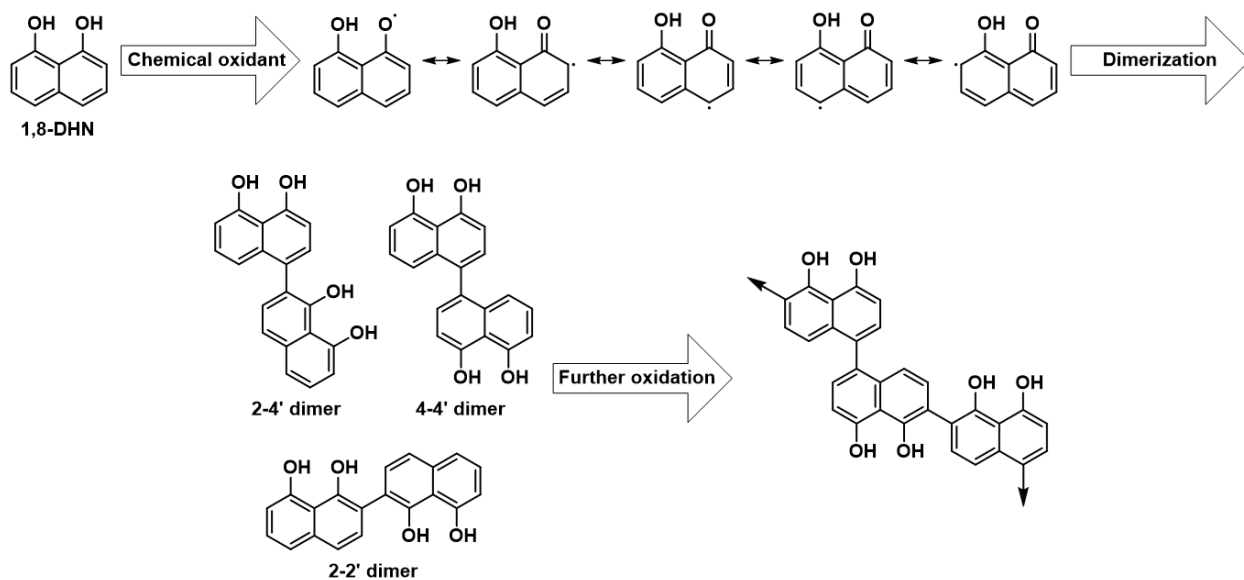
Figure 3.1 Simplified, proposed chemical structure of synthetic allomelanin and putative allomelanin polymer unit. 1,8-DHN is oxidized to form a series of resonance structures which result in various dimer species which can undergo further oxidation to form the final polymer product. The chemical oxidant used in this study was NaIO₄, however KMnO₄ can also be used to form these same structures, and the oxidant chosen affects the distribution of dimers.[107, 111] The final polymer structure is still under investigation.

electron microscopy (SEM) (Figure 3.2d,i,n) and more clearly visible by atomic force microscopy (AFM) (Figure 3.2e,j,o). Over time we observed a visible darkening of the color of the particles in aqueous suspension, from light gray to black, correlated with polymerization and crosslinking.
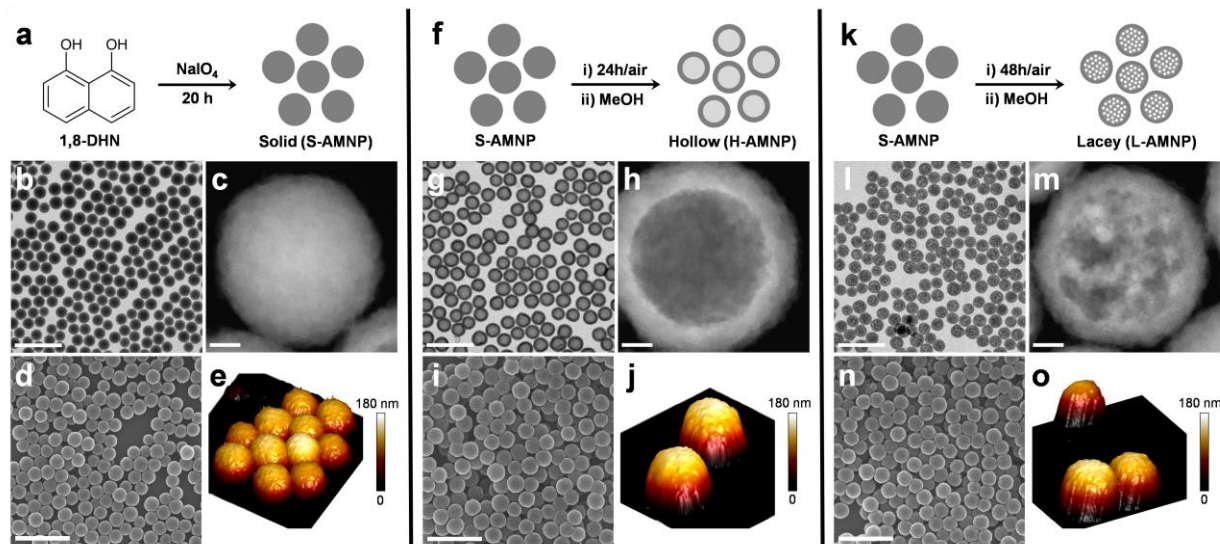
Figure 3.2 Schematic of allomelanin nanoparticle (AMNP) synthesis, with characterization by bright-field scanning transmission electron microscopy (BF-STEM), high-angle annular dark-field STEM (HAADF-STEM), scanning electron microscopy (SEM), and atomic force microscopy (AFM). (a-e) 1,8-DHN is oxidized using $NaIO_4$ to form self-assembled, "Solid" structures (S-AMNP) which can be partially dissolved in MeOH at discrete timepoints to form "Hollow" (H-AMNP, f-j) or "Lacey" (L-AMNP, k-o) nanostructures. (a) S-AMNP synthetic scheme. (b) BF-STEM. (c) HAADF-STEM. (d) SEM. (e) AFM. (f) H-AMNP synthetic scheme. (g) BF-STEM. (h) HAADF-STEM. (i) SEM. (j) AFM. (k) L-AMNP synthetic scheme. (l) BF-STEM. (m) HAADF-STEM. (n) SEM. (o) AFM. All SEM and BF-STEM scale bars 500 nm, and all HAADF-STEM scale bars 20 nm.

UV-Vis absorbance was monitored from 1 to 15 days after synthesis of the S-AMNPs revealing a broadening of the peak at ~250 nm and a shift to longer wavelengths, indicative of expansion of the conjugated system (Figure 3.3). This is coupled with an increase in the visible region as particles further oxidize and become darker in color, consistent with previous observations of these types of systems.[112] Solvent stability was then assessed in preparation for porosity measurements which necessitate the use of ethanol, or a solvent with low surface tension that is miscible with liquid CO_2, for storage prior to supercritical activation. We observed that the initially formed allomelanin nanoparticles partially dissolved in ethanol but became stable in solution after aging, polymerizing and darkening.
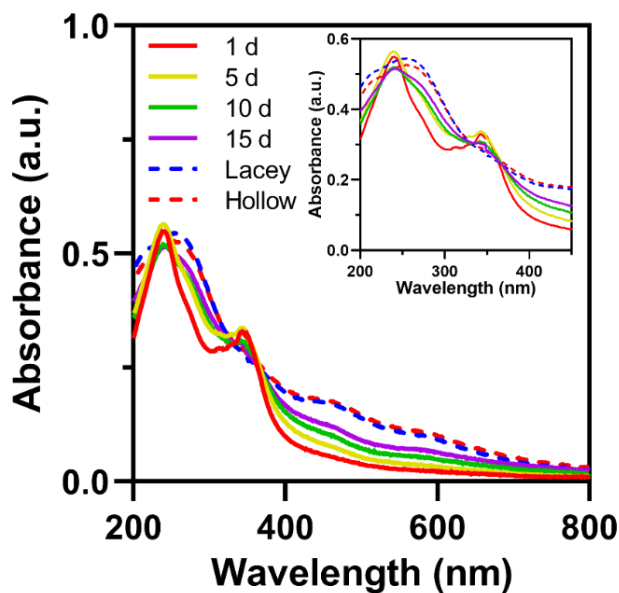
Figure 3.3 UV-Vis of AMNPs over time. Time course following the absorbance of Solid AMNPs (S-AMNPs) at 24 h, 5 days, 10 days, and 15 days post-synthesis. This is in comparison to Lacey and Hollow AMNPs (L- and H-AMNPs, respectively) after their formation from S-AMNPs, subsequent incubation in the MeOH etching solution for 6 days, and dialysis into water. The inset is zoomed into the region between 200 nm and 450 nm for clarity. All AMNPs are suspended in water at 0.008 mg/mL.

Due to the initially observed instability, a solvent screen was performed using several organic solvents with varying polarities to determine the effects on the particles (Figure 3.4). Freshly synthesized AMNPs (24 h after the initial reaction) were solvent switched from water to organic solvent *via* centrifugation at 10,000 rpm for 10 minutes, followed by redispersion at 0.5 mg/mL in the solvent of interest (ethyl acetate (EtOAc), dichloromethane (DCM), acetone, N,N-dimethylformamide (DMF), acetonitrile (ACN), 1-octanol, acetic acid, isopropanol (IPA), ethanol (EtOH), or methanol (MeOH)) and incubated for 1 month in the etching solution. Some solvents (EtOAc, ACN, acetic acid, and EtOH) caused more aggregation than others, which is reflected in the TEM images. Methanol was discovered to have profound effects on the particle morphology in the first 3 days after synthesis, resulting in well-defined structures (Figure 3.5), with

accompanying visual changes in the suspension color both over time and across different solvents (Figure 3.6). Isopropanol also produced well-defined, hollow-looking particles, but only in a sub-population of the particles, and EtOH also produced similar hollow particles, but with less definition. In addition, both EtOH and IPA treatments resulted in particles with a higher degree of aggregation than MeOH. Therefore, subsequent experiments were performed with MeOH as the "etching" solvent. Chemical changes in the dimer content were also observed up to two weeks following synthesis (Figure 3.7). Aliquots from a fresh batch of purified S-AMNP were removed every day for 13 days, pelletized by centrifugation at 14,000 rpm for 8 minutes, the supernatant removed, and the particles re-suspended by vortexing in MeOH to a final concentration of 0.5 mg/mL. The solution/suspension was then re-pelletized by centrifugation at 14,000 rpm for 8 minutes and the supernatant analyzed by HPLC.
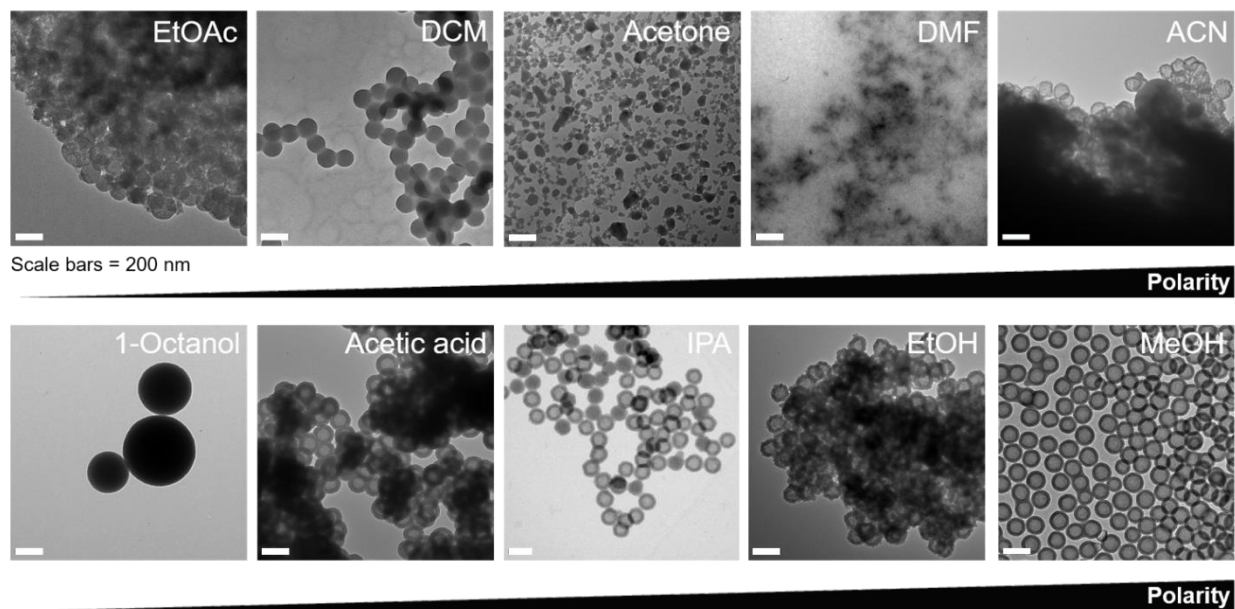
Figure 3.4 Solvent stability screening of S-AMNPs. Images arranged by increasing solvent polarity from left to right in the top row, and then continuing left to right in the bottom row. Micrographs were acquired on a JEOL 1230 TEM operating at 80 kV.

Incubation time with MeOH post-etch

Time post-reaction before etching with MeOH

| | 24 h | 48 h | 72 h | 4 d | 5 d | 6 d |

Scale bars 200 nm
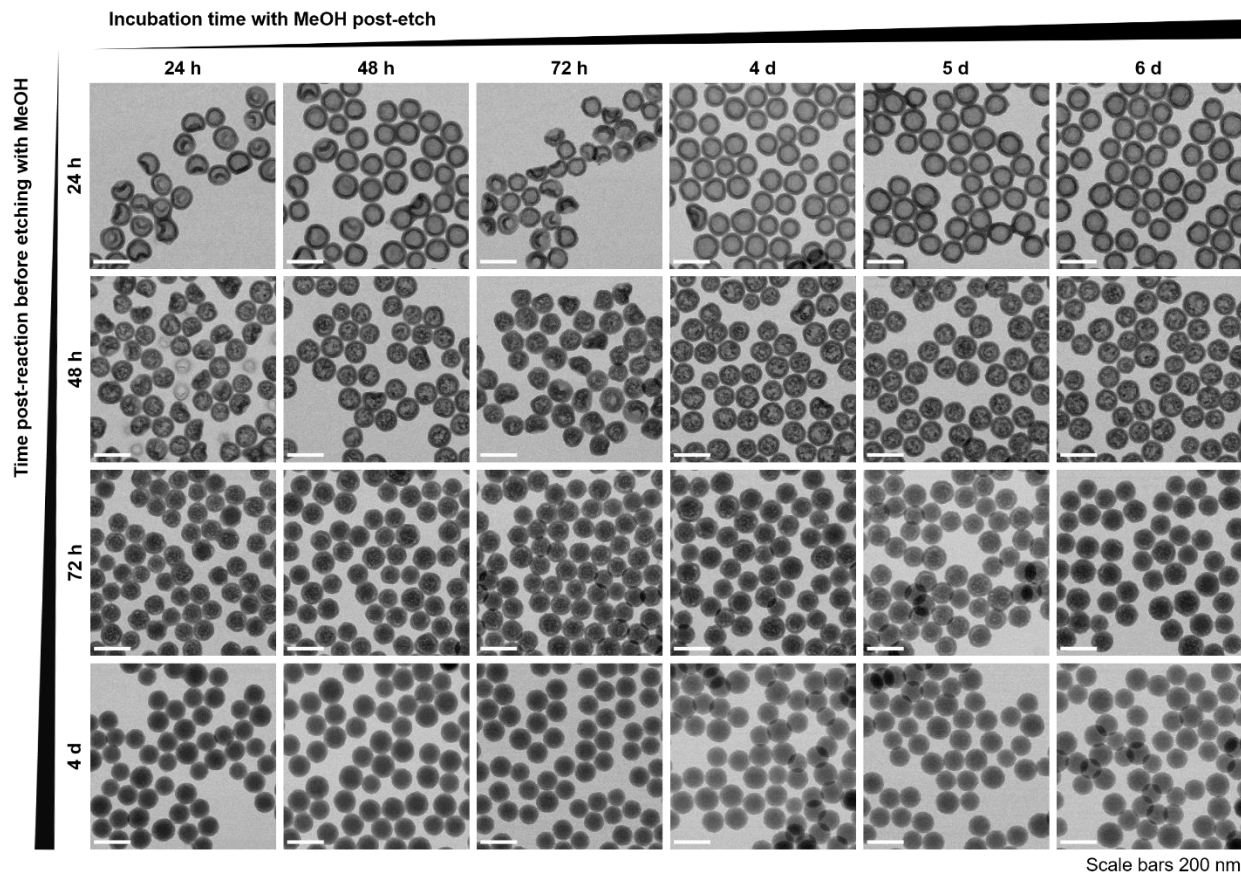
Figure 3.5 STEM timeseries showing the etching of S-AMNPs and subsequent formation of L- and H-AMNPs. Freshly synthesized S-AMNPs were solvent switched to MeOH between 1 and 4 days after synthesis (rows). In each of those conditions, they were incubated for between 1 and 6 days in the same MeOH etching solution, followed by dialysis into water (columns). The particles are more well-defined, and with less collapsed structures after 5 or 6 days in the MeOH solution containing the etched species. H-AMNPs are best obtained upon solvent switching to MeOH 24 h post-reaction, and L-AMNPs are best obtained 48 h post-reaction. A slightly etched structure can be obtained after 72 hours, resembling L-AMNP but to a lesser degree, and 4 days post-reaction, the particles are stable enough in MeOH that there are no visible morphological changes, as observed by STEM. Images were acquired on a Hitachi HD2300 STEM operating at 200 kV.

Freshly synthesized S-AMNPs stored at room temperature in water release dimer over time, but this shedding decreases over the first two weeks after synthesis. This indicates that the particles take approximately two weeks to fully oxidize, although more studies are needed to investigate the role of the dimers and other oligomers in the final, oxidized structure.
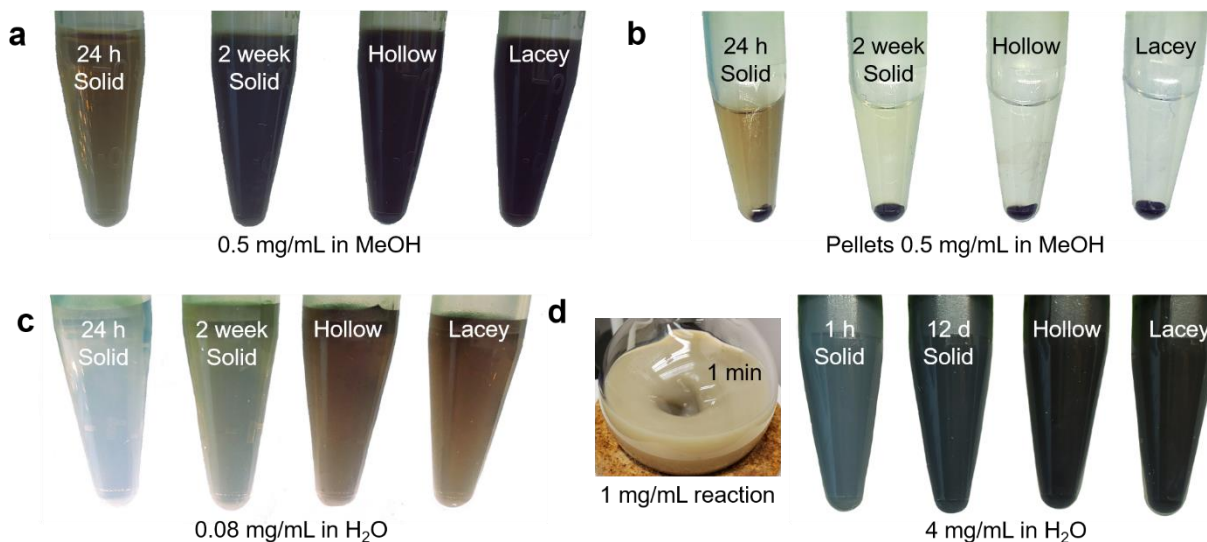
Figure 3.6 Photographs of AMNPs in MeOH or Milli-Q water at different timepoints and at different concentrations. (a) S-AMNPs were dispersed in MeOH at 24 h or 2 weeks after the initial reaction, and L-AMNPs and H-AMNPs were re-dispersed in MeOH after the etching and incubation process was completed and after the particles were dialyzed into water for purification. All AMNPs shown at 0.5 mg/mL in MeOH. (b) Tubes from a were pelletized by centrifugation at 10,000 rpm for 10 minutes. (c) AMNPs were dispersed in water at 0.08 mg/mL (subsequently diluted 10X for UV-Vis analysis, see Figure 3.3). (d) S-AMNPs forming in the initial reaction mixture (1 mg/mL in H_2O/ACN) 1 minute after injection of the $NaIO_4$ oxidant, or at 4 mg/mL 1 h or 12 d after the reaction was completed (particles were clean and purified). L- and H-AMNPs at 4 mg/mL in water after the etching, incubation, and dialysis process was completed. The concentration was re-measured after dialysis.
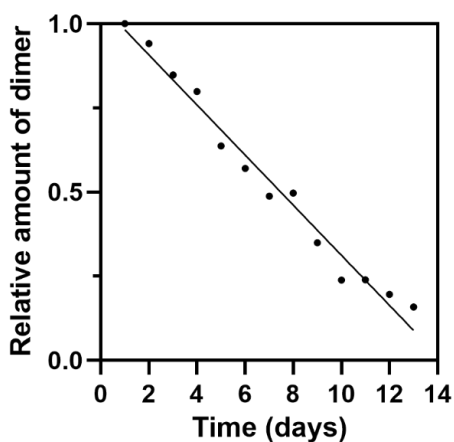
Figure 3.7 Relative amount of 1,8-DHN dimer shedding from S-AMNP over time as the particles "age" (oxidize further) in water. The amount of dimer in the supernatant was plotted as a function of time, with the starting concentration at 24 hours normalized to 1.

Preparation of Hollow Allomelanin Nanoparticles (H-AMNP). As observed by STEM, the aging process for generating AMNPs corresponds with an increase in solvent compatibility. The observations also resulted in the serendipitous discovery that particles aged for 24 h could be etched to well-defined, Hollow AMNPs (H-AMNP) (Figure 3.2f-j and Figure 3.5). STEM micrographs show uniform, hollow structures (Figure 3.2g) that are more clearly visible by HAADF-STEM, wherein there appears a clear distinction between the hollow core and the shell (Figure 3.2h). H-AMNPs were ultramicrotomed to 80 nm sections, and imaged *via* STEM, revealing a hollow core (Figure 3.8). The particles persist as stable suspensions when stored in water at room temperature for at least 18 months, with no indication of aggregation (Figure 3.9).
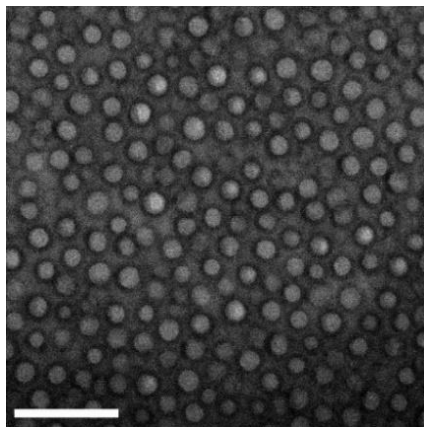
Figure 3.8 STEM micrograph of H-AMNPs, resin-embedded and sectioned to 80 nm thickness. The sample was not post-stained after sectioning. Scale bar 500 nm.

A zeta potential titration was also performed at a wide range of pH values to ascertain the isoelectric point and to quantify the observed stability of AMNPs over time (Figure 3.10). The initial pH values of the stored suspensions in Milli-Q water were 3.48, 3.95, and 3.92 for S-AMNP, L-AMNP, and H-AMNP, respectively, and the pH of the pure water used was 5.24. Suspensions of AMNPs stored over time in water (see Figure 3.9) were adjusted to 0.25 mg/mL, and pH 0, 2, 4, 6, 8, 10, or 12 by the addition of HCl or NaOH. The particles were stable, with large, negative
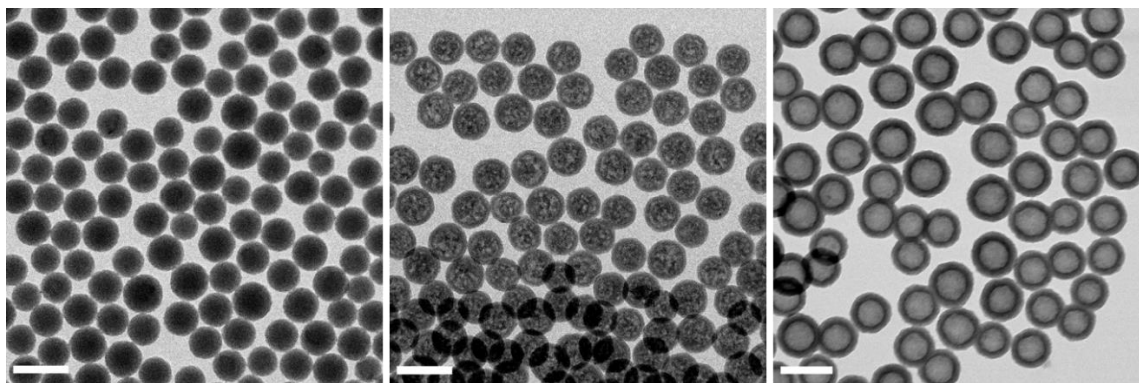
Figure 3.9 STEM micrographs of S-AMNPs (left), L-AMNPs (middle), and H-AMNPs (right), imaged 18 months after synthesis. The particles were stored in water on the benchtop at room temperature. Imaging was performed on a Hitachi HD2300 STEM operating at 200 kV. Scale bars 200 nm.

zeta potentials within a large range of pH values, namely at or above pH ~3.5, and with the lowest values occurring for pH ~6-10. The isoelectric point (zeta potential is approximately 0 mV) occurred at pH ~0.
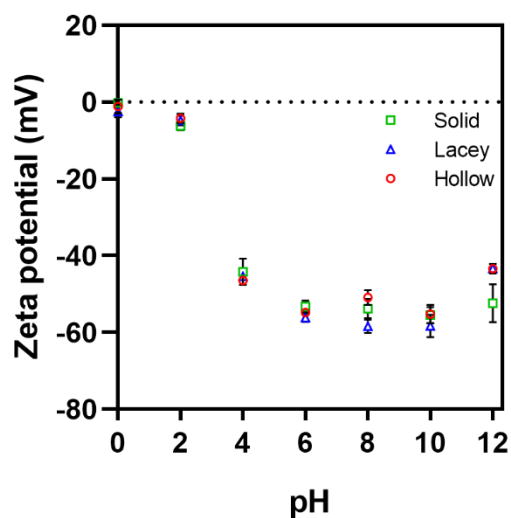
Figure 3.10 Zeta potential titration of S, L-, and H-AMNPs. AMNPs stored in Milli-Q water were adjusted to 0.25 mg/mL and pH 0, 2, 4, 6, 8, 10, or 12 using NaOH or HCl, prior to zeta potential measurement.

Preparation of Lacey Allomelanin Nanoparticles (L-AMNP). With a method for routinely generating hollow, spherical H-AMNPs, we reasoned that further aging followed by etching with methanol would lead to a higher surface area particle, with more internal structure (Figure 3.2k-o and Figure 3.5). STEM micrographs show structures which are an intermediate between S- and H-AMNP, with material density in the center having a lacey appearance (Figure 3.2l). HAADF-STEM imaging reveals the core of the particle with small voids throughout (Figure 3.2m). We hypothesized that this was due to the re-deposition process of leached oligomers back onto the particle surface where they are further oxidized as a polymeric shell.

3.2.2 Characterization of AMNP

We next conducted light and x-ray scattering studies to ascertain the dispersity, morphology, and fine structure of the materials in bulk solution (Figure 3.11 and Figure 3.12). First, AMNPs were analyzed using multi-angle dynamic light scattering (DLS) (Figure 3.11a-c and Figure 3.12a) and static light scattering (SLS) in water (Figure 3.12b).
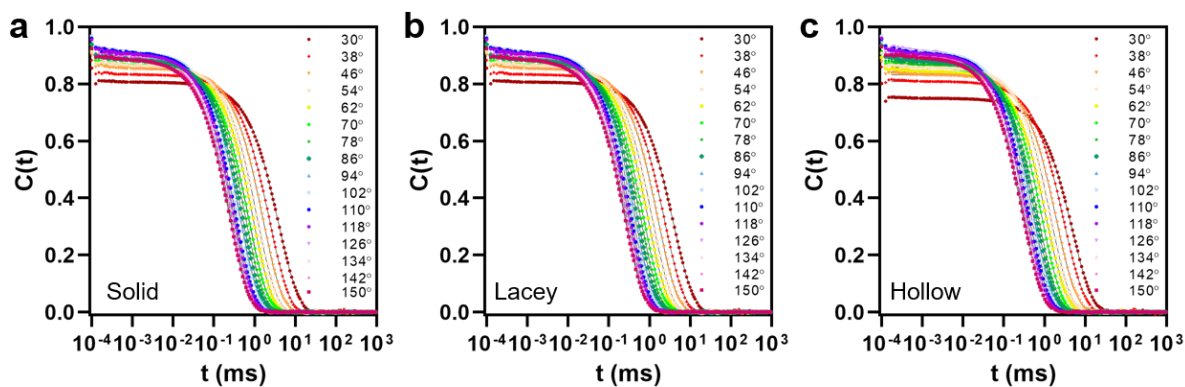
Figure 3.11 Autocorrelation functions from DLS measurements. (a) Solid (S-AMNP). (b) Lacey (L-AMNP). (c) Hollow (H-AMNP).
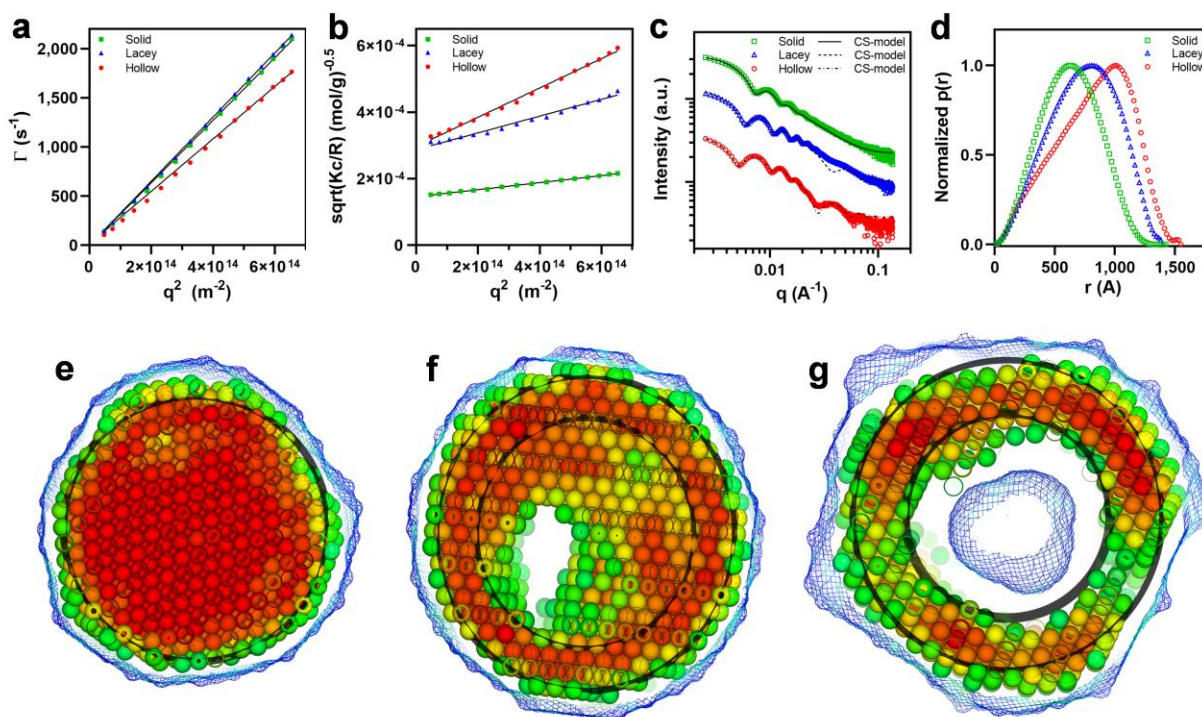
Figure 3.12 Scattering analysis of Solid (S-AMNP), Hollow (H-AMNP), and Lacey (L-AMNP) nanoparticles using dynamic light scattering (DLS), static light scattering (SLS), and small-angle x-ray scattering (SAXS). (a) DLS plot of the average decay rate of the autocorrelation function (Γ), *vs* the square of the scalar magnitude of the scattering vector (q^2), showing the particles have high uniformity. (b) SLS plot for deriving the radius of gyration (R_g). (c) SAXS patterns for AMNPs and scattering patterns from spherical core-shell (CS) geometric modeling. (d) Normalized pair distance distribution functions (p(r)). (e-g) Representative cross-sections (each 400 Å thick) of the average dummy atom modeling (DAMs) for S-, L, and H-AMNPS, respectively. Color coding represents the normalized bead probability from 0 (blue) to 1 (red); only beads with occupancy > 1/3 are shown. Blue mesh represents the surface of all the beads with occupancy > 0.1, accessible to an imaginary 180 Å solvent molecule. The cross-sectioned black spheres are for comparison only and have the same radii as the nanoparticle dimensions determined by core-shell modeling of the experimental SAXS.[113]

Hydrodynamic diameters (D_h) of 154 nm (S-AMNP), 150 nm (L-AMNP), and 184 nm (H-AMNP) were determined by DLS (Equation 3.1 and Equation 3.2). The effective radius of gyration (R_g) was obtained *via* multiangle SLS with the parameter $\rho = R_g/R_h$ giving an estimate of the compositional distribution of the particles. AMNP R_g values were determined to be 66 nm (S-AMNP), 73 nm (L-AMNP), and 94 nm (H-AMNP), with ρ values of 0.86 (S-AMNP), 0.97 (L-

AMNP) and 1.02 (H-AMNP) corresponding to solid spheres in the case of S-AMNP, with an increasing distribution of mass towards the shell, commensurate with that observed by STEM, for L- and H-AMNP, respectively. The effective diffusion coefficient (D_{eff}) was primarily invariant with q^2 for all samples, with this angular independence indicative of their low dispersity (Figure 3.13).
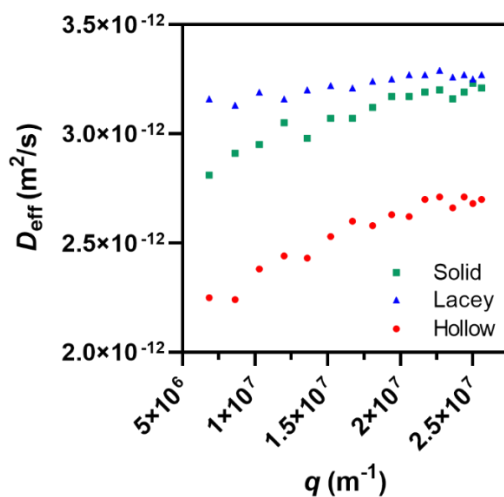
Figure 3.13 Effective diffusion coefficient (D_{eff}) plotted as a function of scattering vector (q). Polydispersity indices (PDI) for the Solid, Lacey, and Hollow particles are 0.17, 0.21, and 0.08, respectively.

Small-angle X-ray Scattering (SAXS) was performed on AMNPs that were synthesized 1 month prior to measurement and compared to that of a "fresh" S-AMNP sample synthesized 48 hours prior (see also Equation 3.4). The 1D SAXS patterns from each nanoparticle sample were fit with a spherical core-shell (CS) model using a Gaussian distribution (Figure 3.12c). In the case of S-AMNP, to minimize contributions of the shell thickness the shell was fixed to 0.001 Å, and the X-ray scattering length density of the shell constrained to match that of solvent (H_2O, 9.42×10^{10} cm^{-2}). Through these constraints, the core-shell model mathematically reduces to be very similar
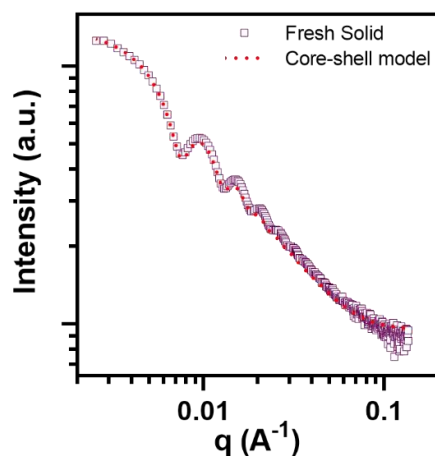
AMNP	Core radius (Å)	Shell thickness (Å)	Total radius (nm)	Core ρ ($\times 10^{10}$ cm^{-2})	Shell ρ ($\times 10^{10}$ cm^{-2})	Solvent ρ ($\times 10^{10}$ cm^{-2})
Fresh Solid	600 ± 55	0.001	60.0	12.434	9.42	9.42

Figure 3.14 SAXS pattern and corresponding core-shell modeling parameters of Fresh Solid AMNPs (Fresh S-AMNPs) synthesized 48 hours before the measurement.

to that of a solid spheroid. To further confirm this, no appreciable difference was observed in the quality of fit or the modeled radius for the solid melanin nanoparticles modeled with either a simple spheroid or the constrained core-shell model as shown in Figure 3.14 and Figure 3.15. This allowed for the direct comparison of parameters across the three melanin nanoparticles using the same geometrical model.

We also analyzed the pair distance distribution function (p(r)) with D_{max} (the maximum diameter of the particle) determined (Figure 3.12d and Figure 3.16). S-AMNPs follow a normal distribution as expected for solid spherical nanoparticles of smooth surface and uniform density. H-AMNPs display skewed distribution in p(r) to higher r values as expected for a hollow interior and significant shell density.
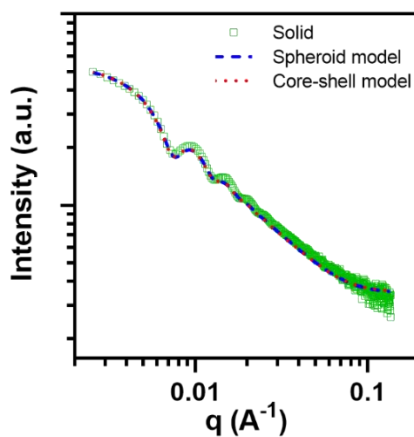
Figure 3.15 SAXS pattern of S-AMNPs (green circles) with spheroid (blue dashed line) and core-shell model (red dashed line) for comparison of geometrical models.
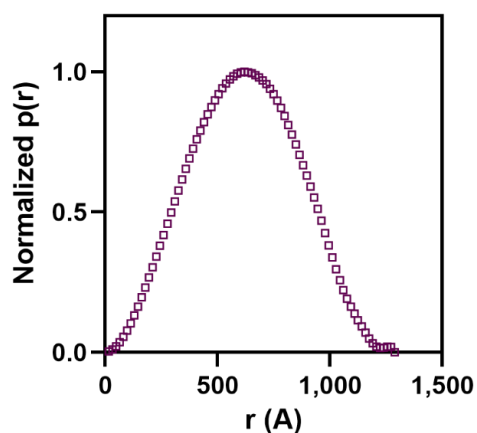
Figure 3.16 Normalized pair distance distribution function (p(r)) for Fresh Solid AMNPs (Fresh S-AMNPs).

Finally, L-AMNPs demonstrate peak broadening and skewness suggesting inhomogeneity within the core. The D_{max} for S- (142.4 nm), L- (140.0 nm) and H- (155.0 nm) AMNPs is in strong agreement with values calculated from core-shell modeling of X-ray scattering and those observed also by light scattering experiments. Modeling demonstrates H-AMNP have the largest overall particle radius of 71 nm and greatest shell thickness of 23 nm. In comparison, S-AMNP exhibited

Table 3.1 Summary of experimental SAXS measurements determined by the core-shell (CS) model.

AMNP	Core radius (Å)	Shell thickness (Å)	Total radius (nm)	Core ρ ($\times 10^{10}$ cm^{-2})	Shell ρ ($\times 10^{10}$ cm^{-2})	Solvent ρ ($\times 10^{10}$ cm^{-2})
Solid	611 ± 65	0.001	61.1	13.553	9.42	9.42
Lacey	526 ± 56	162	68.8	11.220	13.545	9.42
Hollow	483 ± 61	227	71.0	9.281	12.245	9.42

the smallest total radius of 61 nm and L-AMNP a total radius of 69 nm with a shell contribution of 16 nm (Table 3.1). 3D reconstructions (Figure 3.12e-g) reveal structures in good agreement with STEM, AFM, and light scattering data (Table 3.2). R_g and R_g/R_h were determined from SLS data.

Table 3.2 Comparison of morphology and size using DLS, SLS, SAXS, STEM, and AFM analyses.

AMNP	$D_{h,\ DLS}$ (nm)	R_g (nm)	R_g/R_h	$D_{h,\ SAXS}$ (nm)	D_{STEM} (nm)	D_{AFM} (nm)
Solid	154	66	0.86	122	108 ± 9	124 ± 10
Lacey	150	73	0.97	138	123 ± 9	131 ± 9
Hollow	184	94	1.02	142	128 ± 10	141 ± 7

The SAXS analysis software suite ATSAS was used to further investigate the melanin nanoparticle structures using an *ab-initio* dummy atom modeling (DAM) approach. In this approach, each atom/bead represents an occupied volume element of either particle phase or solvent phase.[113] These beads are initially randomly assigned phases after which point the calculated scattering of the modeled particle is refined against the experimental scattering data by randomly switching the phase of the beads, while gradually reducing the probability of accepting those changes that do not improve the fit (Figure 3.17 and Figure 3.18, Table 3.3). Renderings of the averaged DAMs for each nanoparticle, with the bead occupancy probability color coded from

0 to 1 (blue to red, respectively) support the differences observed between melanin nanoparticles

(Figure 3.12e-g). Hence red represents a high probability that the bead position is occupied across
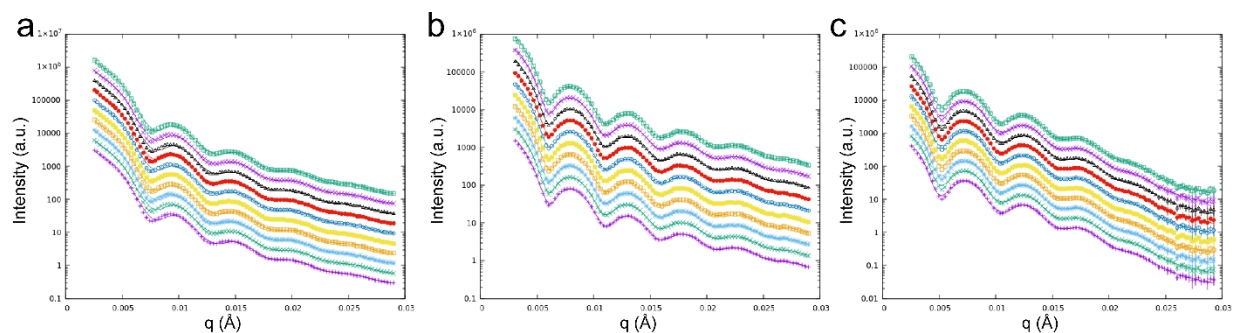
Figure 3.17 Ten individual DAMMIF modeling runs for AMNPs. (a) Solid (S-AMNP). (b) Lacey (L-AMNP). (c) Hollow (H-AMNP). X-ray scattering data displayed as symbols with the DAM fit for each individual run represented with the line. Each modeling run has been vertically offset for clarity.
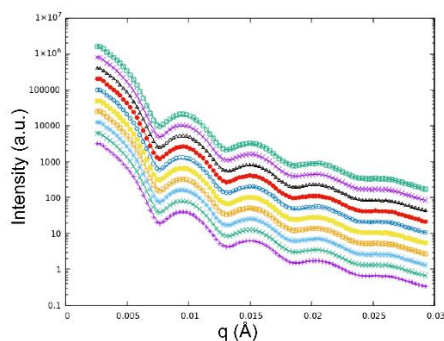
Figure 3.18 Ten individual DAMMIF modeling runs for Fresh Solid (Fresh S-AMNP) nanoparticles. X-ray scattering data displayed as symbols with the DAM fit for each individual run represented with the line. Each modeling run has been vertically offset for clarity.

the averaged DAM through to blue representing a low probability for this bead position. DAM for

S-AMNP matches the core-shell modeled sphere of radius 61 nm and has a uniform high

probability of bead occupancy throughout the nanoparticle (Figure 3.12e). The average DAM for

L-AMNP exhibits a core-shell structure which is in strong agreement with core-shell fitting with

low probabilities for bead occupancies throughout the core of the nanoparticle suggesting a

randomly dispersed lacey internal structure (Figure 3.12f). Finally, the average DAM of H-AMNP

Table 3.3 Modeling parameters derived from *ab initio* dummy atom modeling of AMNPs.[a]

AMNP	$R_{g,real}$ (Å)	$R_{g,reciprocal}$ (Å)	$R_{g,aDAM}$ (Å)	D_{max} (Å)	NSD	FSC resolution (Å)
Solid	474.3 ± 1.3	476.1	476.3	1423.5	0.543 ± 0.012	180 ± 13
Lacey	558.2 ± 0.2	561.8	560.3	1400	0.672 ± 0.006	227 ± 16
Hollow	621.0 ± 0.6	626.3	624.4	1550.1	0.768 ± 0.013	249 ± 17
Fresh Solid	470.9 ± 0.3	473.4	472.9	1289.5	0.567 ± 0.013	193 ± 14

[a] For each particle, the real and reciprocal space radius of gyration fitted by DATGNOM agree with eachother, as does the final R_g as calculated from the averaged DAM. Additionally the normalized spatial discrepancy of all ten seperately refined aligned models of a particle are below 1, indicative of the individual models sharing a high degree of similiarity for each nanoparticle.[113] The variability of the aligned models as analyzed by FSC suggests a true resolution of these models is around 180 to 250 Å. This knowledge is used to guard against over interpretation of small features in the averaged DAMs. $R_{g,real}$ = radius of gyration from real space, $R_{g,recirocal}$ = radius of gyration calculated from reciprocal space, $R_{g,aDAM}$ = radius of gyration from the average dummy atom model, D_{max} = maximum dimension, NSD = normalized spatial discrepancy, FSC resolution = Fourier shell correlation resolution. $R_{g,real}$, NSD, and FSC resolution data all displayed as mean ± standard deviation.

has a shell of significantly high bead occupancy probability, with a hollow core in good agreement with core-shell fitting analysis (Figure 3.12g). Average DAM of fresh S-AMNPs produced a model with similar characteristics to aged S-AMNPs (Figure 3.19). Representative cross-sectional slices (400 Å thick) of the average DAM for Fresh Solid (Fresh S-AMNPs) were rotated through three different imaging planes and color coded to represent the normalized bead probability from 0 (blue) to 1 (red). From the *ab initio* modeling it is important to note that the spherical imperfections evident in the nanoparticle average DAMs could be representing real nanoparticle imperfections, or they could be an artifact of sample polydispersity, insufficient low-q data, inter-particle interference, and the modeling method.
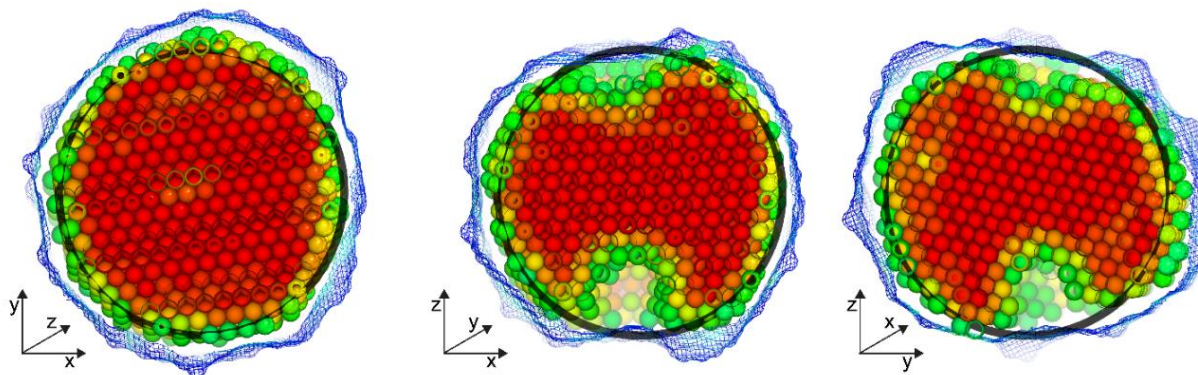
Figure 3.19 Representative cross-sectional slices (400 Å thick) of the average DAM for Fresh Solid (Fresh S-AMNPs) rotated through three different imaging planes. Color coding represents the normalized bead probability from 0 (blue) to 1 (red); only beads with occupancy > 1/3 are shown. Blue mesh represents the surface of all the beads with occupancy > 0.1, accessible to an imaginary 180 Å solvent molecule. The cross-sectioned black spheres are for comparison only and have the same radii as the nanoparticle dimensions determined by core-shell modeling of the experimental SAXS data.

3.2.2 Mechanistic STEM Analysis

Scattering experiments and initial STEM imaging led us to form the hypothesis that at early timepoints after synthesis, S-AMNP retain a "molten core" of loosely associated small oligomers that can be dissolved in organic solvent. These small molecules can then leach out of the micropores into solution, where they eventually redeposit back onto the particle surface over time as the etching solution remains in contact with the particles. Hollow particles are formed by etching at an earlier timepoint, therefor the core is less oxidized and more susceptible to dissolution, whereas just 24 hours later, the etching process leads to lacey particles due to increasingly oxidized particles which are less susceptible to dissolution by MeOH. To further probe the mechanistic details of formation of the various morphologies of AMNPs, and to test our hypothesis of the formation process, high-angle dark-field scanning electron microscopy (HAADF-STEM) images were obtained and analyzed for size and material density distribution throughout the particles (Figure 3.20). For these studies, and due to the distinct morphologies, a mixture of 1:1:1

Solid:Lacey:Hollow AMNP was analyzed on a single lacey carbon TEM grid to provide a uniform background signal for the intensity measurements (Figure 3.20a). The S- and L-AMNP diameters were measured as well as the H-AMNP inner diameter (ID) and outer diameter (OD). The frequency distribution shows that H-AMNP OD increases in relation to the amount of material dissolved from the inside of the particle. H-AMNPs lose the most material from inside the particle
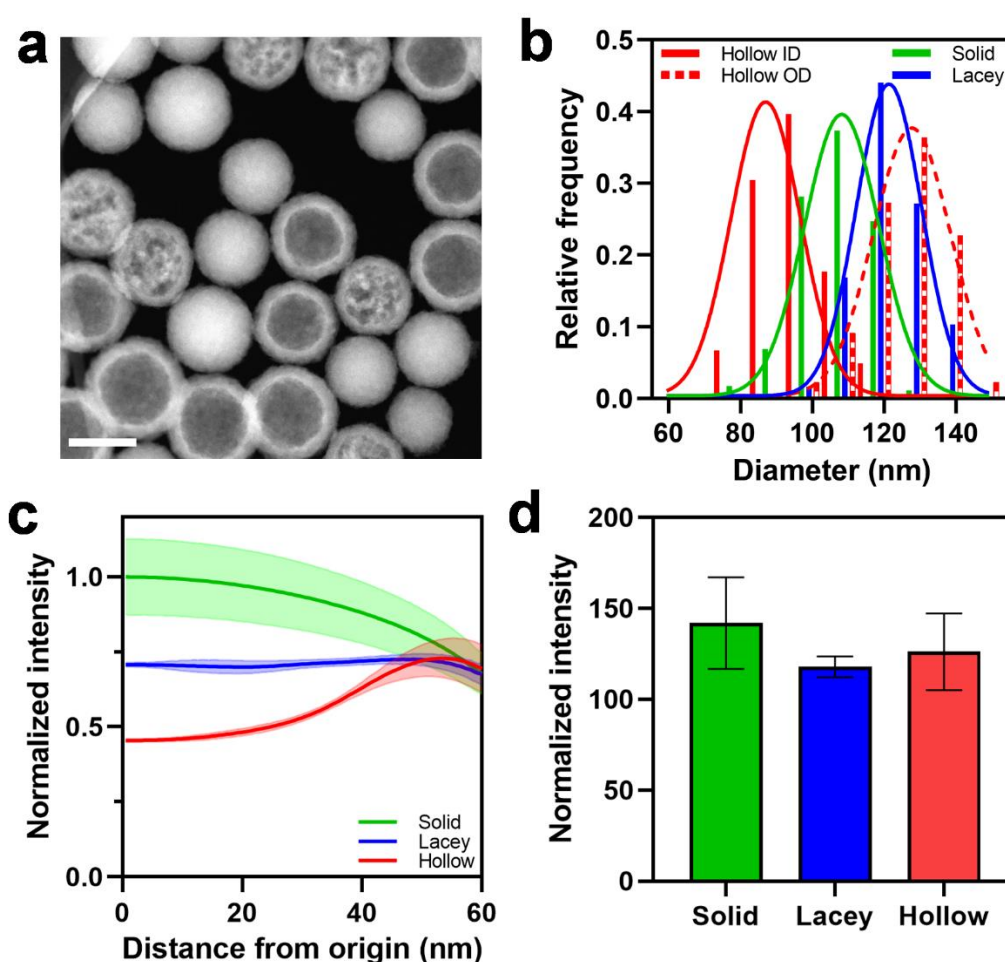
Figure 3.20 HAADF-STEM analysis of AMNPs. (a) HAADF-STEM micrograph of 1:1:1 Solid:Lacey:Hollow AMNP mixture used for size and intensity analyses. (b) Frequency distributions for S- and L-AMNP diameters as well as the inner (ID) and outer (OD) diameters of H-AMNP. (c) Normalized intensity as a function of the distance from the center of a single AMNP. The lightly colored area around each curve is the standard deviation of the measurements of at least 4 AMNP particles. (d) Average total intensity of AMNPs normalized by area.

and therefore have the largest OD. The H-AMNP ID is smaller than the OD of the S-AMNP, indicating that some of the original S-AMNP shell remains as material is lost from the inner volume (Figure 3.20b).

To quantify the relative difference in volume of the material within the particle, we measured the intensity profile from the center to the periphery of individual nanoparticles (Figure 3.20c and Figure 3.21). Indeed, the relative volume of the material follows expected trends, with S-AMNPs the most densely packed in the core, and H-AMNPs the least. For all three particles, the outer "shells" converged to the same relative volume of material.
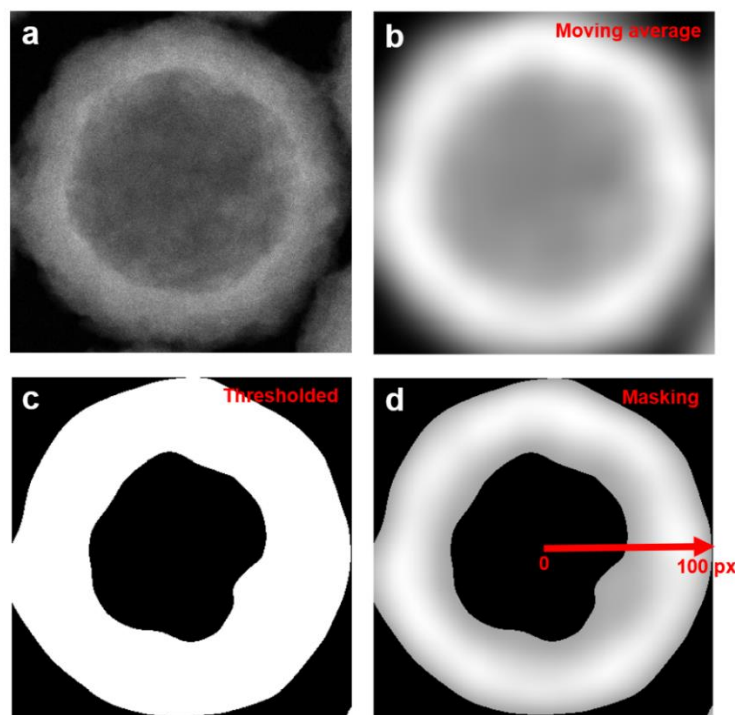
Figure 3.21 Image analysis sequence for STEM intensity measurements from Figure 3.20. Intensity from the masked image is summed and normalized. (a) Raw H-AMNP HAADF-STEM image. (b) Moving average. (c) Thresholding. (d) Masking. Analysis was performed in MATLAB.

To clarify whether there was a conservation of material between AMNPs, the total intensity of the particle was normalized by area of the particle (Figure 3.20d). Here, irrespective of their morphology, normalized intensity is almost the same for all the analyzed particles, indicating negligible loss of material between the particles. This is consistent with the mechanism of formation of L- and H-AMNPs leaching oligomers from their cores and redepositing them onto the particle surface, growing the OD of the particle using core material. This process is better elucidated in Figure 3.22, which illustrates how when Fresh S-AMNP are solvent-switched into MeOH, monomers/dimers/oligomers from the center diffuse out of the particles through micropores, and diffused species re-deposit onto the surface of the particle with incubation over time. This process results in H-AMNP, a hollow particle with a larger diameter than the parent S-AMNP.
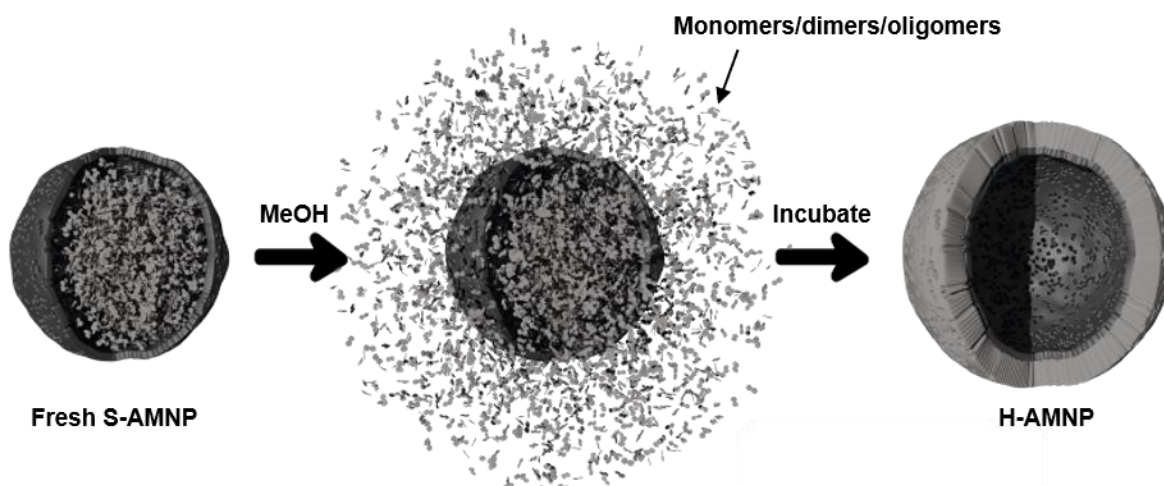
Figure 3.22 Schematic of H-AMNP formation. Fresh S-AMNP are etched in MeOH. Their cores contain loosely associated monomers/dimers/oligomers which dissolve in the MeOH and escape the particles through micropores. Over time, during incubation with the etching solution, these dissolved species redeposit onto the surface of the particles, growing the outer shell.

Some of the initial parent S-AMNP shell remains in H-AMNP, which is evidenced by H-AMNP inner diameters (ID) which are smaller than S-AMNP outer diameters (OD). Formation of L-AMNP follows the same mechanism, but as the initial S-AMNP is slightly more oxidized before MeOH treatment, less material diffuses from the core, resulting in a final particle with a diameter intermediate between S-AMNP and H-AMNP. This mechanism reflects the frequency distribution shown in Figure 3.20b. This is also consistent with the STEM timeseries that shows that particles etched at 24 or 48 h but not incubated over several days with the etching solution have shells that collapse when dried onto a TEM grid (Figure 3.5). The shells are very thin upon initial etching so that the spherical structures collapse easily, but over time, as more monomer/dimers/oligomers in solution redeposit onto the outside of the particles, the shells become thick enough that the particles are stable to deformation. It is unknown whether the etched species (monomers/dimers/oligomers) first oxidize prior to re-deposition onto the particles, or whether they deposit onto the surface and then further crosslink. The crosslinking mechanism and resulting chemical structure also remain unknown, and future studies should investigate these processes more thoroughly.

3.2.4 Sorption Measurements

To assess the porosity of AMNPs, nitrogen physisorption measurements were performed at 77 K. The particles were first activated using supercritical CO_2 and did not have any significant changes in morphology before and after activation (Figure 3.23). Nitrogen isotherms revealed Brunauer-Emmett-Teller (BET) areas of 680 m^2/g for S-AMNPs, 645 m^2/g for H-AMNPs, and 860 m^2/g for L-AMNPs (Figure 3.25). DFT calculations showed two major pores around 6 Å and 12 Å for all AMNPs, although L-AMNP pore volume (0.60 cm^3/g) was significantly higher than for S- (0.35 cm^3/g) or H- (0.36 cm^3/g) AMNPs (Figure 3.20b) which is consistent with the larger
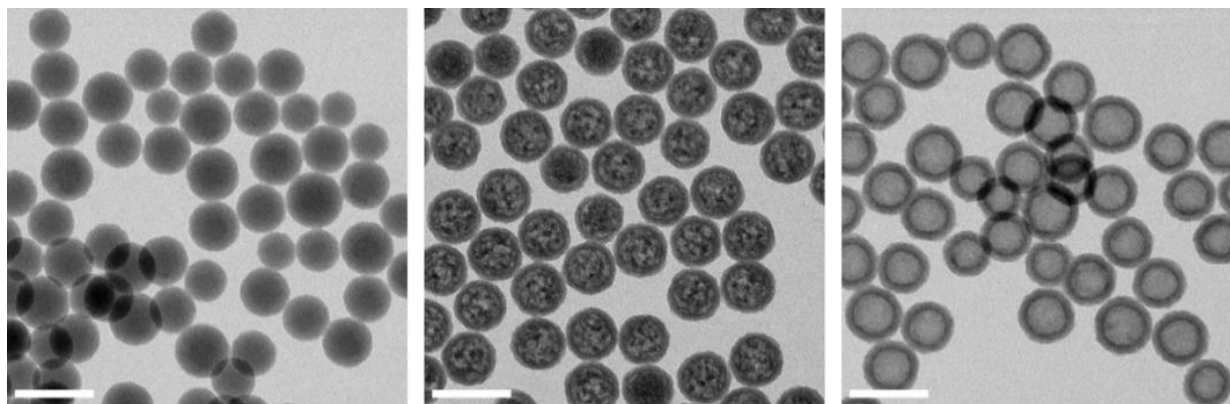
Figure 3.23 STEM micrographs of AMNPs recovered after critical activation for BET sorption measurements. There is no visible morphological change before and after the measurements. Left to right- Solid (S-AMNP), Lacey (L-AMNP), and Hollow (H-AMNP). Scale bars 200 nm.

voids seen *via* HAADF-STEM. Based on our pore-size distribution analysis, there were no distinct

mesopores present in L-AMNPs. Although from the STEM data we can see mesoporous voids,

based on the surface characterization conducted from the N_2 isotherms, we believe that these

mesopores are highly irregular in size and present only in low concentrations.
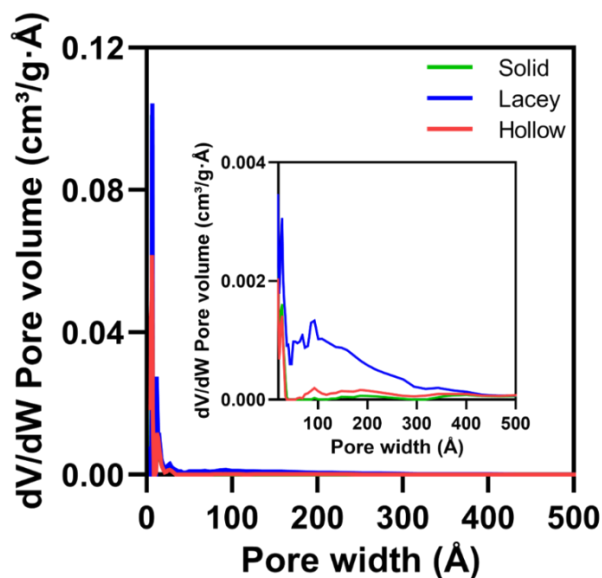
Figure 3.24 Pore size distribution from 0 Å to 500 Å. Two major micropores appear around 6 Å and 12 Å (see Figure 3.25b). Inset shows the mesoporous range (20-500 Å), zoomed in to reveal a low concentration of mesopores for Lacey particles (L-AMNP), and even less for Solid particles (S-AMNP) and Hollow particles (H-AMNP).

Beyond 2 nm, the dV/dW pore volume is close to zero, which points to the low quantity of these mesopores in our materials (Figure 3.24). We hypothesized that due to the -OH groups present on the surface of the porous AMNPs, these materials would be promising for ammonia capture and/or storage.[114] Therefore, we conducted ammonia isotherms at 298 K (Figure 3.25c). The samples were degassed and placed under vacuum (P/P_0 ~10^{-6}-10^{-7}) prior to measurements. The ammonia isotherms showed steep and high uptakes at lower pressures arising from strong interactions between the AMNPs and NH_3, which indicates that these materials would be promising for air filtration applications. At 1 bar, NH_3 uptakes for the S-, L-, and H-AMNPs were 17.0 mmol/g, 12.6 mmol/g, and 11.6 mmol/g, respectively. We hypothesize that S-AMNP had the highest NH_3 uptake due to an increase of functional group density per gram of material.
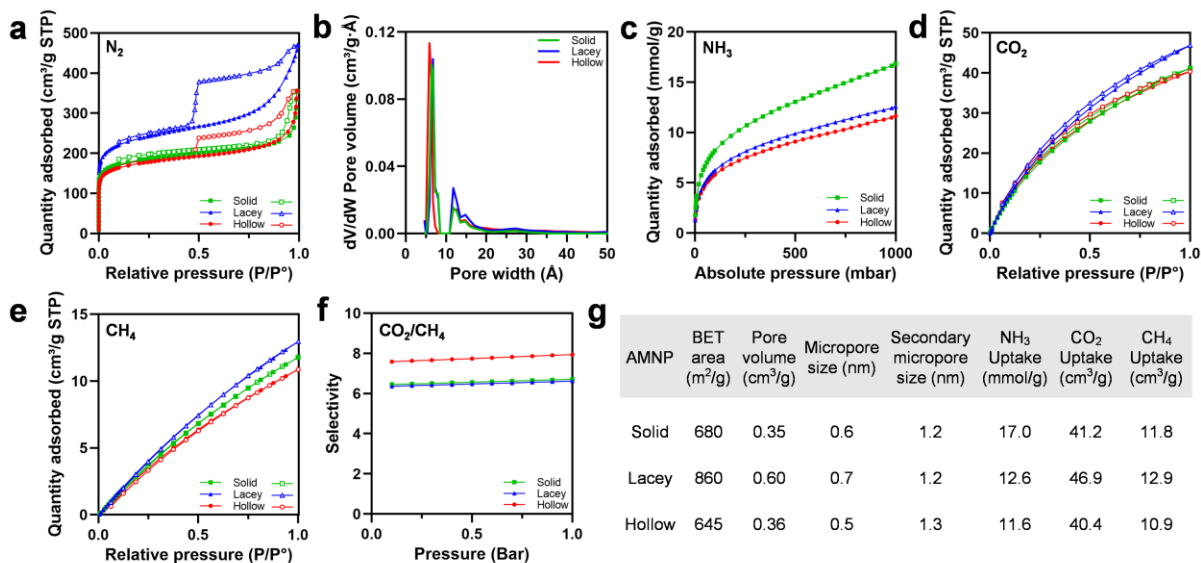
Figure 3.25 Sorption measurements for Solid (S-AMNP), Lacey (L-AMNP) and Hollow (H-AMNP) nanoparticles, and pore size calculations. For sorption measurements, closed markers represent adsorption and open markers represent desorption. (a) Nitrogen isotherms. (b) Pore volume measurements. (c) NH_3 uptake. (d) CO_2 uptake. (e) CH_4 uptake. (f) IAST calculation for a mixture of mole fractions 0.05 CO_2 and 0.95 CH_4. (g) Summarized sorption measurements and pore sizes for AMNPs.

AMNP	BET area (m²/g)	Pore volume (cm³/g)	Micropore size (nm)	Secondary micropore size (nm)	NH_3 Uptake (mmol/g)	CO_2 Uptake (cm³/g)	CH_4 Uptake (cm³/g)
Solid	680	0.35	0.6	1.2	17.0	41.2	11.8
Lacey	860	0.60	0.7	1.2	12.6	46.9	12.9
Hollow	645	0.36	0.5	1.3	11.6	40.4	10.9

Despite it having a lower surface area, this higher density could have facilitated NH_3 adsorption. These porous materials have comparable performance in total uptake at 1 bar to metal-organic frameworks[114-117] and porous organic polymers.[118, 119]

To probe the efficacy of AMNPs for gas storage and separation applications, CO_2 and CH_4 isotherms were collected at 298 K (Figure 3.25d,e). Total CO_2 uptake is similar to that seen in microporous organic polymers[120] (S-AMNP= 41.2 cm^3/g, L-AMNP= 46.9 cm^3/g, and H-AMNP= 40.4 cm^3/g), and is higher than observed for CH_4 (S-AMNP= 11.8 cm^3/g, L-AMNP= 12.9 cm^3/g, and H-AMNP= 10.9 cm^3/g). To determine whether AMNPs could be utilized for carbon dioxide separation from natural gas consisting predominantly of methane, we quantified their selectivity through the application of ideal adsorbed solution theory (IAST)[121] on the pure gas isotherms fitted using BET model (Figures 3.26-3.28). Using gas phase mole fractions of 0.05 for CO_2 and 0.95 for CH_4, which is a typical composition for natural gas purification, IAST calculations were performed at 1 bar (consistent with collected measurements) and predicted selectivities ranging from 6–8 were obtained (Figure 3.25f). These selectivities indicated that CO_2
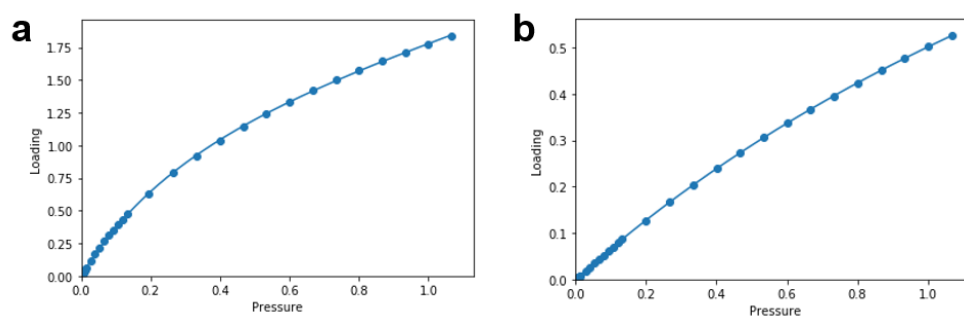
Figure 3.26 Pure-component adsorption isotherms for S-AMNP. Loading (mmol/g) of (a) CO_2 and (b) CH_4 versus pressure (bar) at 298 K. Isotherms were fitted using a BET model with the Python package pyIAST.
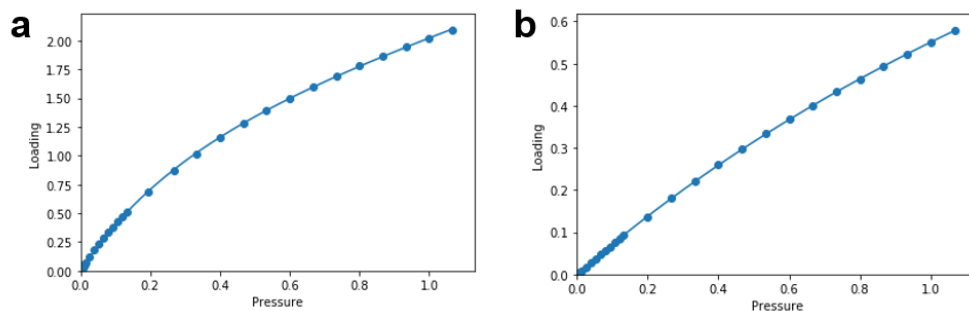
Figure 3.27 Pure-component adsorption isotherms for L-AMNP. Loading (mmol/g) of (a) CO_2 and (b) CH_4 versus pressure (bar) at 298 K. Isotherms were fitted using a BET model with the Python package pyIAST.
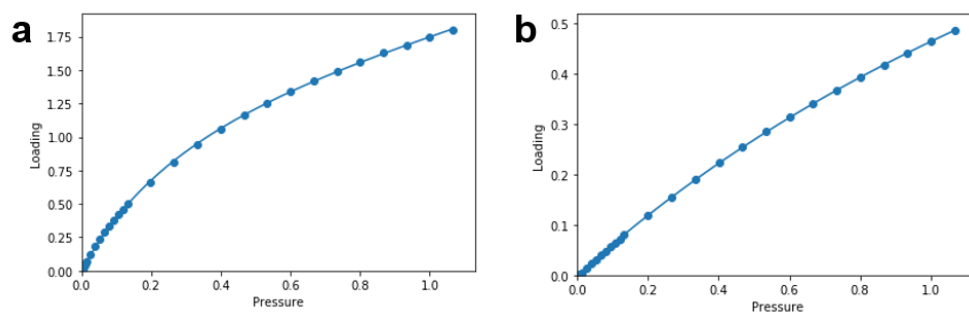
Figure 3.28 Pure-component adsorption isotherms for H-AMNP. Loading (mmol/g) of (a) CO_2 and (b) CH_4 versus pressure (bar) at 298 K. Isotherms were fitted using a BET model with the Python package pyIAST.

was preferentially adsorbed over CH_4. The stronger interactions between AMNPs and CO_2 were attributed to the presence of hydroxyl moieties present on the surface.[122, 123] Despite L-AMNPs having the highest storage capacity, the selectivity (6.5) was comparable to that of the S-AMNP. H-AMNP had the highest selectivity of around 7.5, perhaps arising to the higher density of functional groups present on the surface per unit volume, as indicated by the lower pore volume of 0.36 cm^3/g. Beyond preferential adsorption due to surface functionalization, the microporous nature of these particles may have aided in increased uptake of CO_2, which has a smaller kinetic diameter of 3.3 Å compared to that of CH_4 (3.8 Å). AMNP selectivities were on the order of those of ZIF-8,[124] glucose-derived porous carbon spheres,[125] and close to those of mixed-ligand metal-

organic frameworks.[126] Therefore, we predict that these particles could be useful for CO_2 separation from natural gas. The total uptake for CO_2 and CH_4 followed surface area trends, indicating that the total loadings of these molecules were less impacted by intermolecular interactions than for NH_3. The combined sorption measurements are compared in Figure 3.25g.

3.2.5 Toxin Adsorption Measurements in Solution

Given the high porosity of AMNPs and success with ammonia capture, we next tested whether they could serve as toxin remediation agents upon exposure to diazinon and paraoxon, which are common pesticides and are used as analogues for structurally similar chemical warfare agents.[55, 127] A known mass of AMNP (10, 20, or 40 µg ± 1 µg) was incubated with either diazinon or paraoxon for 2 h after which the solution was filtered using a 0.2 µm PTFE syringe filter. Analysis of the target remaining in the sample was performed by HPLC and the resulting data was fit using the Langmuir isotherm to generate the saturation loading for the materials in grams/gram and an affinity coefficient (1/M) (Figure 3.29). Binding data suggests that L-AMNP (41.4 g/g) are
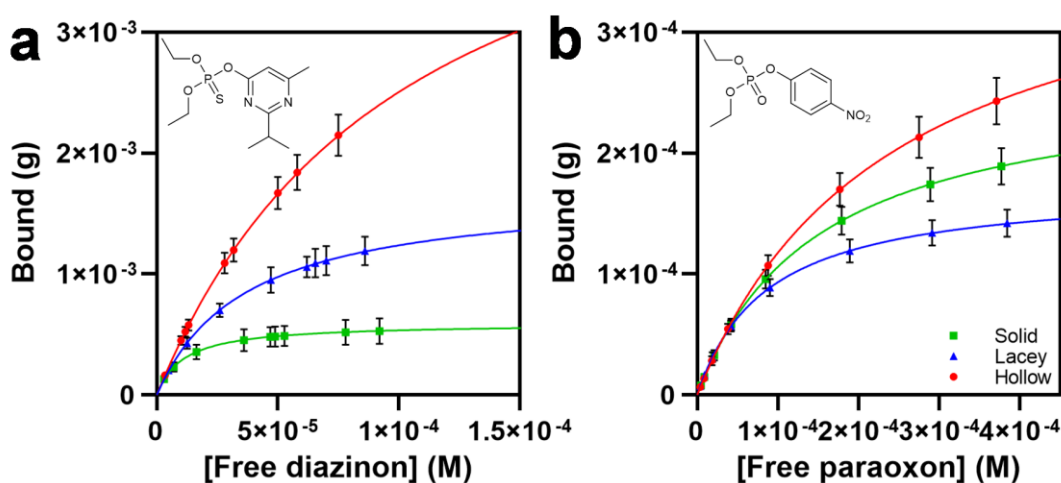
Figure 3.29 Binding of diazinon and paraoxon by Solid (S-AMNP), Lacey (L-AMNP) and Hollow (H-AMNP) nanoparticles. (a) Diazinon adsorption. (b) Paraoxon adsorption. Error bars represent the standard deviation based on three replicate measures.

more efficient at binding diazinon than S-AMNP (14.5 g/g), but not paraoxon (L-AMNP 4.2 g/g, and S-AMNP 6.5 g/g). Surprisingly, despite H-AMNPs having similar surface areas to S-AMNPs, they are capable of binding both diazinon (124 g/g) and paraoxon (9.8 g/g) better than S- or L-AMNPs. This suggests that surface area is not the only parameter important for diazinon binding, which corroborates the higher affinity for diazinon seen in S-AMNP (91,305 M^{-1} *vs* 27,310 M^{-1} for L-AMNP, and 9,739 M^{-1} for H-AMNP). However, surface area trends are consistent with paraoxon affinities (4,162 M^{-1} for H-AMNP, 6,698 M^{-1} for S-AMNP, and 11,658 M^{-1} for L-AMNP). Results from these studies can be found summarized in Table 3.4. The performance of these materials in on par with that of porous organosilicates.[128]

Table 3.4 Saturation loading and affinity of S-,L-, and H-AMNP for diazinon and paraoxon.

AMNP	Diazinon		Paraoxon	
	Saturation loading (g/g)	Affinity (M^{-1})	Saturation loading (g/g)	Affinity (M^{-1})
S-AMNP	14.5	91,305	6.5	6,698
L-AMNP	41.4	27,310	4.2	11,658
H-AMNP	124	9,739	9.8	4,162

3.2.6 Toxin Adsorption on Nylon-Cotton (NYCO) AMNP-Coated Fabrics

We next applied AMNPs to nylon-cotton (NYCO) fabric, and tested their ability to withstand breakthrough following dimethyl methylphosphonate (DMMP) exposure. DMMP is an analogue of sarin gas, and a common simulant for phosphorous containing nerve agents and for permeation studies due to its stability in the gas phase at room temperature.[55] Despite the fact that production and stockpiling of sarin and similar nerve agents have been outlawed, they remain in use as chemical warfare agents.[129, 130] Antidotes are available but they must be administered very quickly after exposure and may not be widely accessible. Clothing with the ability to slow and/or

impede the permeation of nerve agents may provide sufficiently increased protection and/or time necessary to obtain antidotes and treatment. To this end, NYCO swatches (2.5 cm^2) were coated (dyed) by immersion in a suspension of AMNPs (4 mg/mL) or a 1,8-DHN monomer solution (4 mg/mL), stirred at 45 °C for 15 hours, and then washed and dried thoroughly. AMNP-coated fabric swatches (S-AMNP-NYCO, L-AMNP-NYCO, or H-AMNP-NYCO for S-AMNP, L-AMNP, and H-AMNP, respectively) were imaged *via* SEM to illustrate the distribution of material along the fibers, with individual nanoparticles visible for each sample, in comparison to 1,8-DHN-coated (DHN-NYCO) and uncoated (CTRL-NYCO) controls (Figure 3.30 and Figure 3.31).
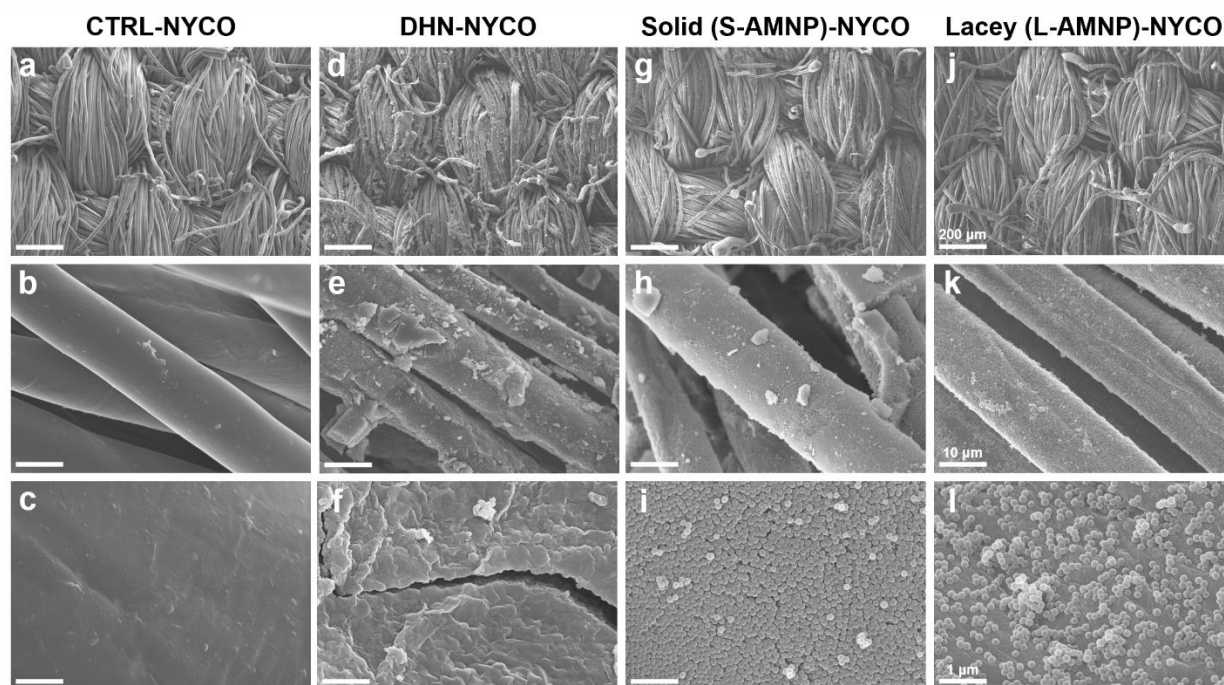
Figure 3.30 SEM images of NYCO fabric swatches at three different magnifications- 100X low mag (top row, scale bars 200 μm), 2,000X (middle row, scale bars 10 μm), and 20,000X (bottom row, scale bars 1 μm). (a-c) Uncoated NYCO control (CTRL-NYCO). (d-f) DHN monomer-based coated NYCO (DHN-NYCO). (g-i) Solid (S-AMNP) coated NYCO (S-AMNP-NYCO). (j-l) Lacey (L-AMNP) coated NYCO (L-AMNP-NYCO).

Fabric swatches were then tested for permeability to DMMP using a stainless-steel aerosol-vapor-liquid-assessment group (AVLAG) cell which holds the sample horizontally with O-ring

seals, supported with solid disks. Liquid droplets of DMMP were applied to the top of the fabric using a repeating dispenser and a flame ionization detector (FID) continuously monitored DMMP concentration on the bottom of the fabric over 16 hours. Typically, the threshold used for initial target breakthrough is based on the military exposure guideline (MEG) of 1 h of marginal exposure level in air. A "marginal" hazard level is defined as causing degraded mission capability or unit readiness. This is based on the proportion of the unit likely to exhibit effects, the nature of those effects, and confidence in the available data. The 1 h marginal air exposure limit for DMMP is 500 mg/m^3.[131] None of the materials evaluated permitted target breakthrough at this rate (Figure 3.31e). To provide a point of comparison, 5.0 mg/m^3 was used as the threshold value for DMMP analysis. The peak DMMP rate through CTRL-NYCO was 7.5 g/m^2/h with initial breakthrough at <1 min and 1,030 μg recovered over the 1,000 min experiment duration.

Fabric sample	Initial breakthrough (min)	Peak rate (g/m²/h)	Total (µg) over 1,000 min	Water vapor transport rate (g/h/m²)
NYCO control	<1.0	7.45	1,030	123 ± 4
DHN monomer	<1.0	10.90	1,027	68 ± 3
S-AMNP	25.2	10.02	981	104 ± 3
L-AMNP	--	0.53	124	103 ± 5
H-AMNP	--	0.50	160	116 ± 9
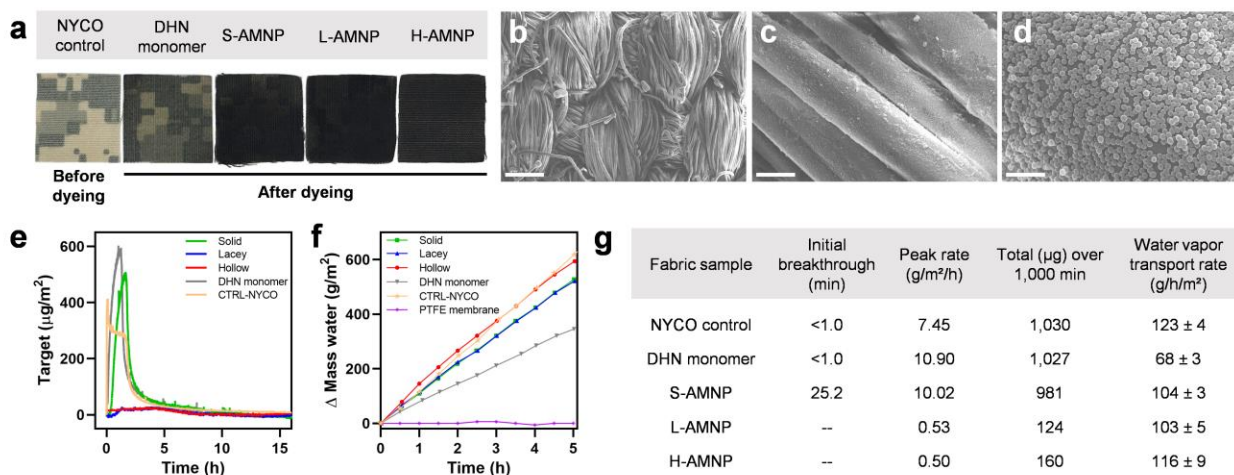
Figure 3.31 AMNP-coated nylon-cotton (NYCO) fabric toxin permeation studies. (a) Photographs of 2.5 cm^2 NYCO swatches before and after coating with AMNPs or 1,8-DHN monomer. (b-d) SEM images of H-AMNP-NYCO. Scale bars: (b) 200 μm, (c) 10 μm, (d) 1 μm. (e) Time-dependent FID response of dimethyl methylphosphonate (DMMP) permeating through NYCO coated and uncoated fabric swatches. (f) Water vapor transport across NYCO coated and uncoated fabric swatches *vs* polytetrafluoroethylene (PTFE) control membrane. (g) Breakthrough times, rates, and total masses for DMMP exposure, and water vapor transport rates across NYCO fabrics.

DHN-NYCO swatches had no impact on initial breakthrough (<1.0 min) but resulted in a higher peak transport rate of 10.9 $g/m^2/h$, with a similar final recovery of 1,027 μg. S-AMNP-NYCO delayed DMMP breakthrough to 25.2 minutes and resulted in a recovery of 981 μg with a peak rate of 10.02 $g/m^2/h$. Both L-AMNP-NYCO and H-AMNP-NYCO had significantly improved performance over S-AMNP-NYCO, DHN-NYCO, and CTRL-NYCO. DMMP permeation through L-AMNP-NYCO and H-AMNP-NYCO remained below the 5.0 mg/m^3 peak rate threshold, and their peak rates were low, at 0.53 and 0.50 $g/m^2/h$, respectively. The total transport was 124 μg for L-AMNP-NYCO and 160 μg for H-AMNP-NYCO; an order of magnitude lower than CTRL-NYCO and DHN-NYCO controls. Although other fabric coatings exist that have exceptional DMMP resistance, they are not always practical. StedCarb, for example, exhibits complete resistance to DMMP, however, the material also impedes permeation of water vapor, a proxy for breathability in fabrics.[132] Fabrics which do not permit water vapor transport are uncomfortable for the wearer and suitable for short duration use only. We sought to examine all NYCO fabric swatches to see if they exhibited efficient water vapor transport, comparing these values to that of a polytetrafluoroethylene (PTFE) membrane control which is highly fluorinated and non-permeable to water vapor (Figure 3.31f). All AMNP-NYCO and CTRL-NYCO showed similar water vapor transport, indicating that the coatings should have little impact on comfort, and the PTFE performed as expected, with essentially zero transport of water vapor. Interestingly, DHN-NYCO, which performed poorly in the DMMP breakthrough study, was less permeable to water vapor than AMNP-NYCO or CTRL-NYCO, although still much more permeable than PTFE. These results are promising for the application of AMNPs as active dyes for uniforms or other fabrics where the wearer is in need of additional protection (Figure 3.31g). The black color of the

dyes may additionally be useful for certain applications, and for others, they can potentially be used to coat inner layers of multi-layer, composite fabrics.

3.2.7 Porosity and Toxin Adsorption of Fungal Melanin Microstructures

Returning to the original inspiration from naturally melanized systems, we sought a natural analogue of our system to determine if there were any similarities or promising attributes. One such possibility is that of the melanized hollow shell created by the etching of fungal cells that constitutively synthesize DHN melanin. These structures are known as melanin ghosts and have a more complex chemical makeup compared to our solely DHN-derived synthetic systems, containing a mixture of 1,8-DHN and related compounds.[133, 134] These structures were imaged using SEM and TEM, followed by porosity measurements (Figure 3.32).
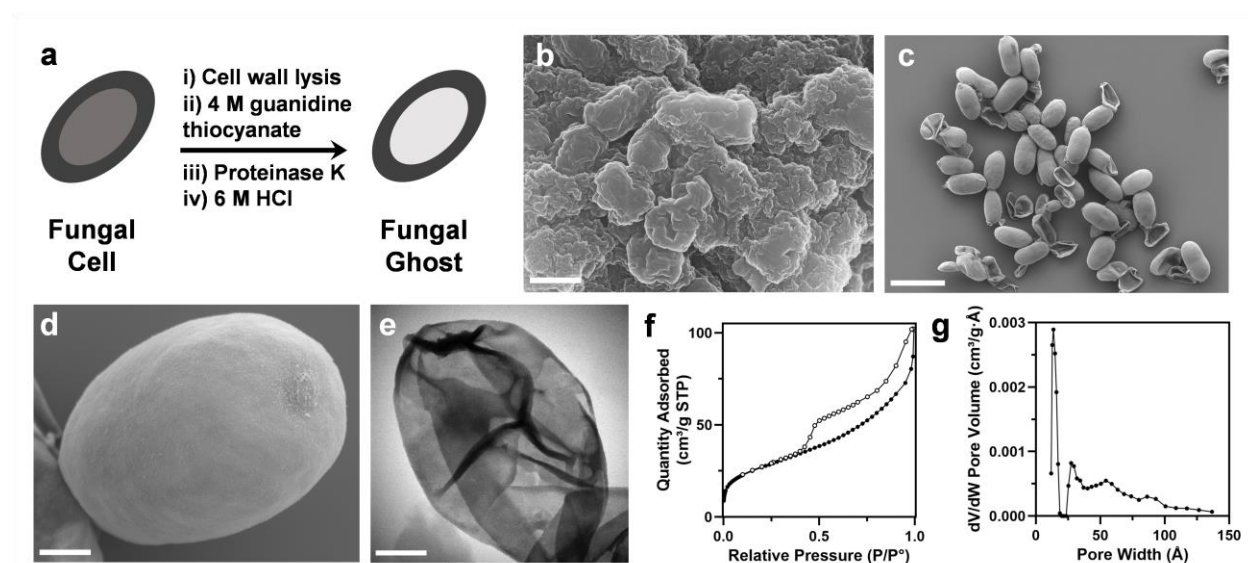
Figure 3.32 Melanized fungal cell ghost synthesis and characterization. (a) Schematic of the melanin ghost formation process. (b) SEM image of aggregates precipitated in HCl from cell culture supernatant (scale bar 500 nm). (c) SEM image of ghosts after critical point drying (scale bar 10 μm). (d) Zoom-in SEM image of ghost after critical point drying (scale bar 1 μm). (e) STEM image of ghost (scale bar 1 μm). (f) N_2 isotherm of ghosts, which yields a BET area of 95 m^2/g. Closed markers represent adsorption and open markers represent desorption. (g) Ghost pore size distribution, with an average micropore size of 13.5 Å.

To make the fungal ghosts, fungal cell walls were enzymatically lysed, followed by treatment with guanidine thiocyanate, proteinase-K, and then 6 M HCl (Figure 3.32a). They were washed in water to afford the hollow ghost structures. The cell culture supernatant was precipitated in 0.6 M HCl to afford melanin aggregates, imaged *via* SEM (Figure 3.32b). These particles were found to be relatively nonporous, with a BET area of 15 m^2/g. Melanin ghosts were also imaged *via* SEM (Figure 3.32c,d) and STEM (Figure 3.32e). SEM samples were prepared by fixation, dehydration in ethanol, and critical point drying in CO_2 in order to preserve the solvated structure. Nitrogen isotherms indicate the ghosts have a non-negligible surface area of 95 m^2/g (Figure 3.32f) with an average micropore pore size of 13.5 Å (Figure 3.32g). The fungal ghosts provided binding capacity larger than S-AMNP and L-AMNP for both paraoxon and diazinon, but less than that of H-AMNP. The binding affinities were within the ranges noted for AMNPs (Figure 3.33).
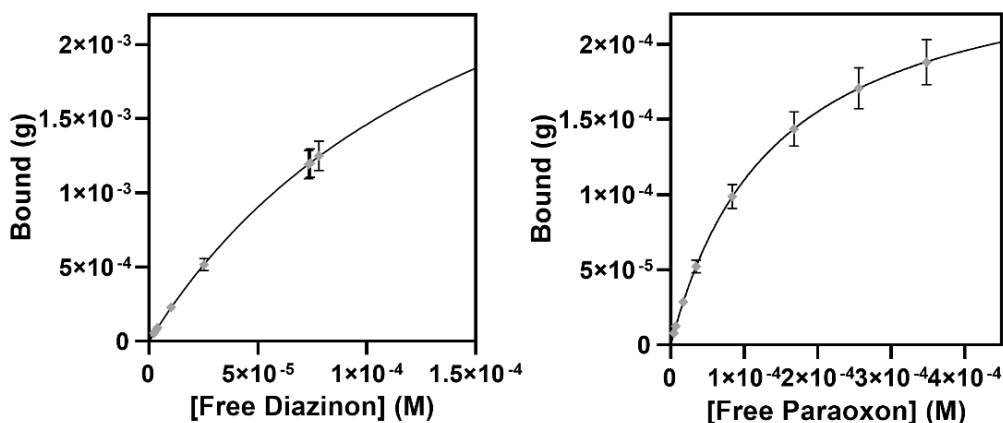
Figure 33. Toxin adsorption of fungal melanin ghosts. (a) Diazinon. (b) Paraoxon.

Since this melanin is assembled within the fungal cell wall, it is possible that cellular components (poly-carbohydrates such as chitin and glucan) may fill in or block pores, interfering with accurate measurement of the contribution of melanin to the porosity. Due to the heterogeneous nature of

the fungal melanin, it is not possible to say what the contribution of allomelanin itself is to the observed porosity. Regardless, these results beg the question whether melanized organisms in nature might have high porosities, dependent on the abundance of certain chemical precursors. This is evidence that, while not as porous as the pure synthetic allomelanin analogues, there is promise for the discovery of other biopolymers of intrinsic microporosity (BioPIMs) in nature.

3.3 Discussion and Conclusion

We found that the initially formed allomelanin nanoparticles, assembled from low molecular weight oligomers, undergo further oxidation and chemical crosslinking on a timescale that allows for partial dissolution resulting in tunable morphology and porosity. The formation of these types of structures has a distant analogue in nature, where process of melanosomal maturation seen in some bird species. In those animals, solid melanosomes are formed, followed by a biochemical "etching" of the core to afford hollow structures, wherein a pheomelanin@eumelanin core-shell structure exploits chemical differences in the bulk and particle surface for the selective etching process.[39] Granted, that is a eumelanin-based process, and requires sophisticated biological mechanisms, but it does beg the question of what kind of role similar processes might play in yet discovered fungal or other melanin containing systems. In addition, hollow melanized structures can be made biosynthetically by etching melanized bacterial or fungal cells to afford hollow structures called melanin ghosts, albeit on a different length scale.[135] Here, we show that the synthesis of these porous AMNP structures is facile, template-free, and requires few starting materials, all of which are commercially available with the principle component, 1,8-DHN, being naturally occurring. In addition, the synthesis can easily be adjusted

with a simple MeOH treatment to enable tunable morphology and increased porosity, while retaining high uniformity.

The initially observed solvent instability and visible color change over time in AMNPs allowed us to consider the possibility of chemical tunability. A solvent screen and timeseries of MeOH treatment revealed a structure that when first synthesized contains a loosely associated core of oligomers which are disrupted by organic solvent and can leach out of the particle through micropores and be redeposited onto the surface over several days. This is consistent with a general increase in size from S- to L- to H-AMNP, as revealed by STEM, AFM, and SAXS analyses. To clarify whether there was a conservation of material between AMNPs, the total particle intensity was normalized by area. Irrespective of their morphology, each AMNP contains approximately the same amount of material. This is consistent with the mechanism of formation of L- and H-AMNPs leaching oligomers from their cores and redepositing them onto the particle surface, growing the outer diameters of the particles using material leached from the core. In addition, the high uniformity of the three AMNPs enabled 3D modeling from well-formed SAXS scattering curves, often reserved for highly ordered, crystalline systems.

BET measurements revealed AMNPs have high surface areas with tunable micropores capable of adsorbing N_2, CH_4, and CO_2. The functionalized surface of these materials also proved to be advantageous for ammonia capture, with results on par or surpassing capabilities of highly ordered, crystalline structures such as MOFs.[114-117] AMNPs were also capable of adsorbing the toxin simulants diazinon and paraoxon in solution and were highly efficient at preventing the permeation of DMMP across AMNP-coated NYCO fabric while allowing the transport of water vapor. This breathable yet absorbent material could be generated in a straightforward manner with

a simple deposition method from materials that are stable at room temperature in water for at least 18 months prior to use.

This work demonstrates how simple materials generated from biologically relevant building blocks may provide a route to scalable, biocompatible materials for applications such as toxin remediation and gas storage. In addition, it proposes the intriguing possibility that such porosity exists for natural melanins or other materials and are yet to be discovered. We also showed that natural allomelanin-containing hollow structures (fungal ghosts) have non-negligible porosity with the capability to adsorb diazinon and paraoxon toxins, and that in the future, other porous melanins might be discovered. These results demonstrate how materials generated from biological building blocks may provide a route to scalable, biocompatible materials for applications such as toxin remediation and gas storage. These results beg the question whether allomelanin-containing organisms in nature might utilize this high porosity to their evolutionary advantage. Indeed, some melanins are known to be toxin adsorbents in organisms, yet they are not known to have high surface areas, and have not been described in terms of their microporosity, although some suggestion of this has been evidenced by NMR cryoporometry studies probing fungal eumelanin ghosts.[91] However, chemical changes in the melanin monomer have been shown to induce structural changes on the nano- and micro-scale,[136, 137] so the correlations are not necessarily straightforward and may vary widely depending on the composition of the melanin. In fact, fungal melanin is not known to exist in a pure state in the cell wall, rather, incorporated with other cell wall components such as polysaccharides and chitin, and the amount of DHN in allomelanin-containing fungal cells has yet to be quantified.[37, 38] Future work will aim to quantify the melanin composition and attempt to manipulate the biochemistry of these organisms to clearly elucidate

the contributions of DHN to the overall structure and function. Synthesis provides a facile approach to access and probe the performance of pure DHN-melanin devoid of confounding biological structures/molecules from the natural system, with the understanding that these additional materials may provide essential functions. Moreover, this synthetic allomelanin may inspire further investigation of microporosity of this type in natural biopolymers originating with fungi and extending to other organisms. Finally, in synthetic systems, this kind of bioinspired approach to porous materials could complement the sophisticated designed materials that have become of increasing interest in the form of metal–organic frameworks (MOFs),[138, 139] covalent organic frameworks (COFs),[140, 141] and mixed matrix membranes.[142,143]

3.4 Experimental Details

Reagents. 1,8-Dihydroxynaphthalene (1,8-DHN) (95+%) was purchased from Matrix Scientific. Ethanol (200 proof) was purchased from Sigma-Aldrich. Sodium periodate ($NaIO_4$) (99.8%), HPLC-grade acetonitrile (ACN) ($\geq$99.99%), methanol (MeOH) ($\geq$99.8%), ethyl acetate (EtOAc) ($\geq$99.5%), dichloromethane (DCM) (99.6%), acetone ($\geq$99.5%), *N,N*-dimethylformamide (DMF) (99.5%), 1-octanol (99%), acetic acid ($\geq$99.7% w/w), 2-propanol (IPA) ($\geq$99.5%), and all other chemical reagents were purchased from Fisher Scientific unless otherwise noted. All chemicals were used as received except for 1,8-DHN, which was re-dissolved in 200 proof ethanol, filtered, and vacuum dried prior to use. Milli-Q water was used in all experiments, purified using a Branstead GenPure xCAD Plus system from ThermoFisher Scientific. Transmission electron microscopy (TEM) grids were purchased from Electron Microscopy Sciences.

Instrumentation. UV-Vis spectra were recorded using an Agilent Cary 100 UV-Vis spectrophotometer. Scanning transmission electron microscopy (STEM) images were acquired on

a Hitachi HD2300 or JEOL 200 ARM at an accelerating voltage of 200 kV. Transmission electron microscopy (TEM) images were obtained on a JEOL 1230 TEM. TEM/STEM grids were surface plasma treated using a PELCO easiGlow glow discharge cleaning system prior to use. Scanning electron microscopy (SEM) images were acquired on a Hitachi SU8030 at an accelerating voltage of 10 kV and an emission current of 15 μA. AFM images were acquired on a Bruker Icon using peak force QNM, and ScanAsyst A cantilevers. Analytical high-performance liquid chromatography (HPLC) analysis for the AMNP aging study was performed on a Jupiter 4u Proteo 90A Phenomenex column (150×4.60 mm) using a Hitachi-Elite LaChrom L-2130 pump equipped with UV-Vis detector (Hitachi-Elite LaChrom L-2420). Zeta potential was measured on a Zetasizer. Multi-angle static and dynamic light scattering (SLS, and DLS, respectively) measurements were performed on an ALV/CGS-3 four-angle, compact goniometer system. Samples were activated using a tousimis SAMDRI-PVT-3D Advanced Manual Critical Point Dryer and a Micromeritics Smart VacPrep. Sorption measurements were taken on a Micromeritics ASAP 2020 and a Micromeritics 3Flex Physisorption instrument. Diazinon and paraoxon toxin adsorption was analyzed by HPLC using a Shimadzu HPLC system. Dimethyl methylphosphonate (DMMP) permeation studies were performed using a stainless-steel aerosol-vapor-liquid-assessment group (AVLAG) cell, with detection *via* a flame ionization detector (FID).

SEM sample preparation. AMNPs were dropcasted onto a silicon wafer, air dried, and coated with 10 nm osmium before imaging with a Hitachi SU 8030 SEM operating at an accelerating voltage of 10 kV and an emission current of 15 μA.

AFM sample preparation. Samples were prepared by depositing 20 to 40 μL of AMNP in Milli-Q water onto 1 cm^2 freshly cleaved mica, letting it sit for 1 minute, and then blotting dry.

Embedding of H-AMNPs in resin for STEM imaging. AMNPs were pelletized in an Eppendorf tube. Dehydration occurred with a graded series of ethanol and acetone prior to infiltration with EMBed812 epoxy resin and the resin polymerized at 60 °C for 48 hours prior to ultramicrotomy using a Leica EM UC7 Ultramicrotome to obtain ultra-thin sections (80 nm). Micrographs were obtained on a Hitachi HD2300 STEM operating at 200 kV.

3.4.1 Synthesis of Solid (S-AMNP), Lacey (L-AMNP) and Hollow (H-AMNP) Porous Allomelanin Nanoparticles

Solid (S-AMNPs) were synthesized in much the same manner as AMNP-1 in previous work.[107] Briefly, 1,8-DHN (150 mg) was dissolved in 7.5 mL acetonitrile in a round bottom flask. To this solution, 142.5 mL Milli-Q water was added, and the mixture was stirred for 5 minutes before quickly injecting 1 mL of 1N sodium periodate solution. The reaction quickly turned yellow and then gray upon injection of the oxidant. The reaction was stirred for 20 hours and then purified by centrifugation at 11,500 rpm for 10 minutes, with three cycles of washing by redispersion in Milli-Q water. After the final wash, the particles were re-suspended in 12 mL of Milli-Q water in a 50 mL Falcon tube, and stored at room temperature, capped, and under ambient conditions. Samples were stored in Milli-Q water at room temperature. The concentration (mg/mL) was determined by lyophilizing a known volume of S-AMNP suspension in a pre-weighed vial.

Hollow (H-AMNPs) were synthesized from a fresh batch of purified S-AMNPs. S-AMNPs were stored in Milli-Q water, under ambient conditions, in a capped, plastic tube for 24 hours after synthesis. At this 24 hour mark, they were pelletized by centrifugation at 11,500 rpm for 12 minutes. The water was removed and replaced with MeOH to a final concentration of 0.5 mg/mL. The pellet was vortexed until full mixing was achieved (approximately 30 seconds), and

the solution/suspension was then placed onto a horizontal shaker at 90 rpm for 6 days. This mixture was then dialyzed into Milli-Q water using 10k molecular weight cutoff snakeskin dialysis tubing (Thermo Scientific), with the water changed 3 times over 2 days. If necessary, the particles were then re-concentrated to the desired amount by centrifuging at 11,500 rpm for 12 minutes and removing excess water.

Lacey (L-AMNPs) were synthesized from a fresh batch of purified S-AMNPs. S-AMNPs were stored in Milli-Q water, under ambient conditions, in a capped, plastic tube for 48 hours after synthesis. At this 48 hour mark, they were pelletized by centrifugation at 11,500 rpm for 12 minutes. The water was removed and replaced with MeOH to a final concentration of 0.5 mg/mL. The pellet was vortexed until full mixing was achieved (approximately 30 seconds), and the solution/suspension was then placed onto a horizontal shaker at 90 rpm for 6 days. This mixture was then dialyzed into Milli-Q water using 10k molecular weight cutoff snakeskin dialysis tubing, with the water changed 3 times over 2 days. If necessary, the particles were then re-concentrated to the desired amount by centrifuging at 11,500 rpm for 12 minutes and removing excess water.

3.4.2 Electron Microscopy and Image Analysis

Scanning Electron Microscopy (SEM). SEM images were acquired on a Hitachi SU8030 at an accelerating voltage of 10 kV and an emission current of 15 µA. AMNPs were dropcasted onto a silicon wafer, air dried, and coated with 10 nm osmium before imaging with a Hitachi SU 8030 SEM operating at an accelerating voltage of 10 kV and an emission current of 15 µA.

Scanning Transmission Electron Microscopy (STEM). STEM images were acquired on a Hitachi HD2300 or JEOL 200 ARM at an accelerating voltage of 200 kV. Samples imaged on the Hitachi instrument were prepared on 200 mesh copper TEM grids with formvar on carbon

support. Samples imaged on the JEOL 200 ARM instrument were prepared on 200 mesh copper TEM grids with lacey carbon support layer. In both cases, grids were first plasma treated using a PELCO easiGlow glow discharge cleaning system, and 2 µL of AMNP suspension was dropcasted and left to dry before imaging.

For resin-embedded particles, AMNPs were pelletized in an Eppendorf tube. Dehydration occurred with a graded series of ethanol and acetone prior to infiltration with EMBed812 epoxy resin and the resin polymerized at 60 °C for 48 hours prior to ultramicrotomy using a Leica EM UC7 Ultramicrotome to obtain ultra-thin sections (80 nm). Micrographs were obtained on a Hitachi HD2300 STEM operating at 200 kV.

STEM Size and Density Measurements. Bright-field STEM (BF-STEM) and high-angle annular dark-field STEM (HAADF-STEM) imaging for size and density measurements was performed on a JEOL 200 ARM operating at 200 kV. Images were collected in HAADF-STEM mode with a probe semiconvergence angle of 10 mrad and at a camera length of 20 cm. A beam current of 0.3 nA and pixel dwell times between 1 and 5 µs were used. For the radial average intensity measurements, individual melanin nanoparticles were cropped and a moving average filter of 5 px was applied to remove noise. Next, the radial averaged intensity from the center of the particle to the periphery was measured and normalized. The average and standard deviation of minimum 4 individual nanoparticles of each type were determined. The pixel size is 0.6 nm. For normalized intensity measurements, the total intensity from the masked data was normalized by the area of the given particle.

3.4.3 Light Scattering Analysis

Multi-angle DLS measurements were performed at 0.0001 wt% in Milli-Q water on an ALV/CGS-3 four-angle, compact goniometer system, which consisted of a 22 mW HeNe linear polarized laser operating at a wavelength of λ=632.8 nm and scattering angles from θ= 30–150°. Fluctuations in the scattering intensity were measured *via* an ALV/LSE-5004 multiple tau digital correlator, and analyzed *via* the intensity autocorrelation function ($g^{(2)}(\tau)$). A cumulant analysis was used to fit the data, and the mutual diffusion coefficient was calculated through the relation:

$$\Gamma = q^2 D_m \qquad \text{(Equation 3.1)}$$

where Γ is the average decay rate of the autocorrelation function and q is the scalar magnitude of the scattering vector. The hydrodynamic radius (R_h) was calculated through the Stokes-Einstein equation:

$$D_m \approx D_t = \frac{k_B T}{6\pi\eta_s R_h} \qquad \text{(Equation 3.2)}$$

where D_m is the mutual diffusion coefficient, D_t is the tracer diffusion coefficient, k_B is the Boltzmann constant, T is the absolute temperature, and η_s is the solvent viscosity. Samples were filtered through a 0.45 μm PVDF filter (Millipore) directly into pre-cleaned scattering cells prior to measurement.

The effective radius of gyration (R_g) was obtained from the SLS data through a Berry equation, which relates the inverse scattering intensity as a function of the scattering angle:

$$\left(\frac{Kc}{R_\theta}\right)^{1/2} = \left[\left(\frac{1}{M_w}\right)\left(1 + \frac{q^2 R_g}{3}\right)\right]^{1/2} \qquad \text{(Equation 3.3)}$$

where K is the optical constant and R_θ is the Rayleigh ratio. The assembly M_w can be extracted from the inverse y-intercept, while the R_g can be extracted from the slope of the linear relationship.

The parameter $\rho = \frac{R_g}{R_h}$ is an estimate of the compositional distribution of the particles, where

ρ values of 0.775, 1.0, and > 1 correspond to spherical micelles, vesicles, or elongated structures, respectively.

3.4.4 Small Angle X-Ray Scattering (SAXS) Measurements

Experiments were performed at beamline 5-ID-D of the DuPont-Northwestern-Dow Collaborative Access Team (DND-CAT) Synchrotron Research Center at the Advanced Photon Source (APS), Argonne National Laboratory. AMNPs were prepared at 10 mg/mL in Milli-Q water and during measurements flowed through a 1.5 mm glass capillary at 1 mm/sec for consistent background subtraction. Data was collected with X-Ray energy at 17 keV (λ= 0.73 Å) with samples exposed for 10 frames of 0.2 seconds each. Sample to detector distances were as follows: 201.25 mm for SAXS (small-angle X-Ray scattering), 1014.2 mm for MAXS (mid-angle X-Ray scattering), and 8508.4 mm for WAXS (wide-angle X-Ray scattering). The scattering intensity was recorded in the interval $0.002390 < q < 4.4578$ Å^{-1}. The scattering vector q is defined as:

$$q = \left(\frac{4\pi}{\lambda}\right) sin\left(\frac{\theta}{2}\right) \qquad \text{(Equation 3.4)}$$

where θ is the scattering angle. Azimuthal integration of the SAXS pattern to achieve 1D data was achieved using GSAS-II software (UChicago Argonne, LLC) developed at the APS. Samples were oscillated with a syringe pump during exposure to prevent beam damage. Background scattering patterns were obtained from samples containing Milli-Q water. This background data was then subtracted from experimental data. Modeling of the scattering data with a spherical core-shell geometrical model was conducted in the Irena software package running on IgorPro software.[144]

3.4.5 Dummy Atom Modeling and SAXS Reconstruction

Scattering data were also assessed using *ab initio* dummy atom modeling (DAM) methods using the ATSAS analysis software.[113] Pair distance distribution functions p(r) were calculated from the background subtracted scattering data (0.003 $Å^{-1}$ to 0.029 $Å^{-1}$) for each nanoparticle using the indirect Fourier transform method DATGNOM.[145] The *ab initio* shape determination program DAMMIF was used to conduct ten separately refined models for each nanoparticle containing 10,000 beads each of approximately 40 Å.[146] Similar models were obtained with either an emphasized Porod or logarithmic curve weighting function. The program DAMAVER was used to align the models and select the most probable; creating an average DAM where the occupancies of the atoms are proportional to the probability of the atom existing in all models.[147] The normalized dummy atom occupancy for each averaged DAM was used to calculate a weighted R_g for each averaged DAM as well as shell to core bead probability ratios. The program SASRES was used to apply a Fourier shell correlation approach as an estimate of DAM resolution.

3.4.6 Gas Sorption Measurements

AMNPs, stored in Milli-Q water, were centrifuged at 11,500 rpm for 12 minutes, and the water was removed and replaced with EtOH. This process was repeated twice more with addition of fresh EtOH each time to ensure effective removal of water. Samples were activated using a tousimis SAMDRI-PVT-3D Advanced Manual Critical Point Dryer. Using the supercritical dryer, particles were added to the sample chamber, cooled to 0–10°C, and pressurized to 800 psi. Ethanol was exchanged with liquid CO_2 over a 10 hour period, purging the system for five minutes every two hours. After the fifth purge, the temperature was raised to 40 °C and the system was pressurized to 1200–1400 psi to obtain supercritical CO_2. Pressure was released slowly overnight

at a rate of 0.5 cc/min. Samples were immediately transferred onto a Micromeritics Smart VacPrep and were placed under vacuum for two hours at 25 °C prior to sorption measurements. Nitrogen physisorption measurements were collected using a Micromeritics ASAP 2020 instrument at 77 K. Pore-size distributions were obtained using DFT calculations with a carbon slit geometry and an N_2 DFT model. CO_2 and CH_4 isotherms were measured using a Micromeritics ASAP 2020 instrument at 298 K. NH_3 isotherms were collected using a Micromeritics 3Flex Physisorption instrument at 298 K. Ideal adsorbed solution theory (IAST) calculations and isotherm fittings using a BET model for CO_2/CH_4 were performed using the Python package pyIAST.[121]

3.4.7 Diazinon and Paraoxon Toxin Adsorption Studies in Solution

Solutions of paraoxon and diazinon were prepared in Milli-Q water at concentrations varying from 1 to 100 ppm in 20 mL scintillation vials, and then 10, 20, or 40 μg ($\pm$ 1 μg) of AMNPs were added to the solution. Three replicates were performed for each concentration. The samples were mixed on a rotisserie mixer at room temperature for 2 h, in the dark, and then filtered with 0.2 mm PTFE syringe filters. Analysis of the target remaining in the sample was performed by HPLC. A Shimadzu High Performance Liquid Chromatography (HPLC) system with dual-plunger parallel flow solvent delivery modules (LC-20AD) and an auto-sampler (SIL-20AC; 40 μL injection volume) coupled to a photodiode array detector (SPD-M20A; 277 nm) was used for data collection. The stationary phase was a C18 stainless steel analytical column (Luna, 150 mm x 4.6 mm, 3 μm diameter; Phenomenex, Torrance, CA) with an isocratic 45:55 acetonitrile: 1% aqueous acetic acid mobile phase (1.2 mL/min).[148] The amount of target bound was determined based on the difference between the amount in the sample and the amount in the original target preparation using the same

HPLC method. The resulting data was fit using the Langmuir isotherm to generate the saturation

loading for the materials in gram/gram and an affinity coefficient (1/M) using the equation:

$$q = \frac{m\, q_{sat}\, k\, [free]}{1+k\, [Free]} \qquad\qquad (Equation\ 3.5)$$

where q is the amount bound, m is the mass, q_{sat} is the capacity, and k is the affinity. The

phenomenological Langmuir expression provides a reasonably good fit for the data collected and

has been used previously for determination of parameters related to binding of energetics and

pesticides by porous adsorbent materials.[128, 149-151]

3.4.8 Nylon-Cotton (NYCO) Fabric Studies

Deposition of AMNPs onto NYCO Fabric. Deposition onto NYCO fabric swatches (2.5

cm^2) was developed through optimization of a previously reported protocol.[152] Swatches were

weighed using a microbalance and subsequently washed with Milli-Q water. The fabrics were then

immersed in 8 mL of a 4 mg/mL AMNP suspension in water or into 8 mL of 4 mg/mL monomer

solution in water. The solutions were stirred at 45 °C for 15 hours. The samples were then placed

into centrifuge tubes containing 10 mL water and washed by vortexing the tubes for approximately

30 seconds. The washing process was repeated three times with fresh water. The samples were

then sonicated in 10 mL water for 2 minutes to remove any unbound AMNPs from the fabric, and

the process repeated 6 times. Finally, the samples were dried in an incubator at 40 °C for 30

minutes. Dried fabrics were weighed again and the amount of deposited melanin was calculated.

The amount of material deposited onto each sample was as follows: 12.4 mg (S-AMNP), 12.7 mg

(L-AMNP), 14.0 mg (H-AMNP), and 2.1 mg from the DHN monomer.

DMMP breakthrough studies on AMNP-coated NYCO fabric. The permeation of

dimethyl methylphosphonate (DMMP) through NYCO fabric samples was assessed as described

by Test Operations Procedure (TOP) 8-2-501, Permeation Testing of Materials with Chemical Agents or Simulants (Swatch Testing).[131, 153] An internal, probe driven heater was used to control the temperature within a custom environment. The ratio of humid to dry air entering this chamber was addressed using probe-driven mass flow controllers. The stainless-steel aerosol-vapor-liquid-assessment group (AVLAG) cell held the sample horizontally with O-ring seals. Diffusive permeation testing used a nitrogen stream. The target was placed in the headspace above the fabric swatch, which was stagnant, with no pressure difference above and below the swatch. The sample was supported between two solid support discs with aligned 0.64 cm^2 circular openings. This assembly was then placed in the AVLAG cell, and humidity equilibrated for 2 h. DMMP was introduced as liquid droplets using a repeating dispenser, and the concentration was monitored using a dedicated flame ionization detector (FID).

Water vapor transport studies on AMNP-coated NYCO fabric. The water vapor transport (WVT) rate for the treated fabrics was evaluated using a circular fabric sample with a total exposed area of 1.65 cm^2.[131, 154, 155] The protocol is derived from guidance suggested by ASTM E96, Water Vapor Transport: Upright Open Cup Method to characterize water vapor transport through the fabric samples and uses an incubator modified to provide an enclosure at 25°C. A 20 mL scintillation vial was loaded with 16.9 mL deionized water. The fabric sample was sealed over this vial, and vial was weighed. A desiccant was used to drive a humidity differential in the incubator, with a dry nitrogen stream flowing across the surface of the sample (0.25 L/min). The weight of the vial was measured at 30 to 45 min intervals using an analytical balance.

3.4.9 Fungal Cell Growth and Ghost Formation

Exophiala lecanii-corni were grown in the following manner: A single colony of E. *lecanii-corni* was inoculated into 10 ml YPD liquid medium and shaken at 30 °C at 200 rpm for 48 hours. 1 mL of cell culture was transferred into 100 ml YPD and shaken at 30 °C for 5 days. The cell culture was very dark after 5 days of growth. The next steps involved a days-long process as follows: Day 1: Collect fungal cells. Spin down cells at 5,000 rpm for 10 min. Wash cell pellets with 100 mL PBS. Spin down again. Suspend cells in 10 mL of 1.0 M sorbitol in 0.1 M sodium citrate (pH 5.5, adjusted with 1 M HCl). Add 100 mg cell wall lysing enzyme from *Trichoderma harzianum*. Shake the suspension at 30 °C overnight at 100 rpm. Day 2: Spin down enzyme-treated fungal cells. Wash with 20 mL PBS twice. Suspend pellets in 10 mL 4 M guanidine thiocyanate solution. Shake at 28 °C overnight at 100 rpm. Day 3: Spin down cells. Wash with 20 mL PBS 3 times. Suspend pellets in 10 mL 10 mM Tris-HCl (pH 7.8), 1 mM $CaCl_2$ and 0.5% SDS plus 1 mg/mL proteinase K . Shake at 37 °C overnight at 125 rpm. Day 4: Spin down cells. Wash with 20 mL PBS 3 times. Suspend pellets in 10 mL 6 M HCl in a glass tube. Put the tube in boiling water for 1.5 hours. Wash acid treated cells with 50 mL DI water multiple times until the pH reaches 6. Spin down washed pellets to afford ghosts.

Fungal ghost SEM sample prep and imaging. A suspension of ghosts in water was dropcasted onto a silicon chip and left for 20 minutes in a humid petri dish. The chip was then transferred into a porous foam cup and then into a standard cell culture 24 well plate in a series of treatments and dehydration as follows: water (5 min), 2.5% glutaraldehyde (20 min, 4°C), water (5 min), and then 10 min each into EtOH at 30%, 50%, 70%, 90%, and finally 3x 10 min at 100% EtOH. The foam cup was quickly transferred to a 100% ethanol-filled sample chamber of a

tousimis samdri-795 critical point dryer. Once dried, the sample was immediately coated in 9 nm osmium and then imaged on a JEOL JSM-7900FLV SEM at an accelerating voltage of 3 kV and an emission current of 60 μA.

Chapter 4. Novel Artificial Melanosomes of Diverse Morphologies: Eumelanin Analogues

4.1 Introduction

Melanin in the natural world and in synthetic analogues contains a wide array of chemical identities that vary largely based on the chemistry of the monomer precursors. However, the synthesis of melanin is much more complex beyond a simple oxidative polymerization of monomeric species to form complex polymers of spherical nano- and microparticles. Morphological control of the resulting structures is at times multifaceted, and it is not always straightforward to describe the reasoning behind these differences even between similar organisms. Melanic structures exist in human skin, for example, packaged as asymmetric perinuclear, cap-like structures composed of spherical particles on the order of hundreds of nanometers, but even this can change depending on the genetic makeup of the individual, with some melanosomes larger than others.[156] The diversity of morphologies in nature extends far beyond this, and the most exotic of these structures are found in bird feathers. Birds are most illustrative and representative example of how the morphology of melanin can vary widely between species, even with a seemingly similar phenotypical outcome (for example, structural coloration). Not only does the morphology of their melanosomes change over time during the developmental process, but the end result can provide not only spherical nanoparticles, but such exotic structures as rods and hollow rods, and with differing packing orientations (Figure 4.1).[1, 39, 40] The most obvious example of this function is for structural coloration for sexual selection and social competition.[2] But what if these diverse morphologies were applied to a biological system relevant to humans? Humans don't possess such

high aspect ratio melanosomes, nor do they synthesize or use hollow structures. Nevertheless, we sought to explore the synthesis of hollow, rod-like melanin structures, and to test their biocompatibility in neonatal human epidermal keratinocytes (NHEK).
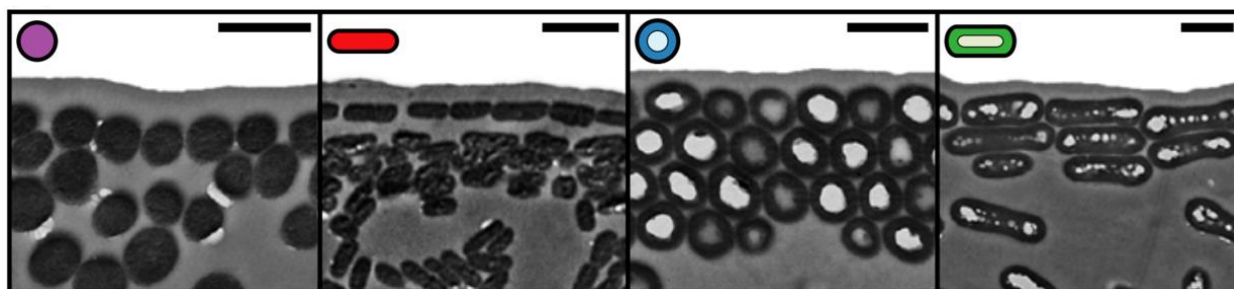
Figure 4.1 Melanosome morphologies observed in African starlings, which lead to an observed iridescence. Scale bars 500 nm. Reproduced with permission, 2013 PNAS.[2]

A ZnO rod-like template was coated with L-DOPA, a precursor in the melanin synthesis pathway found in humans, and subsequently, the L-DOPA was crosslinked to form poly-L-DOPA (P-DOPA). This process also etched out the ZnO rod template, leaving a hollow interior. Through this templation and etching process, we were able to synthesize hollow, long and short aspect ratio melanin nanoparticles. We also synthesized spherical particles from L-DOPA and dopamine (DA) precursors, and compared their biocompatibility with the rod-like particles. The particles were characterized using electron microscopy, scattering, and electrical potential measurements, and their biocompatibility in NHEK was assessed and visualized by confocal microscopy. The particles were internalized by NHEK cells in much the same manner as endogenous melanin, despite their chemical and morphological distinctions, and they were found to be non-toxic. This work paves the way for the use of novel melanin morphologies for human skin protection, cosmetics, and other applications.

4.2 Results and Discussion

4.2.1 Synthesis and Characterization of New Synthetic Analogues of Eumelanin

Melanin mimics (MelNP) were synthesized by oxidative polymerization under ambient oxygen (Figure 4.2). Polydopamine (PDA) particles were synthesized by dissolving 300 mg dopamine HCl with 150 mL of water, stirring vigorously, and then quickly injecting a solution of NaOH to trigger the polymerization. The size of the PDA particles was tuned by the amount of NaOH added, with a larger volume (1.6 mL) resulting in smaller particles, and a smaller volume (1.45 mL) resulting in larger particles. The reaction was stirred overnight and then the particles collected and purified by three centrifugation cycles in water. P-DOPA particles were synthesized in the same manner, but instead of using NaOH, the chemical oxidant $KMnO_4$ was used. 210 mg of L-DOPA was dissolved in 150 mL of water and 0.90 mL of 1 N $KMnO_4$ was quickly injected into the solution and the reaction stirred overnight. For a mixture of PDA/P-DOPA, 500 mg of dopamine hydrochloride and 340 mg of L-DOPA were dissolved in 200 mL of water, and then 2.6 mL of 1 M NaOH was quickly injected into the solution and the reaction stirred overnight.

Synthesis of melanin rod-like structures was more complicated, as it involved a templating and etching process. Both short and long aspect ratio P-DOPA rods were synthesized in the same manner, with the only difference being the starting ZnO template. For the long rods, the template was a ZnO nanowire (50 nm × 300 nm), and for the short rods, the ZnO template was synthesized according to an established protocol (see the experimental details section for more information). To make either of the P-DOPA coated rods, 16 mg L-DOPA was dissolved in 100 mL of water, 17 mg ZnO in 60 mL water was added, the mixture sonicated for 5 minutes, and then stirred vigorously for 20 hours. Over time, the reaction mixture changed from colorless, to light pink, and
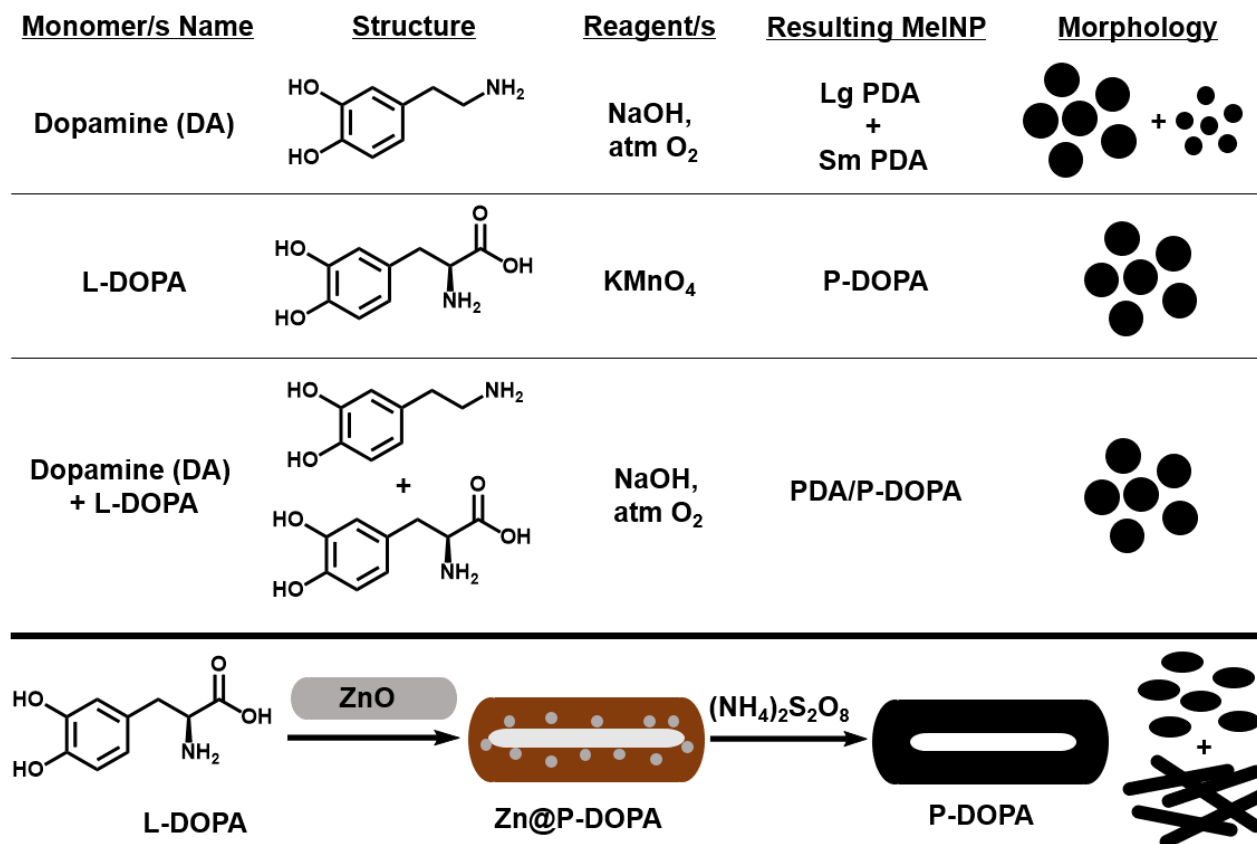
Figure 4.2 Schematic of melanin library synthesis, to form spherical and rod-like structures.

within approximately one hour, a black color formed which continued to darken over several hours. To etch out the ZnO template and further crosslink the particles, they were resuspended in 30 mL of Milli-Q water and stirred overnight with 60 mg of ammonium persulfate. The particles were then washed again in Milli-Q water and dialyzed into Milli-Q water using 10,000 molecular weight cutoff dialysis tubing to remove any residual salt. They were concentrated by centrifugation at 10,000 rpm for 10 minutes to achieved the desired concentration. The melanin library was then characterized by scanning transmission electron microscopy (STEM) and scanning electron microscopy (SEM) (Figure 4.3 and Figure 4.4). These images reveal well-defined particles with low dispersity.
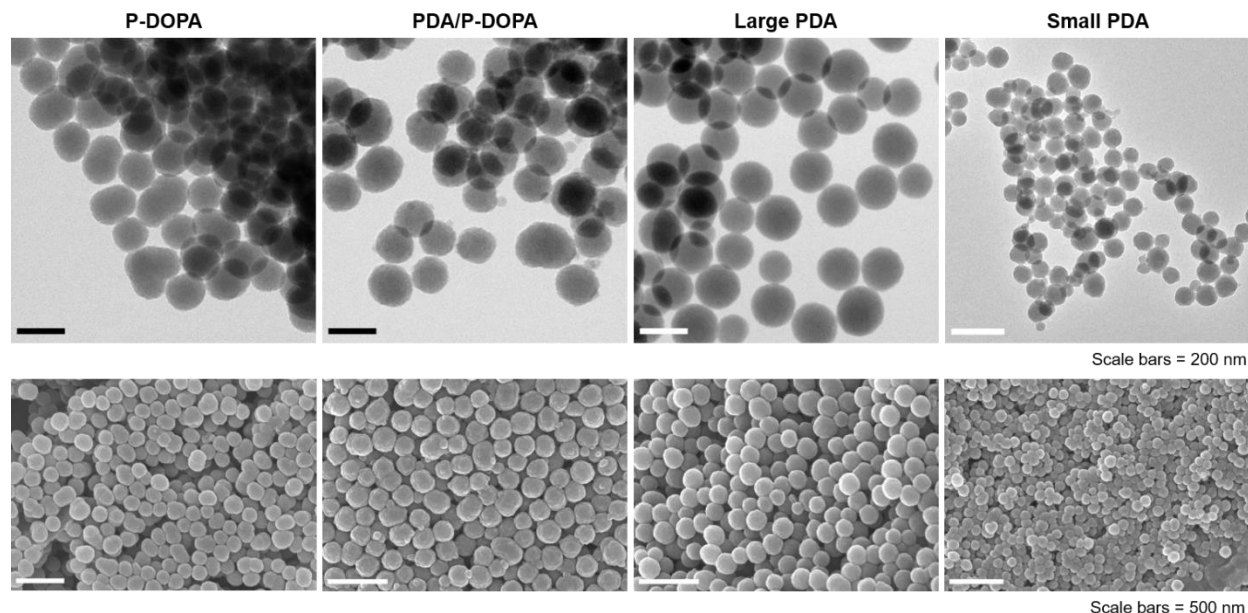
Figure 4.3 Library of eumelanin mimics, characterized by STEM (top row) and SEM (bottom row). From left to right, poly-L-DOPA (P-DOPA), a mixture of 2:1 PDA:P-DOPA, and two different sizes of PDA particles tuned by using less (Large) or more (Small) NaOH in the reaction.
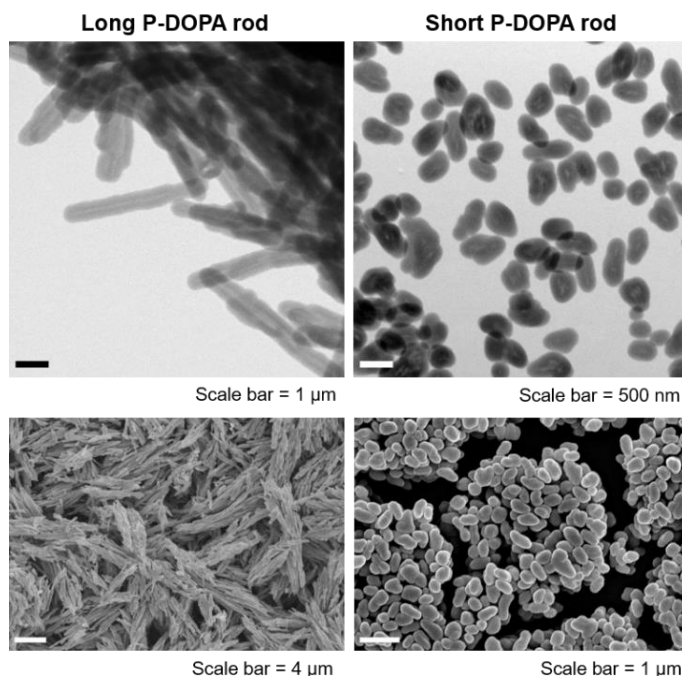
Figure 4.4 Melanin rods of two different aspect ratios, termed long and short P-DOPA rods, characterized by STEM (top row) and SEM (bottom row). Both are synthesized through templation of polymerized L-DOPA (P-DOPA) onto a sacrificial ZnO template which is etched out from the core.

To verify efficiency of the etching process, STEM coupled with energy dispersive spectroscopy (EDS) was performed (Figure 4.5). There is a clear Zn peak in the EDS spectrum prior to the etching process, which disappears after etching. The signals for Al and Cu originate from the TEM grid holder and the copper grid itself, respectively.
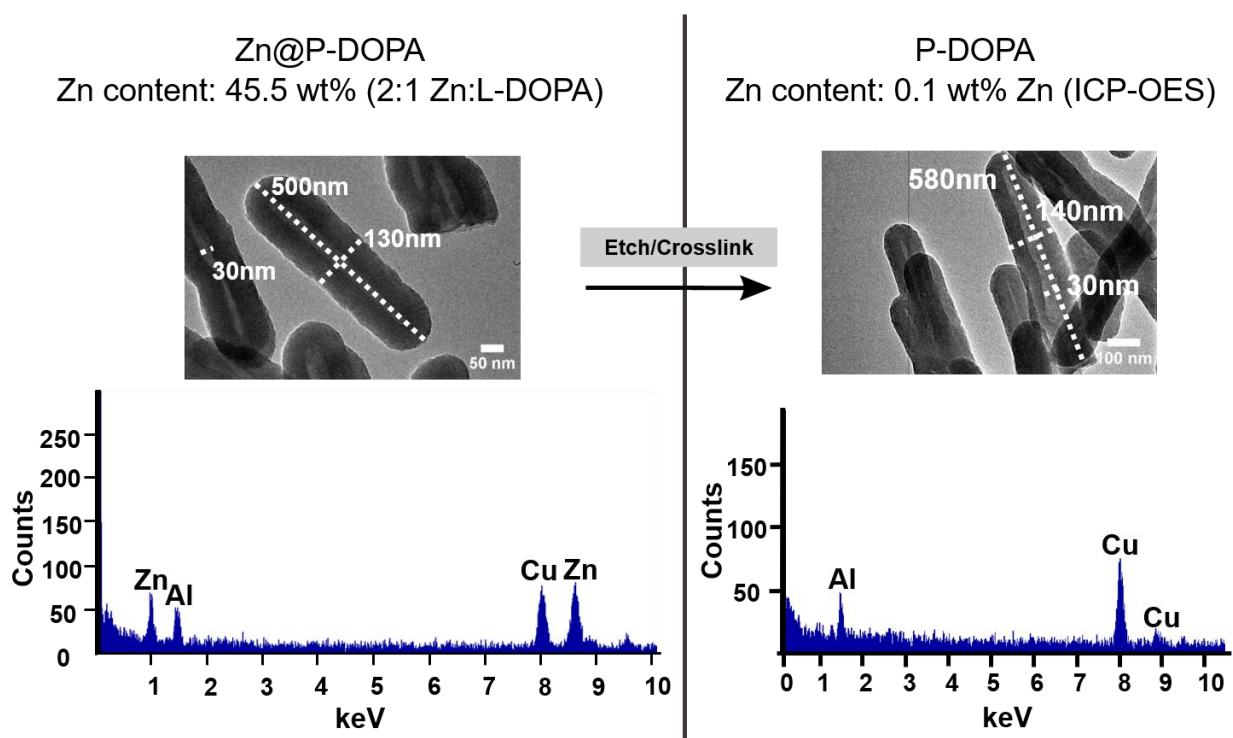
Figure 4.5 STEM-EDS analysis of ZnO template etching from P-DOPA long rods.

After verification by STEM and STEM-EDS, the particles were also characterized by dynamic light scattering (DLS) and zeta potential (Figure 4.6). Long P-DOPA rods were excluded from the DLS analysis, as their aspect ratio is not well reflected in the hard sphere approximation modeled by the automated DLS instrument calculations. All particles had relatively low dispersity with peaks around the 200 nm diameter range, except for the small PDA particles, which were more prone to aggregation. This aggregation led to an artificially increased diameter and a widened distribution.
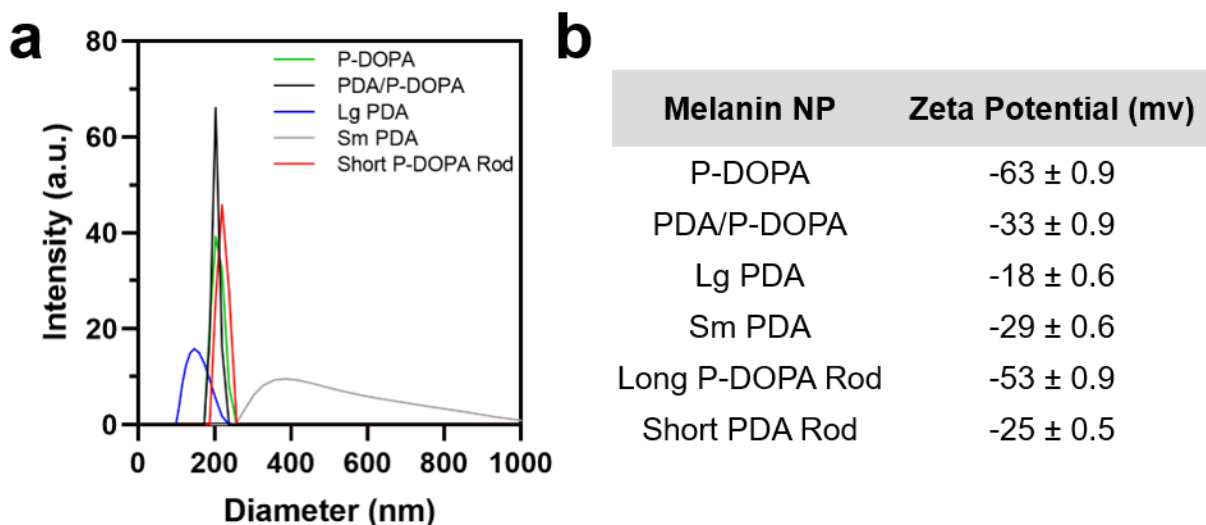
Figure 4.6 Characterization of melanin library. (a) DLS (b) Zeta potential.

Zeta potential was also assessed to determine the colloidal stability. All particles had large, negative zeta potentials, with particles containing P-DOPA having lower zeta potentials overall in comparison to the PDA. This is to be expected given the additional, readily ionizable carboxylate group (pKa ~ 2).[157] Surprisingly, the small PDA particles had a lower zeta potential than the larger PDA particles, which is not reflective of the instability and tendency for aggregation seen in the small particles over the larger ones. Nevertheless, neither were as stable as the P-DOPA containing particles, which is a consideration for future particle chemistry.

4.2.2 Cellular Uptake and Cytotoxicity of Melanin Library

To investigate the biocompatibility of our melanin mimics, NHEK were incubated with 0.02 mg/mL MelNPs for 24 hours. We aimed to determine whether our particles would be internalized by NHEK and recognized in the same manner as endogenous melanin. In the natural system, melanin is passed from melanocytes to keratinocytes, where it is then shuttled to the apical side of the perinuclear region to serve as a protective "cap" against radiation. Indeed, all the

materials, even the long aspect ratio rods, were packaged into the expected asymmetrical cap shape

in the perinuclear region, as evidenced by confocal micrographs (Figure 4.7).

Scale bars = 20 μm (cells), 200 nm (STEM)
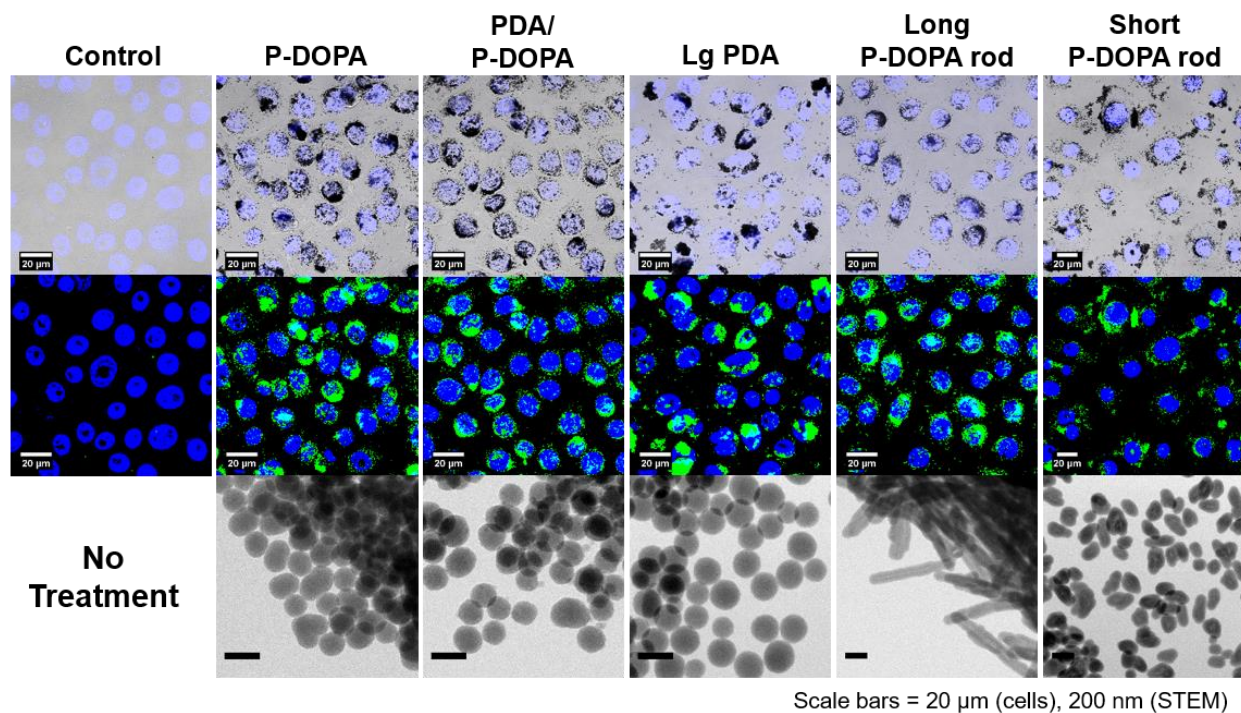
Figure 4.7 Uptake of melanin library in NHEK cells by confocal microscopy. Cells were treated with 0.02 mg/mL for 24 hours. The top row shows bright-field images overlaid with DAPI (nucleus, blue). The middle row shows a false color representation of the top row images, whereby the black perinuclear caps are colored green for easier viewing. The bottom row shows the corresponding STEM images of the particles used for the cell experiments. Small PDA particles were not used for this experiment due to increased aggregation in the cell media.

Bright-field images (Figure 4.7, top row) reveal black melanin structures, which are more easily

visualized when false-colored to a bright green color against the blue nuclei and a dark background

(Figure 4.7, middle row). To determine whether the particles could penetrate more complex cell

cultures, NHEK were partially differentiated *via* a calcium switch into high calcium media, which

is a major signaling cue in keratinocytes and triggers differentiation (Figure 4.8). The cells were

plated to confluence and then left to proliferate over 24 hours after the switch to media containing

1.2 mM CaCl$_2$. This resulted in a culture 1-2 cells thick with high density. The cells were treated

with 0.04 mg/mL PDA, P-DOPA, long P-DOPA rod, or short P-DOPA rod for 24 h, and then

imaged *via* confocal microscopy. In all cases, the particles were taken up by the partially

differentiated cells, indicating there may be promise for penetration and/or adhesion on the skin.

Scale bars = 20 µm
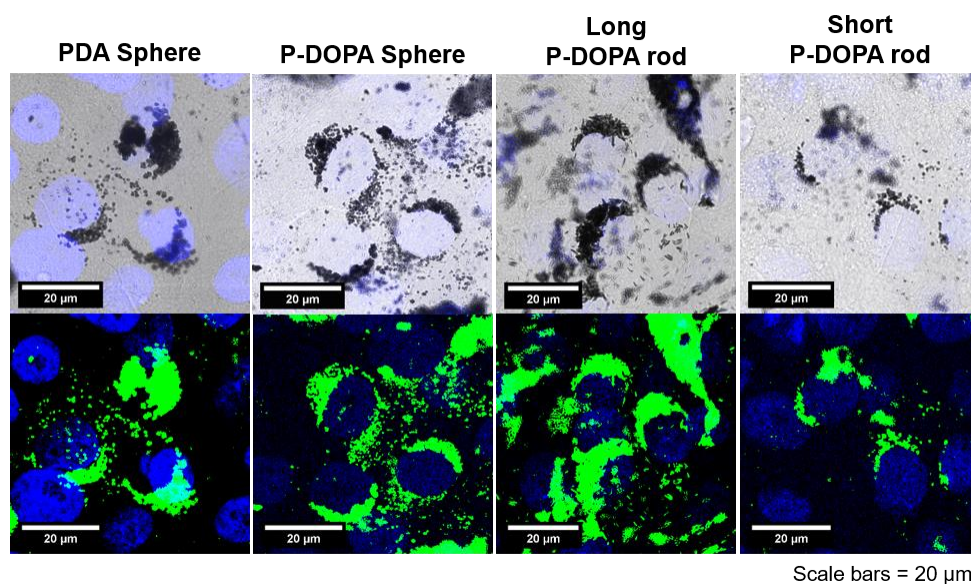
Figure 4.8 Uptake of melanin library in partially differentiated NHEK cells by confocal microscopy. Cells were treated with 0.04 mg/mL melanin particles for 24 h and then imaged. The top row shows bright-field images, and the bottom row is false-colored green for the melanin and blue for the nuclei. Scale bars 20 µm.

To assess the biocompatibility of MelNPs in human cells, NHEK were treated at 0.04 mg/mL of

each melanin particle for 24 h, the cells washed three times with phosphate buffered saline (PBS)

to remove excess melanin particles, and the CellTiter-Blue® reagent in cell media was added. This

assay provides a fluorescent method for monitoring cell viability and is based on the reduction of

a resazurin dye into resorufin, which is measured using a plate reader. This process is only possible

for metabolically healthy cells; therefore the fluorescent signal is directly proportional to the

amount of healthy cells in the culture. The cells were incubated at 37 °C for 4 hours with this

reagent, and the absorbance of the solutions at 590 nm was recorded. All particles showed good

cell compatibility, with viabilities averaging around 92%.
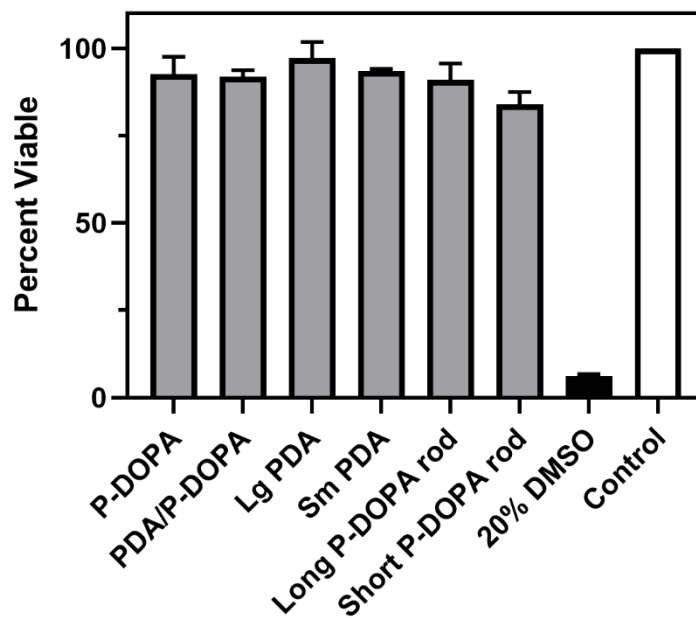
Figure 4.9 Cell viability for melanin library. Cells were treated at 0.04 mg/mL for 24 h and then the viability assessed using the CellTiter-Blue® assay.

These results were compared to a DMSO-treated control which showed 6% cell viability. The biocompatibility of such different types of melanins points to a possibility that other, even more exotic melanins, can potentially be used for biological applications in human cells.

4.3 Conclusion

We have demonstrated the synthesis of a melanin library using not only traditional PDA but also P-DOPA and P-DOPA incorporated into PDA, and also the synthesis of long and short aspect ratio P-DOPA hollow rods. These melanin mimics were characterized by electron microscopy, scattering, and other methods, and for the most part, they showed good uniformity, low dispersity, and high colloidal stability, as evidenced by their largely negative zeta potentials. The materials were fed to NHEK cells and they showed low toxicity, forming perinuclear

structures similar to those found in naturally melanized cells. This effect was also apparent for partially differentiated cells. This work demonstrates that unique melanins with varying chemistries and morphologies are biocompatible and may one day potentially be used for applications in sunscreens, cosmetics, and therapeutics. Future studies will involve testing these materials for their protective capabilities related to radiation and toxin exposure.

4.4 Experimental Details

Reagents. Dopamine hydrochloride (99%) was purchased from Alfa Aesar. Sodium hydroxide (NaOH) (extra pure), potassium permanganate ($KMnO_4$) (99%), and all other chemical reagents were purchased from ThermoFisher Scientific unless otherwise noted. Ultrapure water was purified using a Branstead GenPure xCAD Plus system from ThermoFisher Scientific and used in all experiments. All grids for transmission electron microscopy (TEM) and scanning electron microscopy (SEM) were purchased from Electron Microscopy Sciences (EMS) unless otherwise noted. Lacey carbon, 300 mesh, copper grids were purchased from Ted Pella. Grids were surface plasma treated using a PELCO easiGlow glow discharge cleaning system. Cell viability was performed using the CellTiter-Blue® reagent (Promega). Neonatal human epidermal keratinocyte (NHEK) cells were donated by the Bethany Perez-White Lab at Northwestern University Feinberg School of Medicine. All other cell culture reagents were acquired from ThermoFisher Scientific.

Instrumentation. SEM images were acquired either on a Hitachi S4800-II or a Hitachi SU8030. Dry state TEM of nanoparticles was conducted on a Hitachi HD-2300 STEM at an acceleration voltage of 200 kV. Hydrodynamic diameters and zeta potentials were measured on a

Zetasizer. Cell viability assays were read on a Biotek Synergy Neo2 plate reader. Confocal images were obtained on a Leica SP5 laser scanning confocal microscope.

4.4.1 Particle Synthesis and Characterization

Synthesis of PDA Nanoparticles. PDA nanoparticles were synthesized in the same manner as described in section 2.4.2, through the oxidative self-polymerization of dopamine in water at room temperature with a small amount of NaOH.[82] Two sizes of PDA particles were synthesized in the same exact manner, albeit with a larger volume of NaOH injected into the reaction for the small PDA particles. Typically, 150 mL of ultrapure water was fully mixed with 300 mg dopamine hydrochloride under stirring at room temperature for about 15 mins. Subsequently, 1.45 mL of 1 M NaOH (large PDA) or 1.6 mL of 1 M NaOH (small PDA) was quickly injected into this solution. After 24 h, the particles were separated by centrifugation (10,000 rpm, 10 min) and washed with ultrapure water three times.

Synthesis of P-DOPA Spherical Nanoparticles. 210 mg of L-DOPA was dissolved in 150 mL of water in a round-bottom flask and stirred vigorously for 15 minutes to ensure complete dissolution. To this, 0.90 mL of 1 N $KMnO_4$ was quickly injected into the solution and the reaction stirred overnight. The particles were separated by centrifugation (10,000 rpm, 10 min) and washed with ultrapure water three times.

Synthesis of PDA/P-DOPA Spherical Nanoparticles. 500 mg of dopamine hydrochloride and 340 mg of L-DOPA were dissolved in 200 mL of water in a round-bottom flask and stirred vigorously for 15 minutes to ensure complete dissolution. To this, 2.6 mL of 1 M NaOH was quickly injected into the solution and the reaction stirred overnight. The particles were separated by centrifugation (10,000 rpm, 10 min) and washed with ultrapure water three times.

Synthesis of P-DOPA Rods. Both the short and long P-DOPA melanin coated rods were synthesized in the same manner after obtaining the ZnO template. For the long rods, the template was a commercially available ZnO nanowire (50 nm × 300 nm) (Sigma). The short rod ZnO template was synthesized by mixing 14.75 g zinc acetate in 60 mL MeOH and 7.40 g of KOH in EtOH. This mixture was stirred at 85 °C for 72 h and the resulting nanorods were purified by a series of centrifugation cycles in Milli-Q water (3 x 10,000 rpm for 10 minutes).

To make either of the P-DOPA melanin coated rods, 16 mg L-DOPA was dissolved in 100 mL of Milli-Q water in a round-bottom flask and stirred for 15 minutes to ensure complete dissolution. To this, 17 mg ZnO rod template in 60 mL of Milli-Q water was added, and the suspension sonicated for 5 minutes. The reaction mixture was then stirred vigorously for 20 hours, resulting in a black color. The resulting coated particles were purified by centrifugation (10,000 rpm, 10 min) to remove any unbound monomer in three washing cycles with Milli-Q water. To etch out the ZnO template and further crosslink the particles, they were resuspended in 30 mL of Milli-Q water and stirred overnight with 60 mg of ammonium persulfate. The particles were once again cleaned by centrifugation (10,000 rpm, 10 min) by three washing cycles in Milli-Q water.

4.4.2 Cell Studies

Primary neonatal epidermal keratinocyte (NHEK) cells were isolated from freshly excised neonatal foreskins and gifted by the Perez-White lab at Northwestern Feinberg School of Medicine. Tissue was collected under a protocol approved by the Northwestern University Institutional Review Board (IRB# STU00009443). Patients' consent for neonatal foreskin tissue (for primary keratinocyte isolation) and human tissue sections from truncal skin (obtained from abdominoplasty) were not required as these tissues are de-identified and considered discarded material per IRB

policy. To isolate the cells, the tissue was treated overnight with dispase and then incubated with 0.25% trypsin with 1 mM EDTA for 10 min at 37 °C. The trypsin was neutralized with FBS, the cells suspended in phosphate-buffered saline (PBS), filtered through a 40 μm sieve, and then centrifuged at 1,000 rpm for 5 minutes. The cell pellets were resuspended in, and subsequently maintained in, M154 medium supplemented with human keratinocyte growth supplement (HKGS), 10 μg/mL gentamicin, 0.25 μg/mL amphotericin B, and 0.07 mM $CaCl_2$, and maintained at 37 °C with 5% CO_2. For differentiation studies, the cells were plated to confluence in 0.07 mM $CaCl_2$-containing media, then switched to 0.03 mM $CaCl_2$ for 24 hours, and then again switched to the high calcium media containing 1.2 mM $CaCl_2$ for 24 hours to induce the early stages of differentiation.

Cell Viability. NHEK were seeded overnight in 48 well plates with a volume of 250 μL per well, and then incubated with melanin nanoparticles at a final concentration of 0.04 mg/mL, the vehicle (sterile water), or 20% DMSO for 24 hours. After 24 hours, they were carefully rinsed with DPBS three times, and then 50 μL of the CellTiter-Blue® (Promega) reagent was added to each well. The cells were then incubated for 4 hours at 37 °C. Absorbance of the converted resorufin product at 590 nm was recorded. Results are an average of three biological repeats.

Confocal Microscopy. NHEK were incubated with 0.02 mg/mL melanin particles for 24 hours, rinsed three times with PBS, fixed with 4% paraformaldehyde, and then stained with DAPI. Bright-field images were overlaid with the DAPI channel to orient the black signal from the melanin around the nucleus. False colored images were created in ImageJ (FIJI) by colorizing the black melanin caps in the bright-field channel to green for better visualization of the cap structure.

Chapter 5. Skin Applications of Synthetic Melanins

5.1 Introduction

Melanin is most famous for its role in the pigmentation of human skin. It serves as the primary "natural sunscreen" that shields against UV radiation (UVR) from the sun, protecting nuclei from DNA damage. Human ancestors were primarily located in equatorial environments, and as they became more active, they started losing more body hair and gaining more sweat glands in order to cool themselves faster. This resulted in more skin being exposed to the sun, and an increase in melanin pigmentation which was previously primarily located on the face.[158] This increased melanization allowed for early members of the genus *Homo* to lead active lives in hot climates such as in Africa. As humans migrated away from the equator, these further latitudes afforded less overhead direct sunlight, which decreased their ability to synthesize vitamin D. Therefore, a high degree of skin melanization became less advantageous, as it made the already scarce sunlight even less available. This resulted in the eventual selection of depigmentation over time, which evolved independently in Europe and East Asia.[158] However, in this modern age, humans are more mobile than ever, and there is a mismatch between the genetic expectations of sun exposure, and the climate of residence. Furthermore, there are additional avenues to readily obtain sun exposure such as traveling to hotter climates and artificial tanning beds. This has led to the advent of chemical sunscreens for the protection of the skin from UV damage, which can lead to burns and cancer.

Skin cancers stem result from UVR exposure and make up half of all cancers in the USA. There is evidence that regular use of sunscreen is effective at prevention of squamous cell carcinoma.[159] The first sunscreens were formulated in the 1930's, and one of the earliest patented

sunscreens was a red jelly called "Red Vet Pet" which was created to protect soldiers from the harsh sun of the tropics in World War II. Sunscreens have come a long way from their earliest iterations, with low sun protection factor (SPF) and sticky finish.[160] In modern days, there are two main classes of sunscreens on the market; nano- or microparticle-based TiO_2 or ZnO "mineral sunscreens" which have semiconductor-like electronic properties which make them very effective at absorbing UV light, or "chemical sunscreens" made from aromatic small molecules containing multiple conjugated π-electron systems which absorb UVR and dissipate the energy as heat.[161, 162] These chemical sunscreens are effective agents against UVR, however there is growing concern regarding their systemic safety in the human body[163, 164] and adverse environmental effects.[165, 166] So-called mineral sunscreens have been praised for being "natural" and "safe" for their broad spectrum absorption and low degree of skin penetration, but some studies suggest they can penetrate the skin to various degrees, and that other routes of exposure such as through the respiratory and digestive tracts warrant consideration.[167] In addition, mineral sunscreens are very efficient at scattering visible light, displaying a white, chalky cast onto the skin, which is highly undesirable, especially on people with darker complexions. This issue can be somewhat circumvented by decreasing the particle size from the micron scale to the nanoscale (~200 nm or less for ZnO and ~10-20 nm for TiO_2), but this can change the optical properties, and increases concern for penetration into the skin, especially in compromised skin.[167] Nevertheless, these sunscreen products are widely popular for their prevention against skin cancers and premature aging because there are simply no other alternatives for mitigating sun exposure aside from wearing protective clothing.

Despite the popularity of sunscreen products, there is a discrepancy between the desire for

protection from the harmful effects of UVR, and the desire for increased melanization of the skin for cosmetic purposes, especially in Western societies, which naturally necessitates sun exposure. In certain cultures, having a tanned appearance is considered beautiful, but the best way to achieve a natural tan is by exposing oneself to the sun. It is not impossible to increase melanization while wearing traditional sunscreens, as they are not 100% effective, but it is made more difficult as the process takes much longer and produces a much less pronounced effect. Tanning products (lotions, creams, gels, foams, sprays) were first introduced in the 1960's as a lotion which produces an artificial tan color after application, independent from the melanization process. However, these products suffer from a host of issues. The two chemicals used for artificial tanning are dihydroxyacetone (DHA), and less commonly, erythrulose, which both form a brown color upon reaction with the proteins of the stratum corneum, in a well-known reaction called the "Maillard reaction." The Maillard reaction is a chemical reaction between amino acids and reducing sugars, and is most commonly referred to in the context of food browning as it cooks or bakes. When this reaction occurs in the skin after application of tanning products, it results in a significant, unpleasant odor which is difficult to remove and lasts several days. The resulting skin color is generally an orange tone which does not resemble a natural looking tan. Even more unfavorable are myriad potential health effects resulting from the use of these active ingredients, specifically DHA (much less information exists for erythrulose). The Maillard reaction forms glycotoxins which can cause oxidative stress and inflammation in large quantities and are implicated in several degenerative diseases such as Alzheimer's disease. DHA can also increase susceptibility to free radicals, even hours after application.[168] Lastly, there is additional growing evidence that DHA can penetrate into the basal layer of the epidermis and the dermis, and that chronic inhalation *via*

spray tanning booths may increase the risk for pulmonary disease.[169]

For these reasons, there exists a need for alternative sunscreens and skin tanning agents, ideally by mimicking the natural system by creating an artificial melanin that is chemically and visibly similar to human melanin, or improving upon what nature has provided by designing synthetic materials that mimic or enhance other types of melanin chemistries found in nature.

Synthetic melanin is a promising material for the coloration and protection of human skin since it has color that is similar to that produced by endogenous melanin, and is biocompatible and biodegradable. One can envision that if melanin is the skin's major natural pigmentation and protection system, that a synthetic version mimicking the natural system could augment these properties, especially if the chemistry could be optimized to increase the response to UV radiation damage, including reactive oxygen species (ROS), and circumvent concerns with existing products. Despite the potential promise of bio-inspired mimics as alternative products, such synthetic analogues have been studied very little for their ability to interact with human skin cells, epidermal equivalents, and especially intact human skin. Part of this lack of information is likely due to the fact that well-defined and well-characterized synthetic melanins have only really been developed in the last decade or so. Additionally, what little work has been done has been explored almost exclusively on polydopamine (PDA)-based systems, and usually in mice or in cells; not on human skin.[48] Mice are much easier to access for these studies than recently excised, intact human skin, and there is value to this experimental approach. However, there are ethical issues surrounding the use of animals for cosmetic testing purposes and many consumers prefer "vegan" alternatives. Animal studies are required in certain cosmetic markets, such as in China, but they are avoided in others, such as in Europe and the United States. In addition, the skin of a mouse, although

appropriate for a variety of preliminary studies, is known to be physiologically and genetically distinct from that of human skin.[170, 171] Therefore, it is ideal to begin testing *in vitro* in human cell lines and 3D tissue mimics, or in human skin, wherever possible.

Bio-inspired mimics of melanin-like materials have been explored a great deal in the last several years, however they are generally engineered for materials science applications rather than so-called "cosmetic" or "cosmeceutical" applications along the lines of self-tanning agents and sunscreens. In addition, a narrow focus almost exclusively on PDA-based systems excludes many of the different chemical precursors found throughout the melanin biosynthesis pathway in humans, such as L-DOPA, as well as melanin chemistries found in other organisms. This begs the question of what these alternative chemistries could achieve when applied to biological systems. Recent work has attempted to branch away from this adherence to a eumelanin-based, and specifically PDA-based, approach to develop synthetic analogues of pheomelanin,[17] which is found in humans, birds, insects, and other organisms. Pheomelanin is chemically distinct from eumelanin due to the incorporation of sulfur, contributed by the addition of cysteine. Although recent attempts at expanding the chemical diversity of artificial melanins have been exciting and promising, there is almost a total lack of synthetic efforts and applications of constructs that mimic melanins not found in humans. This is especially apparent in systems found in plants and fungi, namely allomelanins and pyomelanins. There are a few recent examples of synthetic allomelanin, which is naturally formed from naphthalene- and catechol-type monomers, utilized by fungal systems to shield them from radiation. These fungi have been found in some of the harshest environments imaginable, such as at the Chernobyl nuclear power plant, and on spacecraft. They thrive in environments with high radiation levels, giving their melanization process a special interest.[6, 49, 50] By polymerizing

the monomer 1,8-dihydroxynaphthalene (1,8-DHN), a new artificial allomelanin was synthesized as a well-defined nanomaterial with antioxidant capabilities, as described in Chapter 2. To-date, no well-defined or well-characterized synthetic constructs of pyomelanin have been formulated. This is likely due in part to the more exotic nature of pyomelanin, found mainly in microorganisms and plants, and lack of information on the natural system. This is likely also due to the seemingly soluble nature of pyomelanin, making it vastly structurally different from all other melanins, which are known to be highly insoluble.

Previously, PDA-based eumelanin nanoparticles have been shown to internalize into adult human epidermal keratinocytes (HEKa) in monolayer cell culture, with low toxicity, and protect the cells from UVA irradiation.[47] Allomelanin-based nanoparticles were also shown to be biocompatible in neonatal human epidermal keratinocytes (NHEK) and form the same type of perinuclear structures found in the natural eumelanin and synthetic PDA melanin systems. They also showed antioxidant capability and subsequently protected the cells from ROS generated upon UVA exposure.[172] This work paves the way to explore the interaction with both a traditional eumelanin mimic, PDA, and a more novel fungal melanin mimic, 1,8-DHN-based allomelanin, in more complex models of human skin.

Human skin is comprised of three main layers- hypodermis, dermis, and epidermis (Figure 5.1, hypodermis not shown). The epidermis is the most superficial layer of the skin, and it is also the layer that is melanized. The epidermis consists mainly of two types of cells- melanocytes, which synthesize melanin, and keratinocytes, which utilize melanin and make up the bulk of the epidermis. Melanocytes reside in the basal layer of the epidermis and their purpose is to synthesize melanin. After synthesis of melanin is complete, it is transferred to nearby keratinocytes *via*

specialized lysosome-related organelles called melanosomes. Each melanocyte has finger-like projections which reach out to serve approximately 36 basal keratinocytes, but this ratio can differ depending on a variety of factors.[156, 173] The mechanism of this transfer is still debated and not fully understood, with several theories on how the process occurs. It is thought that melanosome transfer involves membrane fusion, vesicle transfer, phagocytosis, or cytophagocytosis.[174]
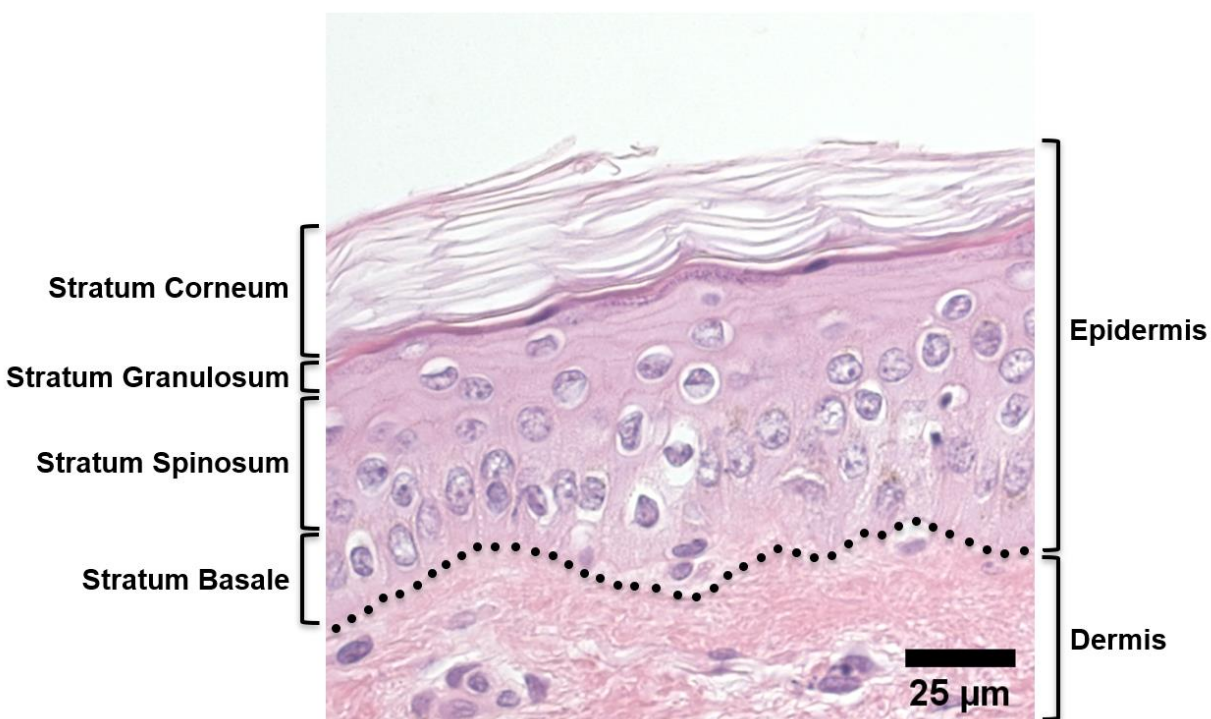
Figure 5.1 The anatomy of human skin. A 4 μm section of Caucasian human truncal skin (obtained from abdominoplasty) stained with hematoxylin and eosin (H&E) is labeled with the layers of the epidermis (left) and the the epidermis and dermis (right). The dotted line represents the dermal-epidermal junction (basement membrane).

Regardless of the specific transfer mechanism, it is established that nearby keratinocytes internalize melanosomes and shuttle them to the perinuclear region, where they are then arranged in a cap-like fashion.[98, 99] These asymmetrical caps reside on the side of the nucleus/cell facing the outer surface of the skin, in the direction which UV light from the sun penetrates, where they serve as radiation protection agents (Figure 5.2). Keratinocytes actively internalizing melanin also reside

in the basal layer of the epidermis alongside melanocytes, and are mitotically active, undifferentiated cells. However, there are many different layers of keratinocytes in the epidermis, situated above the basal layer, which exist in varying degrees of differentiation, triggered largely by a steep calcium gradient.[100] These cells possess unique biochemistry and morphology in every layer, despite the fact that they are all keratinocytes. In fact, the uppermost, terminally differentiated keratinocytes of the epidermis are termed corneocytes, and have little in common with basal keratinocytes.
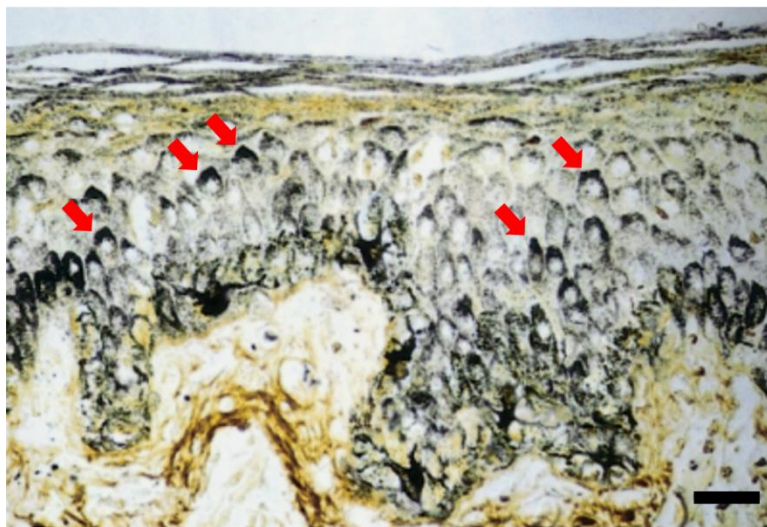
Figure 5.2 Micrograph of highly melanized human epidermis illustrating supranuclear cap structures, stained using the Fontana-Masson silver stain. Several representative melanin "caps" are denoted with red arrows. Scale bar 50 μm. Adapted and reproduced with permission, 2003 Elsevier.[99]

Corneocytes are highly keratinized, fully differentiated, anuclear cells which tightly associate to form a nearly impenetrable tissue layer called the stratum corneum (SC). Originally likened to a "brick and mortar" configuration,[175] the SC is a continuous, proteinaceous structure composed of corneocytes containing lipids and tight intercellular connections called corneodesmosomes.[176] The major purpose of the SC is as a barrier against water loss, and this hydrophobic epidermal layer

also occludes external agents from the body. It is very good at keeping out nanoscale objects, for example.[177, 178]

With a basic understanding of skin physiology and the melanization process, an approach to artificially mimicking the pigmentation process could be envisioned in two ways. First, this could be achieved by using a synthetic melanin material which can penetrate the SC and enter individual cells in the same manner as was shown previously in the monolayer cell culture studies. Second, it could be accomplished by forgoing the penetration of individual cells, or even tissues, and instead forming a melanized layer of material on the surface of the skin. The obvious drawback to the first approach is that melanin is formed both endogenously and synthetically as nanoscale objects on the order of 30 nm to hundreds of nanometers which is generally too large to penetrate the tightly-layered SC.[1, 174, 179] Nanoparticles have been investigated many times for transdermal delivery, but in general, they do not penetrate through the full width of the stratum corneum, and if they do, they generally cannot pass through to the basal layer. In addition, many of the particles that do manage to penetrate, to any extent, are generally very small (<10 nm), metal-based, and are more likely to penetrate skin that is somehow compromised by either disease or other methods of force.[180, 181] Transdermal delivery may also not be desirable, and it may be preferable to deliver a topical therapeutic or active ingredient, especially in the case of a sunscreen, that can act locally while avoiding systemic circulation. This leads to the second approach, which involves a mechanistically distinct method for protecting the skin, and instead of relying on protection of the cells from an intracellular perspective, it seeks to answer whether an outer coating, many microns above the surface of an active keratinocyte, could provide much of the same protections as the internalized materials. Indeed, existing mineral sunscreens function in much the same manner,

although they rely on a mechanistically distinct protection method as they scatter light and are not generally known to mitigate the ROS response. This then begs the question of whether melanin mimics, which have previously shown to quench ROS in monolayer cell culture, can confer a similar chemical interaction to nearby keratinocytes in the absence of cell penetration, and whether this application results in a tanned appearance that mimics that of naturally melanized skin. We begin this investigation by probing the effects of treating keratinocytes *in vitro*, then examining more complex human skin equivalent cultures, and lastly testing the materials on porcine and human skin. This study also requires the exploration of various potential vehicles and formulations for enhancing visually appealing coloration as well as adherence to the skin. To date, these questions have not yet been answered, and this chapter will attempt to explore routes to this end, and future directions for this work.

5.2 Results and Discussion

5.2.1 Synthesis and Characterization of Melanin-Based Materials

A variety of synthetic melanin nanoparticles were utilized in various aspects of this study, including eumelanin mimics (polydopamine (PDA) spheres, poly-L-DOPA (P-DOPA) spheres, and P-DOPA short rods), and a spherical 1,8-DHN-based allomelanin mimic (AMNP). The synthesis of these materials is described in section 2.4.1 (AMNP), 2.4.2 (PDA spheres) and section 4.2.1 (P-DOPA spheres and rods). All PDA- and AMNP-based melanin mimics described are spherical in morphology, and the distinction between P-DOPA rods and spheres will be made wherever necessary, assuming a spherical nature if not specified. Two types of P-DOPA rods were synthesized- a short aspect ratio, termed short P-DOPA rods or sh. P-DOPA rods, and a longer

aspect ratio P-DOPA-based rod, termed long P-DOPA rods, or lg. P-DOPA rods. All AMNP not specified with a number (*i.e.* AMNP-1, AMNP-2, or AMNP-3) are assumed to be AMNP-1.

5.2.2 Skin Tanning Applications

Keratinocytes in culture maintain a translucent/colorless to whitish appearance, discernable by the human eye after centrifugation of a large number of cells to form a visible pellet. However, upon treatment with artificial melanin particles, the cell cultures take on a darker appearance after internalization of the material, and the pellet appears dark brown to black in color. We tested the visual effect of this process by treating monolayer primary neonatal human epidermal keratinocyte (NHEK) cultures with several concentrations of PDA nanoparticles at two different time points. Cell which were previously clear in appearance, took on a "tanned" or a slightly brown to black
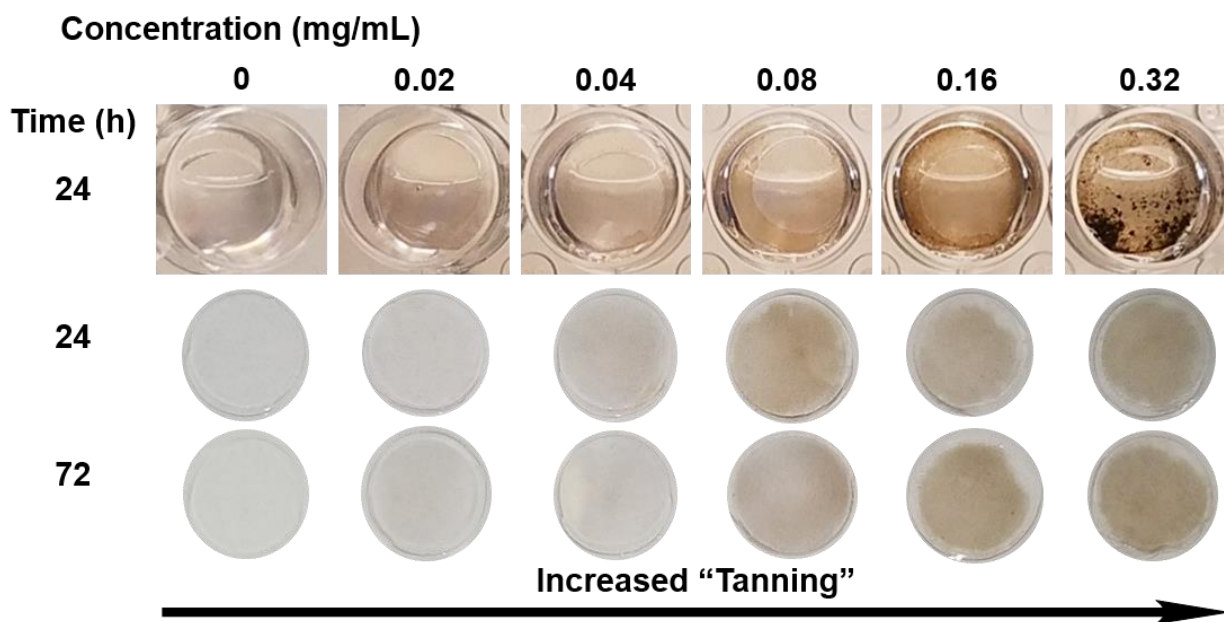
Figure 5.3 NHEK "tanning" over time. NHEK were grown on glass coverslips in 24-well plates and treated with varying concentrations of PDA (top row well plates shown for 24 h condition). The coverslips were removed and mounted onto microscope slides either after 24 h (middle row) or 72 h (bottom row). The cells show a tanning effect which increases with concentration but levels off as high concentrations of material begin to aggregate in the culture and the cells become saturated with melanin.

appearance, depending on the concentration of materials used. This showed that a monolayer of cells could be tanned artificially using synthetic melanins that are recognized in much the same manner as natural melanins (Figure 5.3). NHEK were seeded on circular, glass coverslips, left to attach overnight, and then treated with PDA for either 24 or 72 hours. They were then washed with Dulbecco's phosphate buffered saline (DPBS) three times and then mounted onto microscope slides using a hardening mounting medium. The control was treated with the vehicle, which was a negligible amount of water (~2 μL, or ~0.4% v/v). Photographs of the slides reveal tan/brown cells with shades found in naturally melanized skin. The visual effect of this artificial melanization process increases with concentration but levels off starting around 0.08 mg/mL, whereby an increase in material results in little to no additional increase in tanning color. This is likely due to the cells reaching their maximal melanin uptake coupled with the buildup of material in the medium which aggregates over time if it is not internalized.

Scale bars = 50 μm
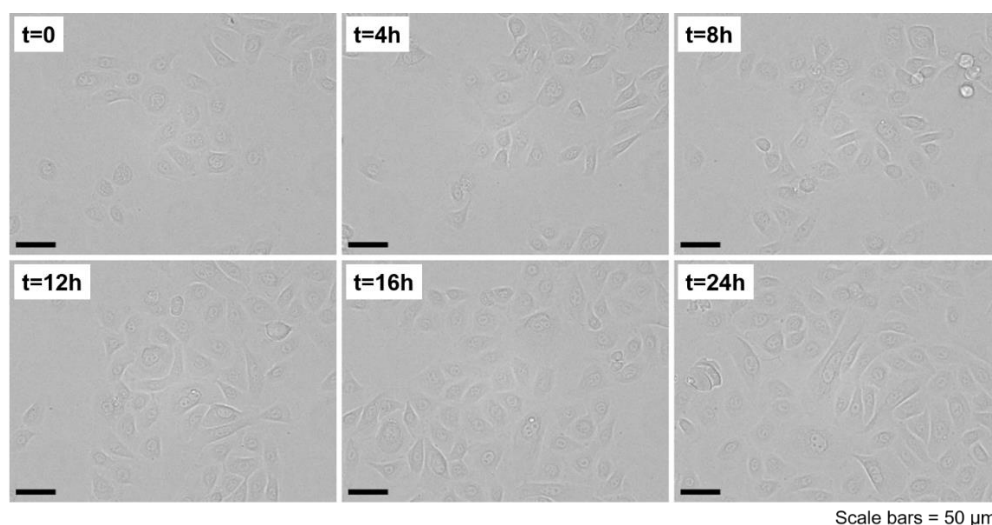
Figure 5.4 NHEK growth monitored over 24 h. NHEK were monitored for 24 hours as a control for P-DOPA-treated cells, imaging once every 30 minutes, in a humidity-controlled microscope chamber at 37 °C. Bright-field images show colorless cells which proliferate but do not darken over time.

As confirmed by confocal microscopy, concentrations of melanin above 0.08 mg/mL confer no advantage, instead leading to very dark cultures which are difficult to image. This process was monitored microscopically in a parallel experiment by incubating NHEK with P-DOPA particles for 24 hours in a humidity-controlled imaging chamber maintained at 37 °C, and the cells imaged every 30 minutes. The control experiment, vehicle (water)-treated cells, showed growth and proliferation of NHEK over time, but no darkening was observed (Figure 5.4). When the cells were incubated with 0.02 mg/mL P-DOPA, diffuse black melanin material inside the cells was first observable after 4 h, with perinuclear caps forming as early as 8 h, and continued growth of the caps even up until the last time point at 24 h (Figure 5.5). These results led us to explore how different types of synthetic melanin could induce coloration, and how that could be observed in more complex epidermal constructs.

Scale bars = 50 μm
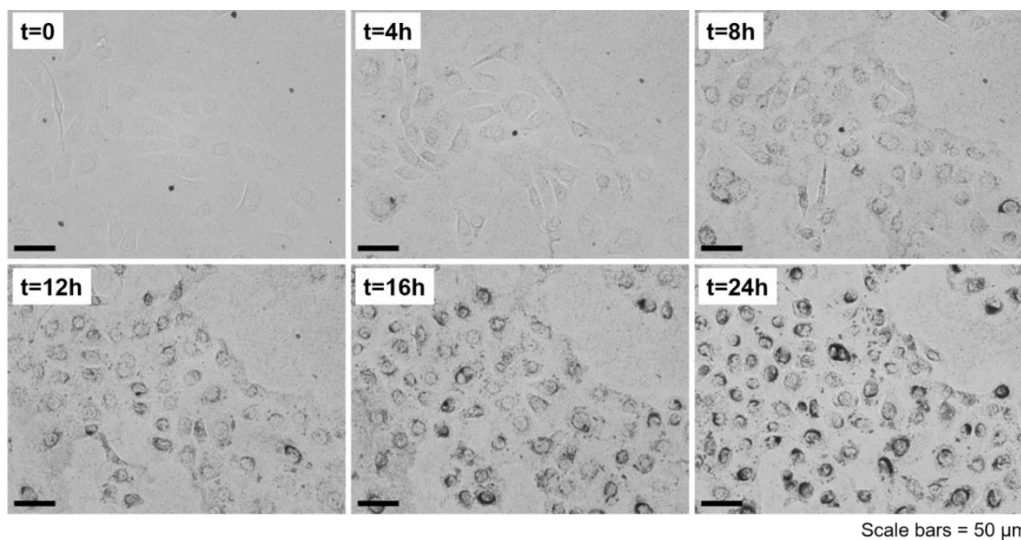
Figure 5.5 Uptake of P-DOPA in NHEK monitored over 24 h. NHEK were treated with P-DOPA particles in water at 0.02 mg/mL, and monitored for 24 hours, imaging once every 30 minutes, in a humidity-controlled microscope chamber at 37 °C. Bright-field images show colorless cells which become darker over time as they uptake melanin.

One way to achieve this is by forming a synthetic epidermis referred to as a Human Epidermal Equivalent (HEE) or Reconstituted Human Epidermis (RHE) (Figure 5.6). This engineered tissue is created by seeding NHEK to confluence in the upper chamber of a transwell system with inserts containing 0.4 µm pores. After two days, the cultures are "lifted" to the air/liquid interface by removing media from the upper chamber where they continue to proliferate and stratify for up to 12 days.

Figure 5.6 Human Epidermal Equivalent (HEE) with H&E stain, labeled with the appropriate layers of the epidermis. The clear layer below the epidermis is the plastic insert upon which the cultures are grown/maintained.

This process produces tissue which contains all the layers of a fully formed epidermis and can be used similarly to intact human skin. The advantage of this approach is that the cultures can be grown without the use of collagen plugs or fibroblasts, both animal-derived components which may not be desirable, and both which necessitate an additional step in the formation process and require the culture of multiple cell lines. Additionally, the cultures need not be "lifted" to the air interface, as is the case for other 3D culture methods, and can be fixed and sectioned with little disturbance. However, the resulting cultures are much thinner than traditional collagen-based cultures, and proper mounting of culture sections is non-trivial.

HEE were treated with suspensions of four different melanin mimics in PBS: PDA, PDA/P-DOPA, P-DOPA, or short P-DOPA rods. This led to highly pigmented cultures, and in some cases

the tissue maintained a very dark appearance even after rinsing thoroughly with PBS, with this effect most apparent in the PDA/P-DOPA and P-DOPA treatments (Figure 5.7).
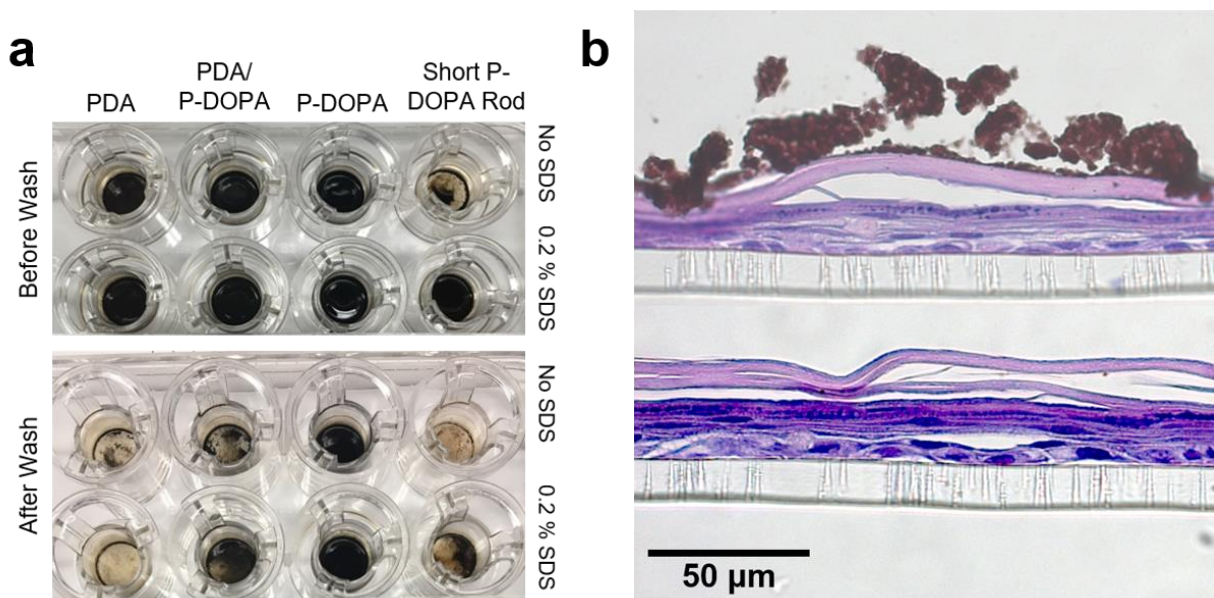
Figure 5.7 Human Epidermal Equivalent (HEE) cultures treated with 2.5 mg melanin NPs in PBS for 24 hours. (a) Images show the tissues before (top well plate) and after (bottom well plate) washing 3x with PBS. Tissues were treated with no SDS or 0.2% SDS in PBS (which was immediately removed after application), prior to NP treatment. (b) H&E stained 4 μm sections of HEE treated with spherical P-DOPA NPs (top) or no treatment (bottom) and without SDS.

To enhance penetration/adhesion of the particles, 0.2% sodium dodecyl sulfate (SDS), an anionic detergent capable of disrupting the epidermal barrier, was applied briefly to the culture surface and then immediately wiped off before applying melanin particles. The addition of SDS increased pigmentation in the tissue treated with P-DOPA, and especially P-DOPA rods. The overall effect was that PDA showed little adherence after rinsing, in either treatment, P-DOPA short rod and PDA/P-DOPA coverage was patchy and sparse without the addition of SDS, and the pure P-DOPA resulted in highly pigmented tissue (Figure 5.7a). To assess whether the particles were penetrating the tissue or remaining on the surface of the stratum corneum (SC), the cultures were fixed with 10% neutral buffered formalin, paraffin embedded, sectioned to 4 μm thick, and stained with H&E.

A comparison between the control and the spherical P-DOPA, which had the thickest visible coating, is shown in Figure 5.7b. These micrographs indicate that the melanin material sits atop the SC as a thick layer, and there was no evidence of penetration through the SC. The results were the same with all particles tested, and in all conditions. This pointed to a possible difference in monomer chemistry affecting the adherence of the particles, but as a whole the SC proved to be a formidable barrier to entry for all the materials tested. The amount of adherence, however, was promising, and therefore subsequent studies sought to determine whether this system would translate to more complex tissues, namely intact skin.

Pig skin was purchased from the local butcher shop for screening the materials to determine translation of the results obtained with HEE. Pig skin is physiologically similar to human skin and is easy to obtain, therefore serving as an ideal substrate for screening purposes.[182] It was cut into squares and sprayed with PDA particles using several vehicles- 5% or 10% diluted "ceramide complex" in water, containing ceramides, cholesterol, and fatty acids to mimic the natural environment of the epidermal barrier (Lotioncrafter.com), Milli-Q water, 25% aqueous EtOH, or 50% aqueous EtOH (Figures 5.8-5.10). EtOH is not an ideal vehicle for application over large areas of skin due to its drying and potentially irritating nature, however it is used safely in common applications such as hand sanitizers and was chosen as a non-toxic organic solvent that would evaporate quickly. Adherence of the material was similar with each vehicle, with a slight enhancement in the ceramide conditions, and increasing concentration leading to a modest increase in coloration. The appearance was patchy, with suboptimal cosmetic coloration, and the particles were easily rubbed off with filter paper or a gloved hand. The observed difference between the adherence in intact skin and the HEE could be attributed to an underdeveloped SC in the HEE

which also may contain a slightly different chemical composition than that of the skin. Additional commercial vehicles were also considered to enhance spreading and adherence to the skin. (With human skin in short supply, porcine skin was used for subsequent applications, however, when available, human skin was used for additional studies, and is discussed in more detail in section 5.2.4 in the context of UV protection.)
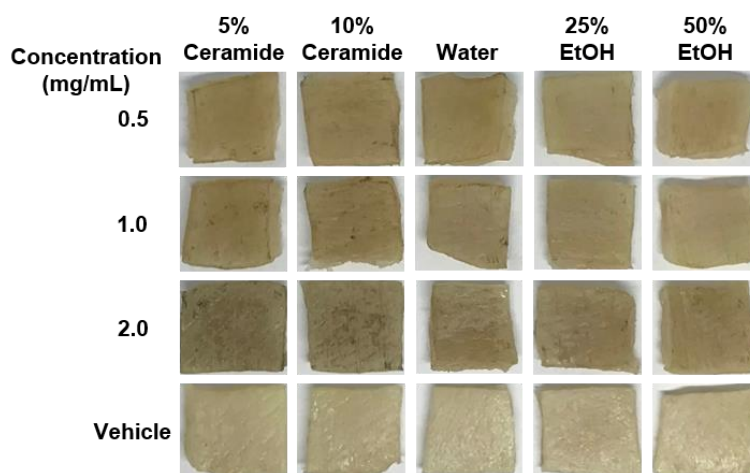
Figure 5.8 Pigskin sprayed with PDA suspended in 5% or 10% ceramide solution, water, 25% EtOH in water, or 50% EtOH in water.
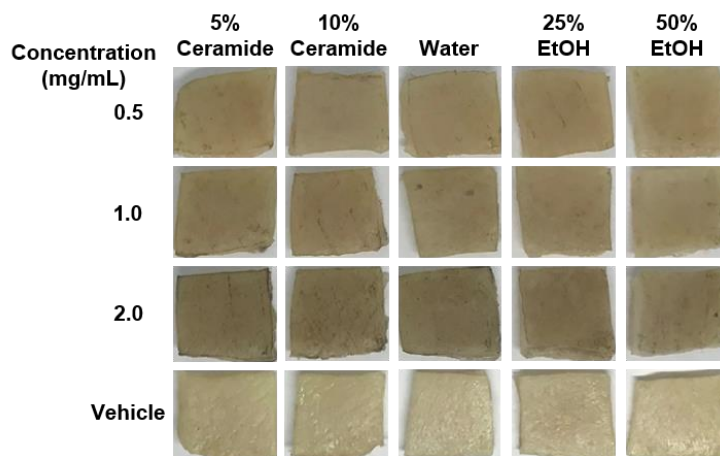
Figure 5.9 Pigskin sprayed with P-DOPA suspended in 5% or 10% ceramide solution, water, 25% EtOH in water, or 50% EtOH in water.
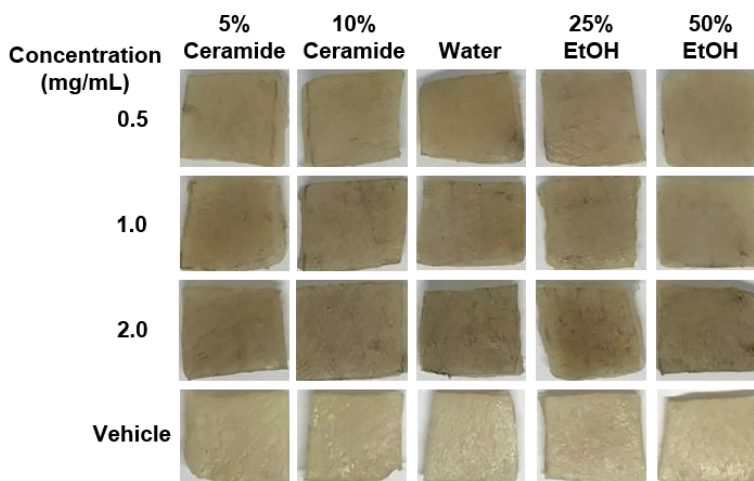
Figure 5.10 Pigskin sprayed with P-DOPA short rods suspended in 5% or 10% ceramide solution, water, 25% EtOH in water, or 50% EtOH in water.

Commercial skin and hair products were purchased to serve as a screening tool for the incorporation of PDA into various vehicles to test whether known formulations could mix well with the particles and increase spreading and adherence to the skin. Aloe vera gel, four different sunscreens, a hair mousse, and water were tested (Figure 5.11). These commercial products were chosen to represent a range of formulation types in typical skin and hair applications. Aloe vera gel is a watery, sticky gel with a translucent appearance. Two chemical sunscreens were chosen, the Neutrogena® being thicker and more "greasy" feeling, and the CeraVe® being lighter and thinner. The Alba Botanica® mineral sunscreen is extremely thick and contains ZnO and TiO$_2$ actives. The Tresemme® mousse is a light foam which is very thin and hydrophobic, drying to a sticky finish. Water is of course the natural storage solvent for these materials, and it serves as a good control against more hydrophobic formulations. The color of each formulation varied drastically with the type of vehicle it was mixed with, even at the same concentration. This points to the importance of the final formulation on the cosmetic effects, since even a single material can look different under different conditions. White vehicles produced a more gray color, whereas
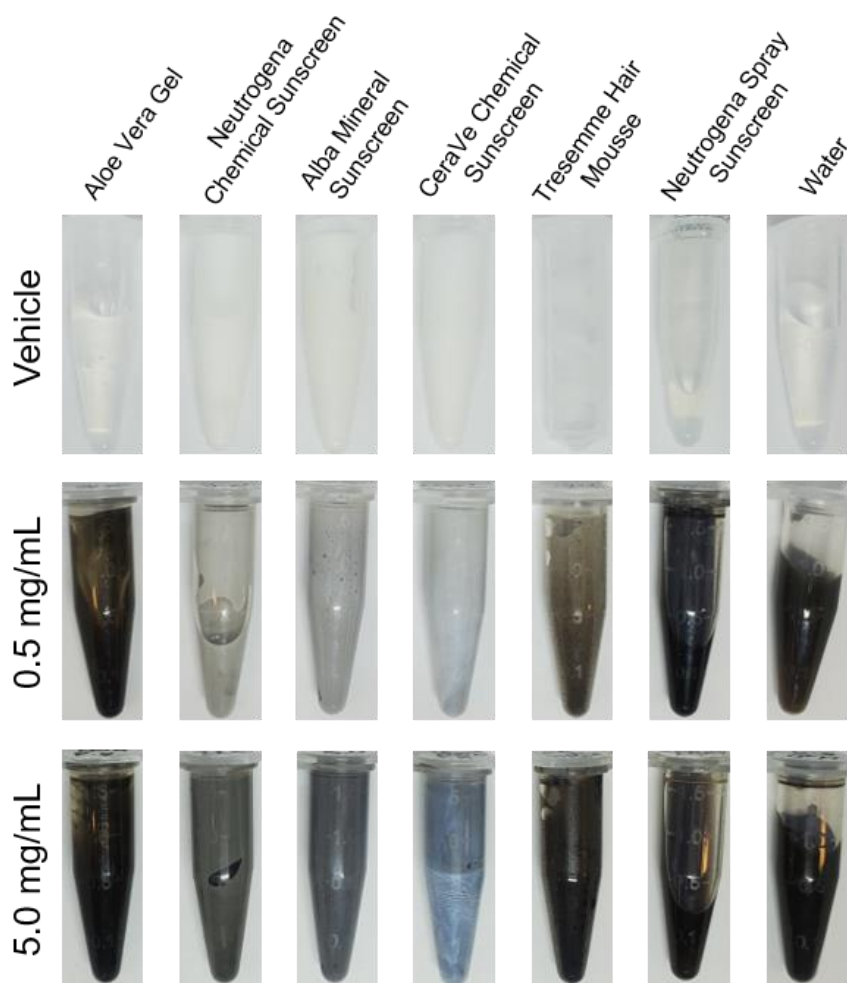
Figure 5.11 Screening of commercial products as vehicles for PDA-based melanin nanoparticles. From left to right, aloe vera gel, Neutrogena® chemical sunscreen, Alba Botanica® mineral sunscreen, CeraVe® chemical sunscreen, Tresemme® hair mousse, Neutrogena® spray sunscreen, and water.

translucent vehicles produced a more brown, warmer color. Each sample was applied to pigskin

by rubbing a small amount onto the surface using a pipette tip (Figure 5.12). While the materials

maintained strong coloration upon initial application of a thick layer, subsequent rubbing of the

skin with filter paper showed a lack of adherence, with patchy, uneven coverage. Although it

remains unconfirmed whether there remained enough material residue on the skin surface to be

useful as a sunscreen, the cosmetic outcome was not favorable. More adhesion experiments are
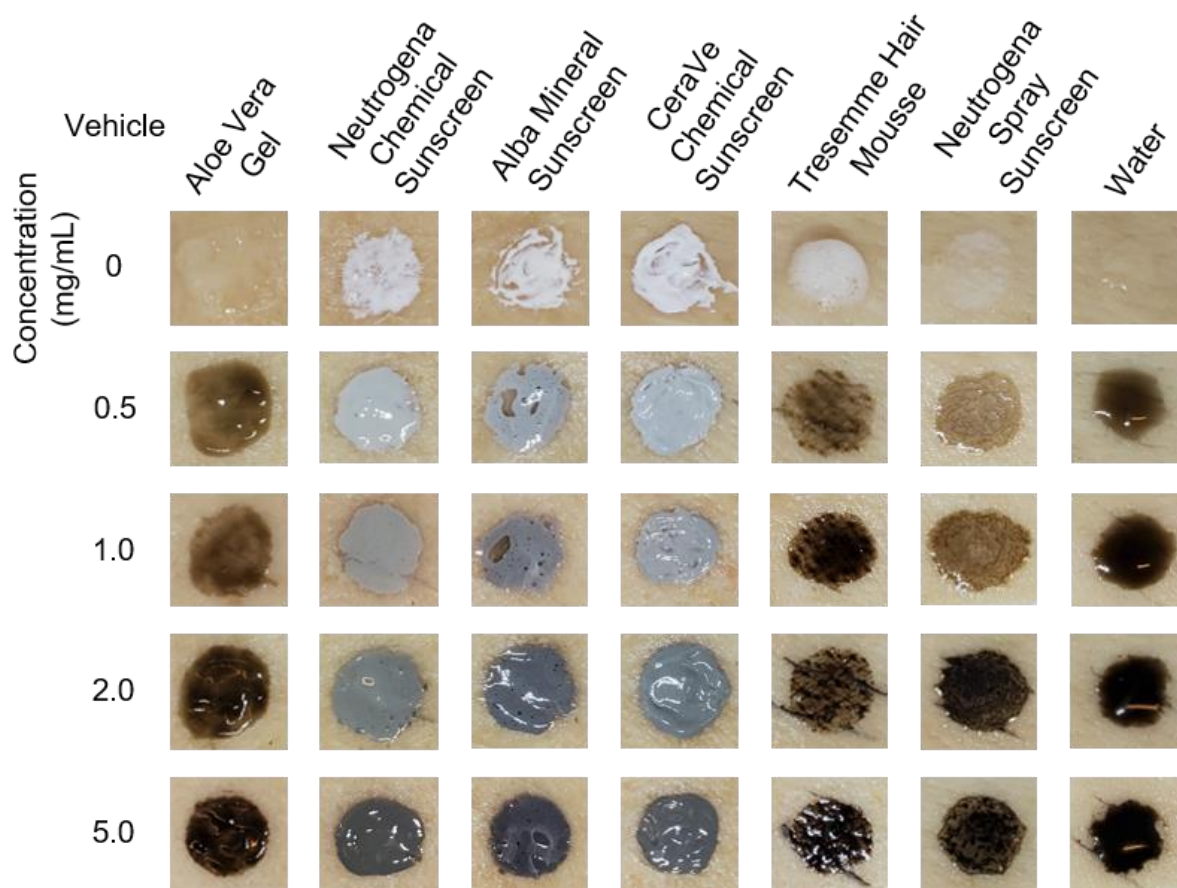
Figure 5.12 Application of PDA nanoparticles in various commercial hair and skin products (Figure 5.11) applied onto pigskin.

discussed in section 5.2.4. Due to the poor surface adherence of the materials, an alternative, proof-of-concept application method was investigated. Dopamine HCl (DA) was mixed with a soap solution to induce *in situ* polymerization of the monomer in a submerged skin section (Figure 5.13). Pigskin was cut into squares and placed into the wells of a 24-well culture plate. They were submerged in a solution of DA in Milli-Q water with or without the addition of a basic soap (Sparkleen laboratory detergent, Fisher Scientific) (~ pH 8.5). Soap was chosen as a catalyst for the reaction because it is a common household item that does not generally cause skin irritation, and it is possible to envision a "wash-off" self-tanning product which can be used while bathing.

The well plate was placed into a typical cell culture incubator at 37°C and left to polymerize, checking the tissue every hour. Skin sections were removed, blotted dry with a clean filter paper, and placed on a white paper sheet for photographing. DA in the absence of soap produced a dark colored tissue which increased in color with the addition of soap.
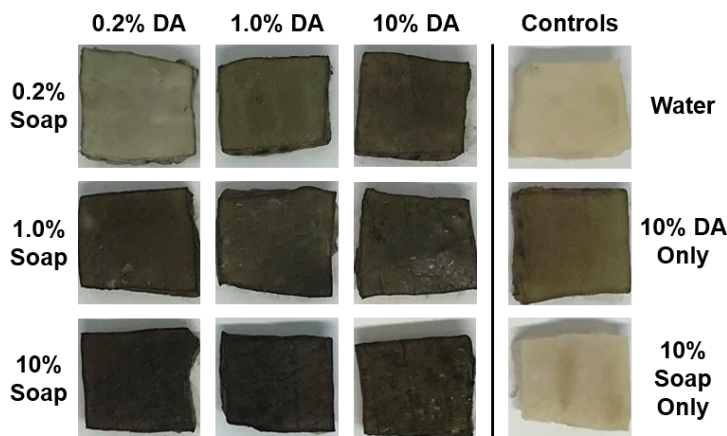
Figure 5.13 Pigskin treated for 3 h with PDA using *in situ* polymerization of dopamine HCl in a soap solution.

As little as 0.2% soap produced a very dark color, which increased with increasing concentration. Neither the water-only or soap-only conditions produced a color change. Although this drastic, visible color change is on a timescale which does not reflect that of a useful household product, nor is the extreme difference before and after application a cosmetically desirable outcome, it is nevertheless a valid proof-of-concept that an *in situ* polymerization approach may be beneficial with additional optimization. This experiment was repeated using human skin explants to verify the results and surprisingly the outcome was very different (Figure 5.14). The human skin was soaked in the same manner as the pigskin, with 10% soap, 10% DA, or 10% of a mixture of both, and placed in the cell incubator at 37 °C for 2 or 3 h. The color change was much lighter than expected, with an even, subtle tanning achieved at 3 h using DA only, and a darker, more gray color with the addition of soap.

Figure 5.14 Human skin treated for 2-3 h with PDA using *in situ* polymerization of dopamine HCl in a soap solution.

Further studies are needed to optimize the conditions necessary for a subtle, warm-toned color (less gray), and much faster reaction time. However, upon optimization, it is feasible that this system could generate a new method for approaching artificial tanning by applying chemistry not currently used in commercial products. What follows then is a question of whether a solution of DA is safe for application onto human skin. Currently, a clinical trial, pending IRB approval, for the testing of these materials on human subjects is forthcoming, and experiments will soon reveal whether irritation of the skin follows from the application of DA, PDA, and other artificial melanins.

5.2.3 3D Human Skin Equivalents (HSE) for UV-Protection

We explored a slightly more complex Human Skin Equivalent (HSE) 3D culture model for assessing whether melanin mimics could protect the tissue from UVA radiation. In this model, keratinocytes are seeded onto mouse fibroblast-seeded collagen plugs, where they fully differentiate into epidermal equivalents, resulting in thicker cultures which are easier to section.[183] J23T3 fibroblasts were mixed with a collagen solution and left to polymerize into a plug. After 48 h, NHEK were seeded to confluence and the media changed 24 h later. Another 24 h later, the cultures were "lifted" to the air interface by transferring them onto gridded dishes. After 9-10 days

of incubation at 37 °C, the cultures were fully differentiated. They were then treated with 150 μL of 1.0 mg/mL AMNP-1 melanin nanoparticles in water. The suspension was left on the tissue for 1 h and then the tissue was irradiated with a 365 nm UV lamp for 50 minutes to provide a dose of 13.5 J/cm^2 (irradiance= 4.5 mW/cm^2). The tissues were immediately fixed in 10% neutral buffered formalin. They were then paraffin-embedded, sectioned, and stained with phospho-histone H2AX (Ser139) rabbit monoclonal primary antibody followed by Alexa Fluor 647-conjugated IgG secondary antibody staining and DAPI to stain the nucleus. Phosphorylation of histone H2AX (pH2AX) is a rapid response to radiation and other causes of DNA damage resulting from double strand DNA breaks, and is a common marker used to assess DNA damage. AMNP-1-treated and vehicle-treated control (VTC) cultures were exposed to UV or no UV and then the pH2AX signal quantified using ImageJ (Figure 5.15).
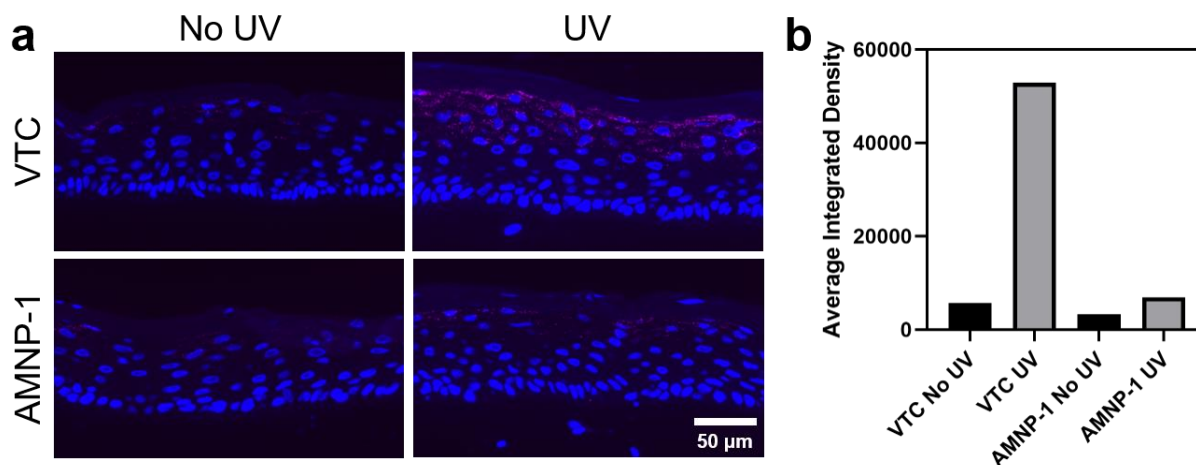
Figure 5.15 Staining and quantification of DNA damage in AMNP-1-treated 3D HSE cultures after UV irradiation based on phosphorylated H2AX signal. (a) Fluorescence micrographs of cultures with and without UV and with and without 0.15 mg AMNP-1 treatment. The stratum corneum is oriented above the tissue. (b) Average integrated density (product of area and mean gray value) of pH2AX signal.

Fluorescence micrographs, with DAPI-stained nuclei (blue) and pH2AX signal (magenta), show that there is a much higher pH2AX signal in the UV-irradiated control, and all other experimental conditions have low pH2AX signal (Figure 5.15a). For quantification measurements, single-channel pH2AX images (magenta) were thresholded and then the region of interest (ROI) selection was applied to non-thresholded images. The product of the area and the mean gray value (integrated density) of the pH2AX signal was averaged over the number of images (approximately 20 for each condition), and the values plotted for each experimental condition (Figure 5.15b). The results indicate that AMNP-1 are effective at protecting HSEs from UV-induced DNA damage. However, the expected result is that an overwhelming amount of the DNA double strand breaks occur in the nuclei, not the cytoplasm, therefore there should be colocalization of the DAPI and pH2AX signals. This is not the case in this experiment, as shown in the representative images in Figure 5.15a which show pH2AX signal throughout the cell cytoplasm. This pattern was also consistent for all other images acquired during the experiment. The pH2AX is punctate, as expected, but the location of the signal is unexpected. Therefore, this more investigation is needed to determine the reasoning behind this staining pattern, perhaps whether mitochondrial DNA plays a role or not, and if these results can be reasonably interpreted to imply that AMNP-1 can indeed protect HSE from DNA damage caused by UV radiation.

5.2.4 Human Skin Explant Studies for UV-Protection

Preliminary experiments with 3D cultures appeared promising, but the results were ultimately inconclusive. Therefore, additional UV irradiation studies were performed to assess the protective properties of topically applied melanin nanoparticles on intact human skin. Skin was obtained from the Skin Tissue Engineering and Morphology Core of the Feinberg School of

Medicine directly from an abdominoplasty patient at Northwestern Memorial Hospital and processed the same day. Skin was processed in the workflow illustrate in Figure 5.16. A 12 mm disposable biopsy punch was used to cut and mark circular punches from the skin, which were then released from the underlying fat using a pair of scissors.
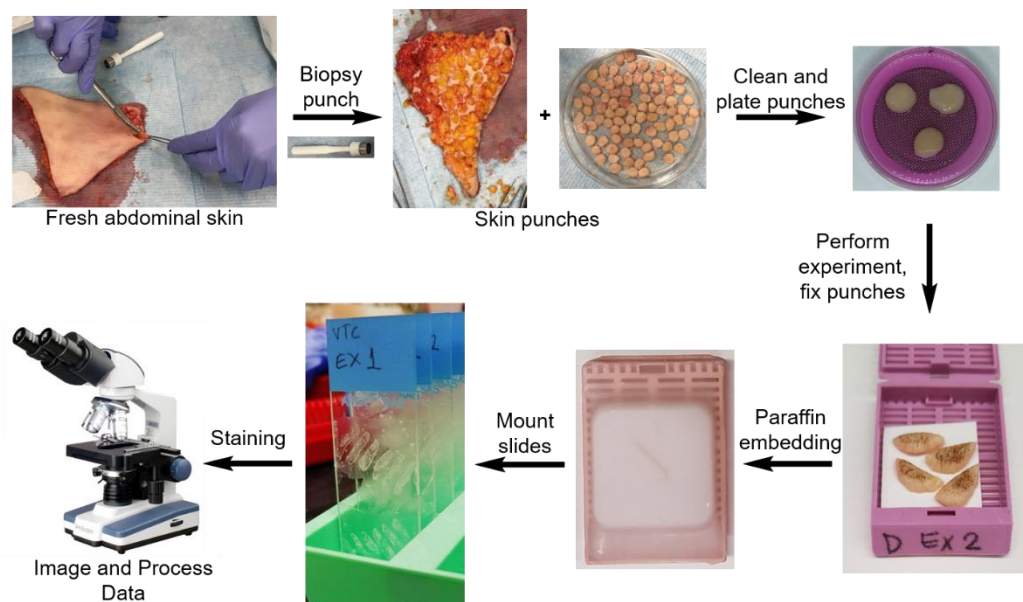
Figure 5.16 Workflow of human skin explant processing. The skin is obtained, punched, and cleaned before the experiment. Following the experiment, it is fixed, embedded in paraffin, mounted onto slides, stained, imaged, and the images quantified.

The punches were cleaned by dipping them quickly in diluted Betadine iodine solution in phosphate buffered saline (PBS) to sanitize the skin. Clean punches were then plated onto a metal grid placed on a plastic culture dish containing media. After experimental treatment, the punches were either placed into an incubator at 37 °C or processed immediately. The skin was bisected using a clean razor blade and placed into a tissue cassette and fixed in 10% neutral buffered formalin. The fixed tissue was embedded in paraffin, sectioned to 4 μm thick, and mounted on slides. The slides were stained for markers of interest before imaging.

To assess adhesion and penetration of the materials onto the skin prior to UV irradiation studies, skin punches were first tape-stripped, or not, and then treated with or without melanin in an Aquaphor® vehicle, which is a petroleum-based jelly (Figure 5.17).
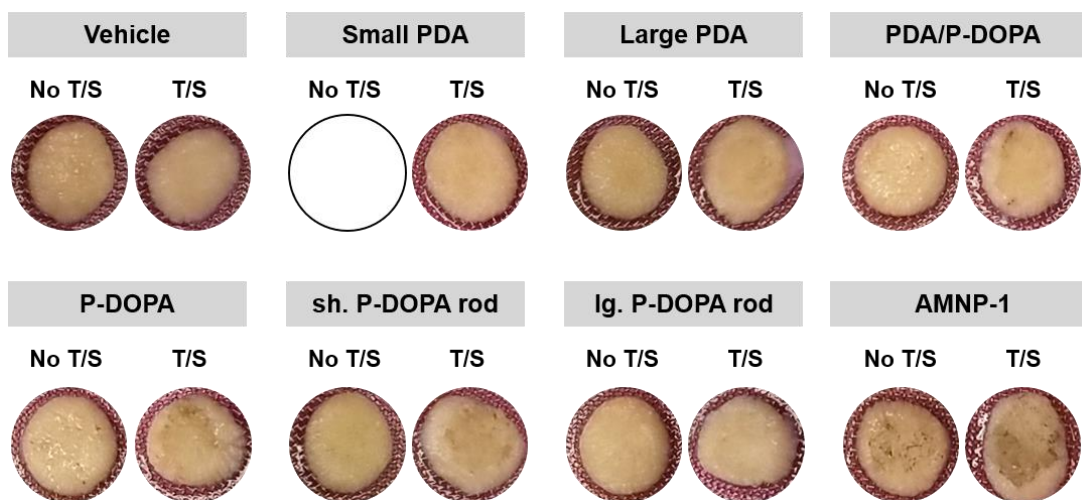
Figure 5.17 Screening melanin library for adhesion to human skin. Skin punches were plated on gridded dished containing cell media. A mixture of 25 μg of melanin nanoparticles in 20 μL of Aquaphor® was applied to the surface of the skin and the treated punches left to incubate at 37°C for 72 h, covered in Parafilm®. The Parafilm® and melanin mixture was peeled off before photographing. Small PDA T/S is missing due to a fungal infection. T/S = tape-stripped.

Tape-stripping is an exfoliation technique whereby a generic clear tape is used to remove loosely associated corneocytes from the stratum corneum. This was performed by adhering the tape to the dry skin and then removing, and it was performed 10 times for each tape-stripped skin punch, with the objective of providing a more advantageous surface for material adhesion. A mixture of 25 μg of melanin nanoparticles in 20 μL of Aquaphor® was applied to the surface of the skin and the treated punches left to incubate at 37°C for 72 h, covered in Parafilm®. The Parafilm® and melanin mixture was peeled off before photographing. Very little adhesion was observed on the surface of the skin, however the sections were fixed, embedded, sectioned, and stained for microscopic analysis.
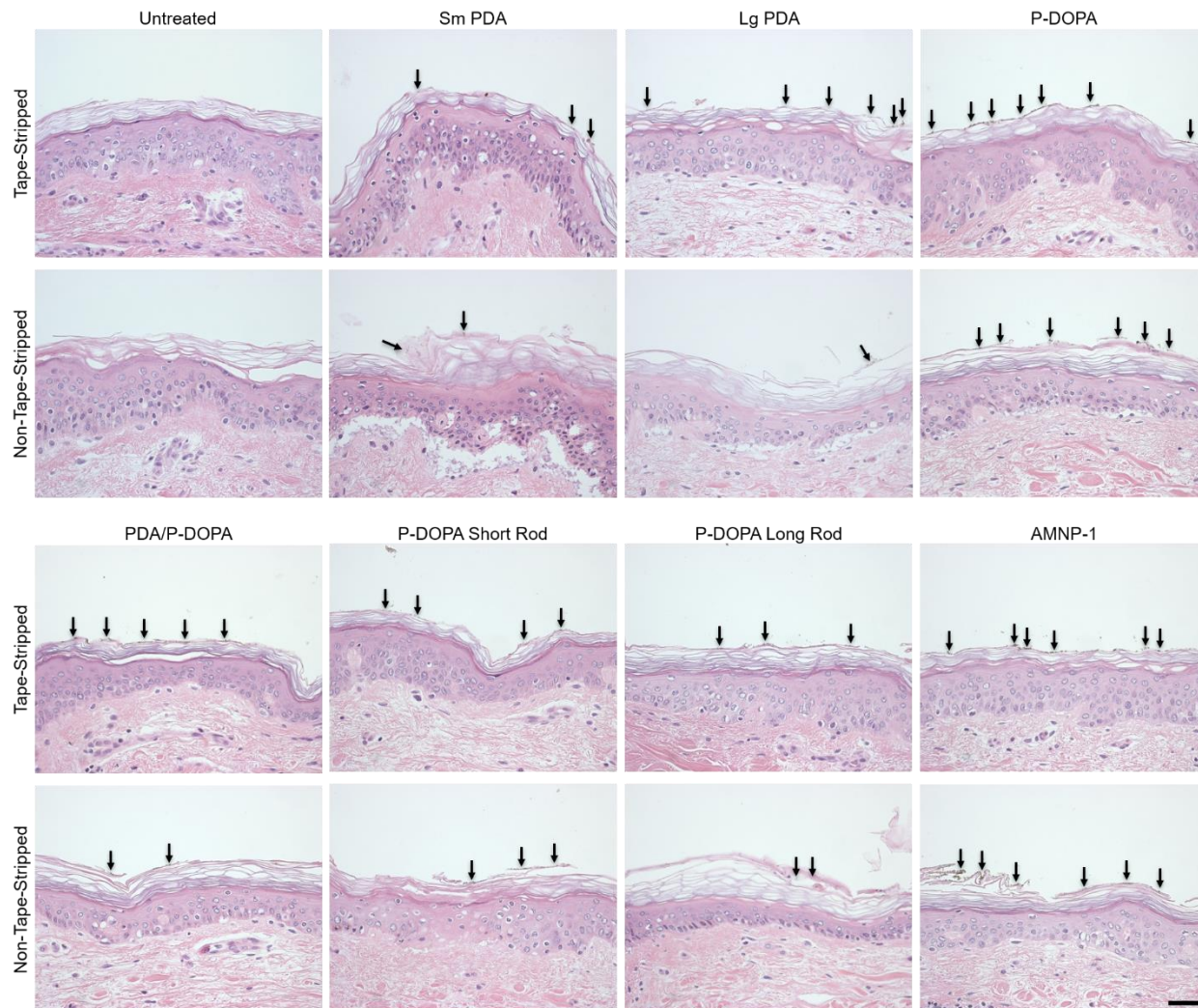
Figure 5.18 H&E stained tissue sections with or without melanin treatment, and with or without tape-stripping. Particles aggregate on the surface of the skin, visible as brown spots, indicated by black arrows. Scale bars 25 μm.

Tissue sections were stained with hematoxylin and eosin (H&E), which is a common histologic staining technique employed to visualize tissue substructures. Hematoxylin is a basophilic dye that stains basic structures such as nuclei blue, and eosin, an acidophilic dye that stains acidic components such as the extracellular matrix (ECM), cytoplasm, and stratum corneum pink. Light micrographs show that melanin-treated skin contains a thin, uneven layer of aggregated nanoparticle material on the surface of the stratum corneum, visible as a collection of small, brown
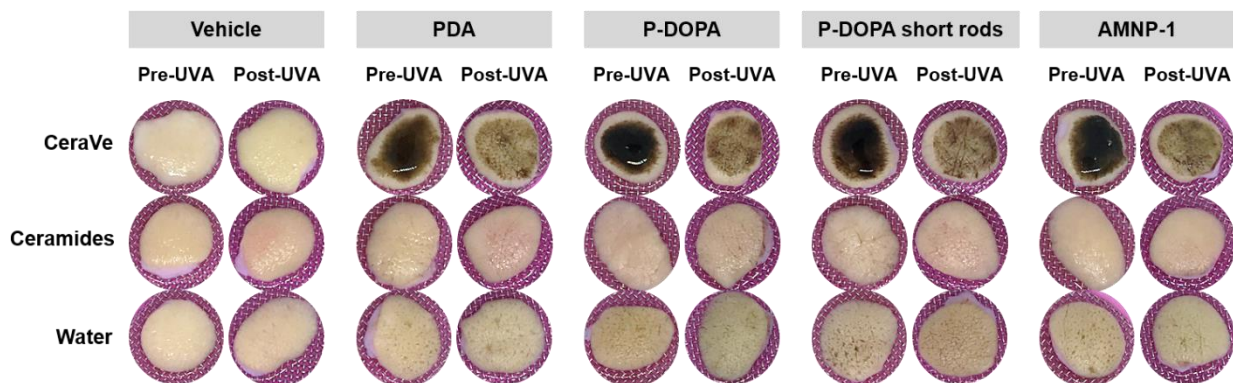
Figure 5.19 Human skin explant punches treated with four different melanins at 2 mg/mL in water, CeraVe,® or a ceramide solution. DS= P-DOPA sphere, A= AMNP-1, DR= P-DOPA short rod, and PDA= polydopamine.

spots (Figure 5.18). From these images, there is no evidence of penetration into underlying tissue layers. It cannot be ruled out completely that individual particles may have penetrated at least one layer of corneocytes, but it is not likely. Penetration of a healthy, intact stratum corneum with an organic nanomaterial of this size is not expected given the size of the particles (~200 nm) and the largely impenetrable nature of the stratum corneum. Due to the poor adhesion of these particles using Aquaphor®, we tested several different, alternative vehicles, including CeraVe® (a light lotion), water, and the same "ceramide complex" (ceramides) used for the pigskin screening in section 5.2.2 (Figure 5.19). Several different melanin particles were suspended at 2 mg/mL in one of the three vehicles and then applied to the explants before exposing them to UV radiation. Both water and ceramides have very low viscosity and were sprayed on the skin using an airbrush device. CeraVe® was too thick to be sprayed on, so it was applied by spreading on with a pipette tip. CeraVe® produced the most pronounced visual effect on the color of the skin, offering the thickest, most even coating of melanin material, and was therefore chosen for further analysis. Explants were subjected to 13.5 J/cm^2 (irradiance= 4.5 mW/cm^2) of 365 nm light and fixed immediately.
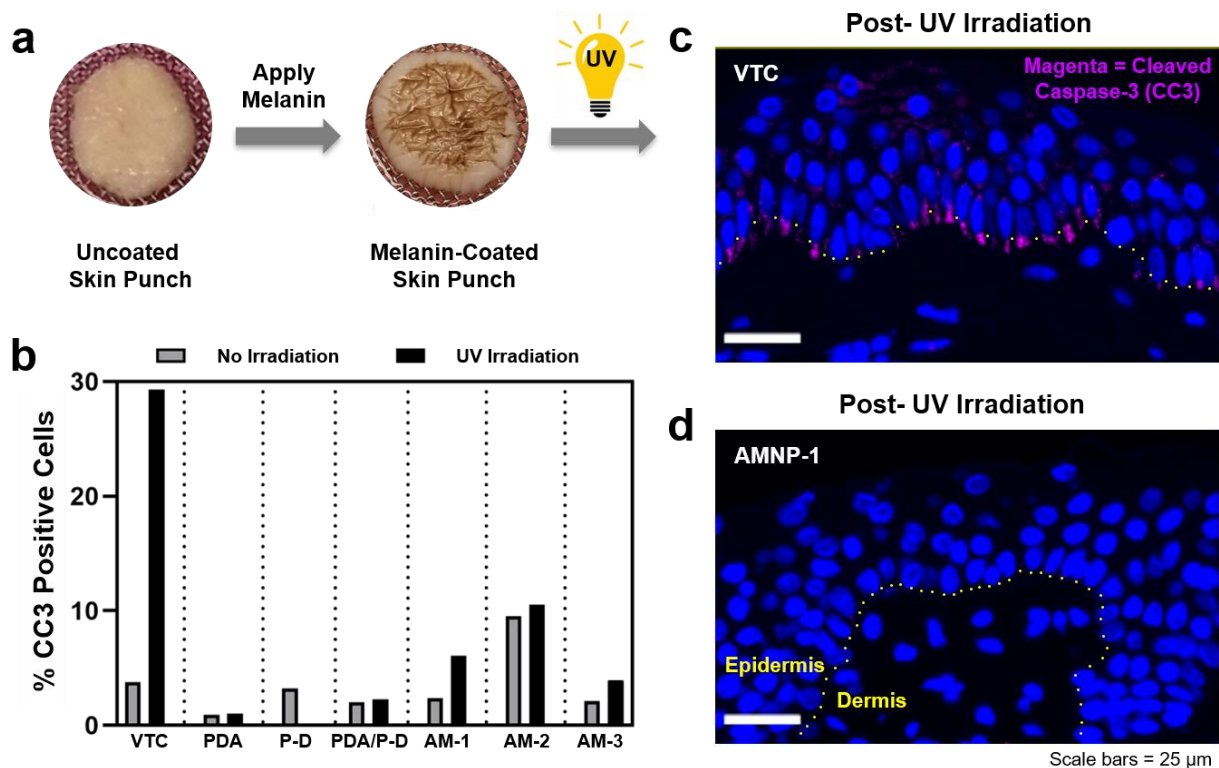
Figure 5.20 Expression of cleaved caspase-3 (CC3) following a 13.5 J/cm^2 dose of 365 nm UV irradiation in human skin explants treated with melanin. (a) Schematic of experimental workflow showing a representative photograph of a skin punch treated with AMNP-1. (b) Percentage of CC3 positive cells from melanin- or vehicle-treated skin punches, with or without exposure to UV radiation. (c,d) Fluorescent micrographs of 4 μm thick tissue sections, immunostained for CC3 (magenta), and the nuclei stained with DAPI (blue), following treatment with the vehicle (c) or AMNP-1 (d) prior to UV exposure. Dermal-epidermal junction demarcated with a dotted yellow line.

The tissue was embedded in paraffin, sectioned, and then immunostained for cleaved caspase-3 (CC3), a marker of apoptosis. The images were analyzed using ImageJ by counting the number of CC3 positive cells in the basal layer of the epidermis (stratum basale), which contains the most active cell population, as a percentage of total cells in the stratum basale (Figure 5.20). Nuclei were stained with DAPI and the images as a reference point to determine the CC3 signal from each cell. Hand counting each cell is the most laborious method for quantifying CC3 expression, but it is the most accurate. The results reveal that all melanin materials were effective at suppressing

CC3 expression after UV radiation, as compared to the vehicle-treated control (VTC). The VTC contained approximately 4% CC3 positive cells prior to irradiation, and 29% positive CC3 cells after irradiation. By contrast, even the worst performing melanin (AMNP-3) only saw an 11% positive signal, and it was only 1% higher than the pre-irradiation treatment, which indicated that some amount of damage to the skin was conferred by the particles alone, but the signal was still low enough that it may be statistically insignificant, pending biological repeats. All other melanin particles saw a minimal increase in CC3 expression after irradiation, demonstrating their effectiveness as UV radiation protection agents.

To streamline the process of image analysis, we attempted to automate the counting of positive keratinocytes in the stratum basale using MATLAB. Fluorescence images from stained tissue sections were analyzed by using a series of transformations to locate and isolate the CC3 signal overlapping with the stratum basale in a several step sequence (Figure 5.21). First, montage images of the DAPI and CC3 channels were converted to 8-bit grayscale images and cropped to appropriate dimensions (Figure 5.21-1). Next, intensity distribution of the DAPI channel was binarized by setting all pixel values $I \geq 1$ as 1, and $I = 0$ as 0 (Figure 5.21-2). The resulting binarized map reveals the global signal distribution from the epidermis across the map. To segment the epidermis from the entire map, the global signal map was further thresholded using the *"Otsu"* method and the connected components within the largest area (epidermis) were extracted (Figure 5.21-3). This resulted in a binary map of the isolated epidermis. To identify the stratum basale, the basal layer boundary was traced along this binary map (Figure 5.21-4), and then it was segmented from the rest of the epidermis (Figure 5.21-5). To avoid strict conditions to identify the positive skin cells based solely on 1-pixel lateral margins within the stratum basale, this segmented layer
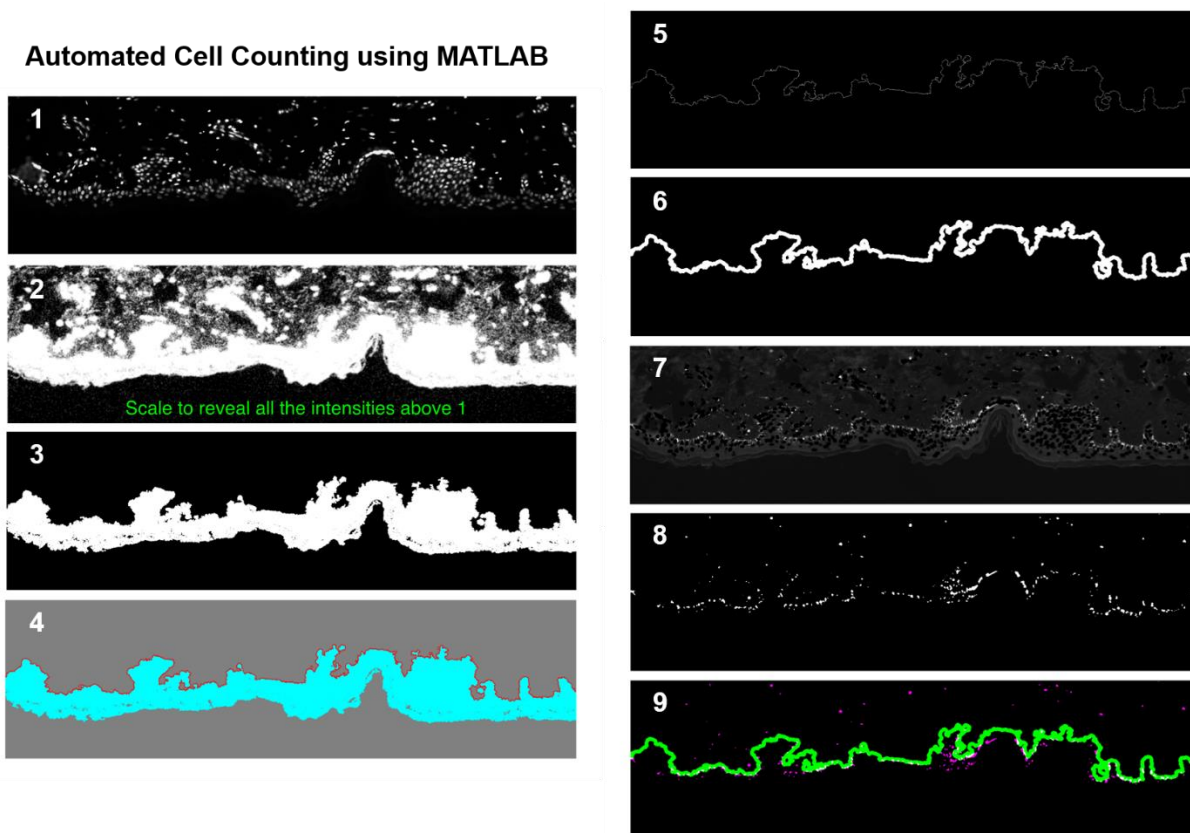
Figure 5.21 Workflow of MATLAB tissue analysis in 9 steps. (1) Cropped grayscale image. (2) Binarization. (3) Segmentation of the epidermis. (4) Tracing of the stratum basale. (5) Segmentation of the stratum basale. (6) Dilation of the stratum basale. (7) Subtraction of DAPI channel from CC3 channel. (8) Segmentation of the CC3 channel intensity. (9) Overlay of the segmented CC3 signal with the dilated stratum basale.

was dilated by 15 pixels laterally (Figure 5.21-6). To identify positive skin cells in the stratum

basale, the overall intensity distribution of the DAPI channel was subtracted from the intensity

distribution of the CC3 channel (Figure 5.21-7). The subtracted intensity distribution of the CC3

channel was binarized by *"Otsu"* thresholding, and further noise from the thresholded image was

removed by morphological operations. This results in a binarized map containing only the CC3

positive signal (Figure 5.21-8). This binarized map was then overlaid onto the map of the dilated

stratum basale to identify positive cells (Figure 5.21-9). By extracting the overlapping intensity

distribution, we quantified the ratio of positivity. Next, a blinded sample data set was obtained

from Prof. Bethany Perez-White in the dermatology department at Northwestern Feinberg School of Medicine containing a series of skin sections stained for CC3 following UV irradiation by a UV lamp (LAMP) or a UV delivery device designed to limit exposure (MN). This data was obtained manually by counting cells with positive staining for CC3. The raw data from this sample set was then processed using our MATLAB sequence to verify if the counting process could accurately predict results matched to results obtained by hand counting (Figure 5.22). Results were promising, indicating that the automated process using MATLAB produces data with similar trends to those seen in the hand-counted data, however the larger error prevented statistical significance.
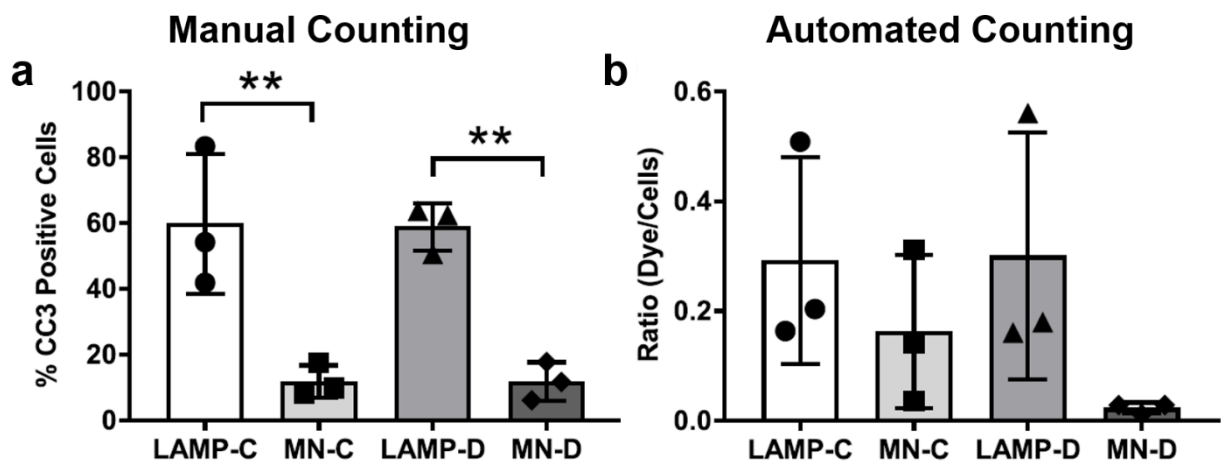
Figure 5.22 Comparison of manual counting vs MATLAB automated counting for cleaved caspase-3 (CC3) data acquisition. (a) Results from manual counting for CC3 positivity in human skin tissue following direct exposure to a UVA lamp (LAMP) or a UV delivery device designed to limit toxic exposure (MN). Statistics were performed using one-way ANOVA followed by Dunnett's multiple comparisons post-test. **, $P \leq 0.0056$. (b) Results from MATLAB-based data acquisition. Manual counting data courtesy of Bethany Perez-White.

It is possible that one or more parameters can be altered to decrease the error associated with this analysis. For example, increasing the pixel size of the stratum basale dilation may increase the signal, but it may also introduce additional error from non-specific staining. Therefore, it is essential to use images with good signal to noise ratios and little background signal. These results

suggest that further optimization is needed for this analysis to be widely applicable, but there is potential for a user friendly method for counting basal epidermal cells that could be accessible to many researchers, pending further optimization.

5.2.5 *In Vivo* Testing of Antioxidant Properties of Melanin

In parallel studies to the development of melanin applications for human skin, there is also a clinical path to the utilization of melanin and other melanin-like materials for skin protection after burns and high energy radiation. We anticipate that these studies form an early, preclinical path toward an FDA route for translation, which necessitates the use of animal testing. In collaboration with Kurt Lu and his colleagues at the Northwestern Feinberg School of Medicine Department of Dermatology, key preliminary studies using mouse models of radiation burns and chemical injury point to a potentially promising future for melanin-based materials as treatments for skin injury.

Based on the photoprotective and ROS quenching properties of melanin in the skin, we hypothesized that PDA-based eumelanin mimics could also ameliorate the inflammatory response after chemical skin injury. We utilized a mouse nitrogen mustard (NM)–induced injury model. NM is a vesicating agent closely related to sulfur mustard, an infamous WWI chemical weapon. Exposure to NM leads to irreversible DNA alkylation followed by cell death in affected tissues, and is characterized by blistering, inflammation and edema. Despite extensive research, currently there is no effective treatment for victims of alkylating-chemical attacks.

C57BL/6J female mice were subjected to NM and treated with PDA NPs two hours after injury induction, and then 24 and 48 hours later (Figure 23). In general, treatment with NM lead to significant skin injury, as was evidenced by skin swelling, necrosis and development of a
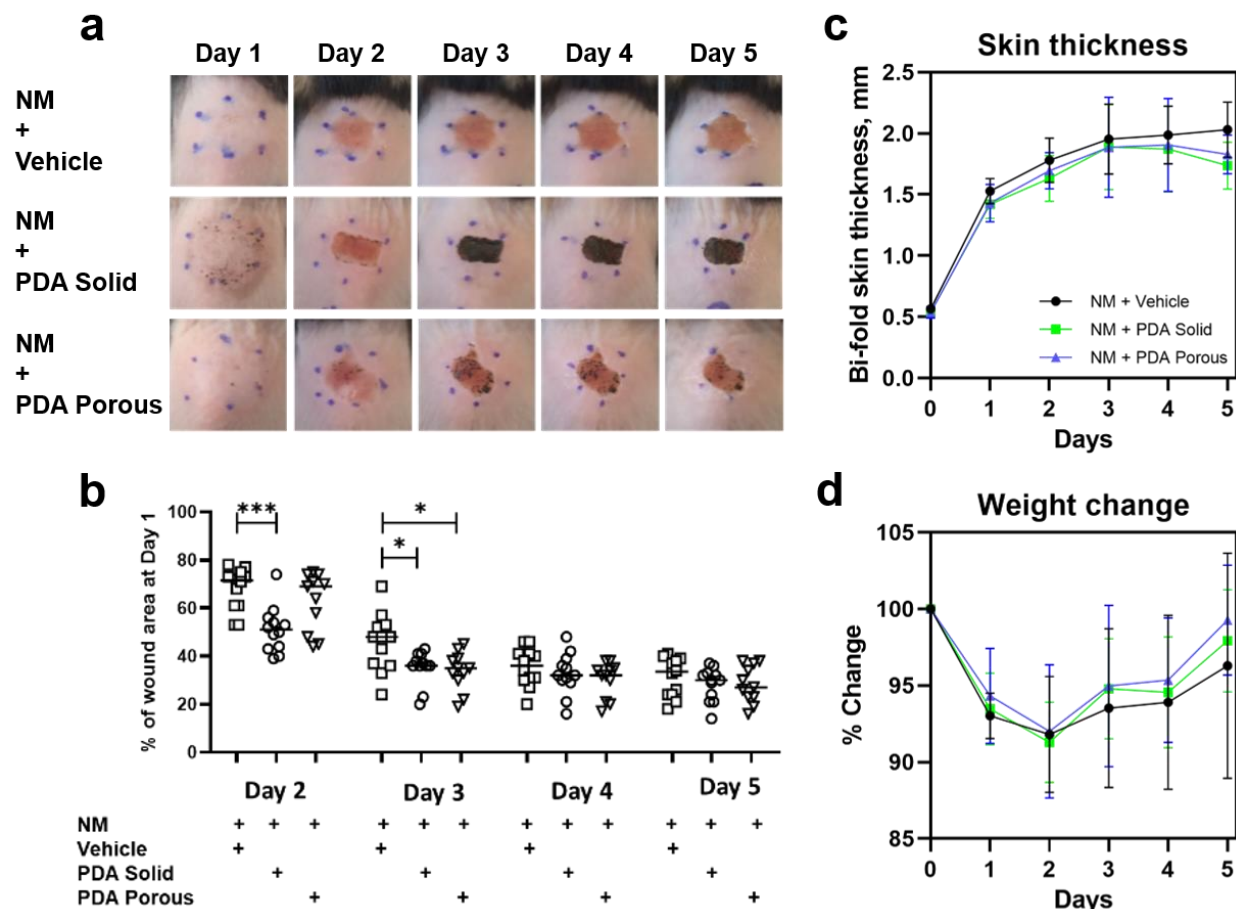
Figure 5.23 Treatment with PDA NP improves skin wound healing after NM-induced injury. (a) Representative wound images. (b) Reduced wound area. (c) Increase in bi-fold skin thickness after NM exposure. (d) Weight change after NM exposure (n=11-12, * p<0.05; *** p<0.001). Data courtesy of Kurt Lu, Dauren Biyashev, and Venus Onay.

hemorrhagic crust (Figure 5.23a). Wound area measurements were used to quantify skin healing.

Compared to the vehicle treated group, treatment with PDA NPs resulted in significant reduction

of initial wound area at days 2 and 3 post injury (Figure 5.23b). The effect of Porous NPs[45] was

delayed at day 2, but reached statistical significance at day 3. PDA NPs also appeared to decrease

skin swelling and counteract the weight loss following NM (Figure 5.23c,d), though the data were

not statistically significant.
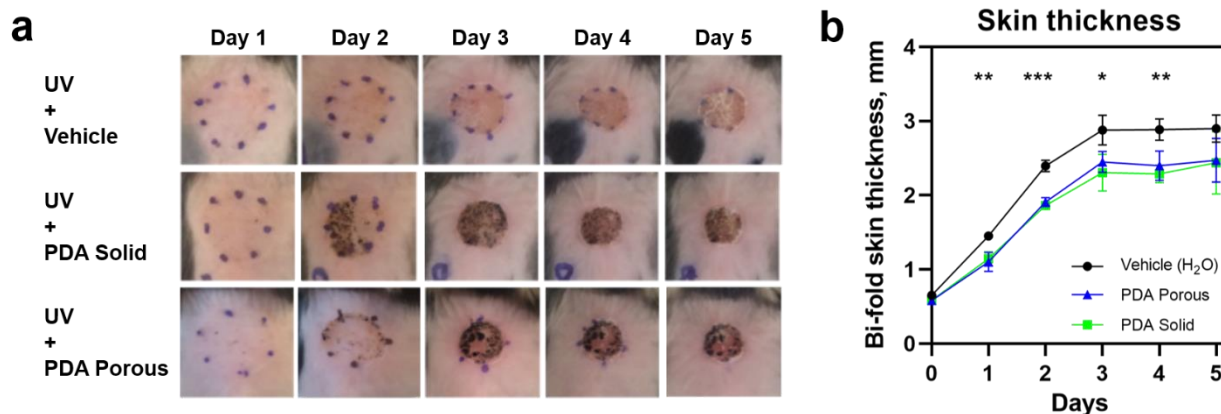
Figure 5.24 Treatment with PDA NP improves skin wound healing after UV-induced injury. (a) Representative wound images. (b) Increase in bi-fold skin thickness after NM exposure; (n=4-5, * $p<0.05$; ** $p<0.005$; *** $p<0.0005$). Data courtesy of Kurt Lu, Dauren Biyashev, and Venus Onay.

To confirm that the observed effect was not due to the potential adsorption of residual NM, we utilized UV-induced injury model in which animals were treated with PDA NPs after exposure to 100 mJ/cm^2 UV radiation (Figure 24). This dose of UV is sufficient to induce a significant sunburn (Figure 5.25a). Similarly, the PDA NP-treated animals showed significantly decreased inflammatory response as evidenced by the bi-fold skin thickness measurements at days 1-4 post injury (Figure 5.24b).

These promising, initial NM and UV studies led us to consider the possible mechanisms of melanin protection. Transcription factor Nrf2 (NF-E2 p45-related factor 2) is a key element that coordinates stress-inducible activation of an array of cytoprotective genes. It regulates the expression of phase I and phase II detoxifying enzymes, heme metabolism and components of glutathione and thioredoxin antioxidant systems. Therefore, NRF2 is a crucial element of the oxidative stress defense, and is itself regulated by reactive oxygen species (ROS). We hypothesized that topical PDA NP treatment regulates NRF2 activity and expression levels of its downstream targets. In preliminary experiments we found that in NM-treated animals, a single

application of PDA NPs downregulated expression of several oxidative stress-induced genes, such as Hmo1, Nqo1, Idh1, and Gsr1. Though only in the case of Gsr1 the data reached the level of significance (n≥4 mice per group, $p<0.05$), all of them show a clear trend. In addition, in NM-injured skin, PDA NPs also downregulated the p53 pathway, which is known to be activated by ROS.

Overall, this promising preliminary data suggest that the anti-inflammatory effects of PDA NPs can be attributed to the reduction of overall ROS burden and demonstrate that topical application of PDA NPs post injury improves skin wound healing and has therapeutic potential.

5.3 Conclusion

Through the use of epidermal models of varying complexity, including monolayer cell culture, 3D cultures, pig skin, human skin, and mice, we tested a variety of artificial melanins as tanning agents, and for their use in protection against radiation and toxin insult. Synthetic melanins are internalized in much the same manner as endogenous melanin, where they form perinuclear caps. This can be monitored over time, evident as a darkening of the cell cultures, which leads to a tanned appearance. Although the materials are readily taken up by monolayer, undifferentiated keratinocytes, they do not penetrate more elaborate, differentiated structures such as 3D human epidermal equivalents or skin equivalents. Rather, they sit on top of the tissue as a layer of brown material. This treatment results in a significant darkening of 3D model tissues, but does not translate when tested on pig skin. The coloration is light, and the coverage patchy. To improve the visual appearance and adherence, a vehicle screen was performed, using several commercial skin and hair products, which provide vastly different color tones depending on the vehicle used. To achieve an even color, *in situ* polymerization of dopamine was also performed, and showed that a

significant darkening could be achieved in pig skin, which was more subtle, albeit more natural looking, in human skin.

To assess the protection aspects of our synthetic melanins, we quantified the amount of DNA damage in 3D human skin equivalents after UVA irradiation. These results seemed promising, but more studies and biomarkers will need to be tested in the future. Intact human skin was then investigated by applying several different melanin materials in a light lotion, which provided even, thick coverage on the skin. The skin was irradiated with UVA light, and then a marker of apoptosis, cleaved caspase-3 (CC3), was quantified to determine the amount of protection afforded by our materials. The results indicated a large increase in the CC3 signal for vehicle-treated, irradiated skin, but not the non-irradiated control, or any of the melanin-treated skin samples, confirming that synthetic melanin can protect intact, human skin from UV irradiation. Lastly, we tested the effects of melanin for mitigating skin damage following nitrogen mustard (NM) and UV exposure in mice. Melanin treatment resulted in significant reduction of initial wound area at days 2 and 3 post injury and appeared to decrease skin swelling and counteract the weight loss following NM. Melanin treatment after UV injury also provided a significantly decreased inflammatory response as evidenced by the bi-fold skin thickness measurements post-injury.

Altogether, these results point to melanin as a promising, biocompatible material for preventing UV damage, for the treatment of skin injury following UV or NM exposure, and as a possible cosmetic for artificial tanning. Future studies will repeat these experiments, and thoroughly investigate the mechanisms by which different synthetic melanins can both prevent and treat skin injury, and improve upon formulations which retain optimal skin adherence and

spreading. By mimicking a natural material which is already used by nature to protect a wide variety of organisms, we hope to add additional function, and to apply these synthetic melanin analogues to human systems.

5.4 Experimental Details

Uptake of melanin in NHEK over time was obtained using a BioTek Lionheart FX automated microscope with 20x objective. For human skin experiments, H&E tissue sections were imaged on a Zeiss Axioplan 2 microscope system (Carl Zeiss). AxioVision software (Carl Zeiss, Germany) was used to acquire and analyze the images. Immunofluorescence images were acquired using a Zeiss AxioImager Z.1 microscope with ApoTome and a high resolution AxioCam MRm digital camera (Carl Zeiss, Germany). Image analysis was performed with Zeiss AxioVision software. UV irradiation studies were performed using a handheld UVP (now Analytik Jena US) UVL-26 EL Series 6 watt, 365 nm UV lamp.

5.4.1 Monolayer Cell Culture

Primary neonatal epidermal keratinocyte (NHEK) cells were isolated from freshly excised neonatal foreskins and gifted by the Perez-White lab at Northwestern Feinberg School of Medicine. Tissue was collected under a protocol approved by the Northwestern University Institutional Review Board (IRB# STU00009443). Patients' consent for neonatal foreskin tissue (for primary keratinocyte isolation) were not required as these tissues are de-identified and considered discarded material per IRB policy. To isolate the cells, the tissue was treated overnight with dispase and then incubated with 0.25% trypsin with 1 mM EDTA for 10 min at 37 °C. The trypsin was neutralized with fetal bovine serum (FBS), the cells suspended in phosphate buffered saline (PBS),

filtered through a 40 μm sieve, and then centrifuged at 1,000 rpm for 5 minutes. The cell pellets were resuspended in, and subsequently maintained in, M154 medium supplemented with human keratinocyte growth supplement (HKGS), 10 μg/mL gentamicin, 0.25 μg/mL amphotericin B, and 0.07 mM $CaCl_2$, and maintained at 37 °C with 5% CO_2.

5.4.2 3D Cultures (HEE and HSE)

Human Epidermal Equivalents (HEE). HEE were formed by the following set of steps developed in the laboratory of Bethany Perez-White at Northwestern Feinberg School of Medicine Department of Dermatology: 1.) Culture primary epidermal keratinocytes in CnT-Prime Epithelial Culture Medium (CnT-PR, CELLnTEC, Bern, Switzerland) 2.) Day -3: Plate 3.6e5 keratinocytes in 500 µL CnT-PR in the upper chamber of a 12-well polyester transwell culture dish with pore membrane size 0.4 µm (3460, Corning Life Sciences, Glendale, Arizona, USA). Add 1 mL CnT-PR to the lower chamber. 3.) Day -2: Change media in the upper chamber, 500 µL CnT-PR 4.) Day -1, late in the day: Change media in the upper (500 µL) and lower (1 mL) chambers with CnT-Prime 3D Barrier Media for 3D Epidermal Models (CnT-PR-3D, CELLnTEC). 5.) Day 0, early in the day: Culture cells at the air-liquid interface by removing media from the upper and lower chambers, then adding 300 µL CnT-PR-3D to the upper chamber only. 6.) Days 1- 10: Change media every day, 300 µL in the bottom chamber only. 7.) Day 11: Treat with NP. 8.) Harvest sample by fixing in 10% neutral-buffered formalin.

Human Skin Equivalents (HSE). 3D epidermal equivalents (organotypic rafts) were prepared according to an established protocol, section 4.2 entitled, "3D Organotypic Raft Culture Protocol."[183] J23T3 mouse fibroblasts were trypsinized using 0.05% trypsin/1mM EDTA and inactivated with serum-containing media. Cells were counted to ensure 400,000 cells per culture.

They were resuspended in reconstitution buffer and diluted in DMEM. Collagen (rat tail collagen, Type I, Corning, cat. #354249) was added to a final concentration of 4 mg/mL and diluted in water as needed (depending on the amount of cells used). The mixture was pH adjusted using 0.5 M NaOH until reaching the color of a "watermelon Jolly Rancher." The mixture was pipetted onto the top chamber of a transwell (Corning cat. #355467) with 3 μm pore size insert (Corning, cat. #353091) and then incubated at 37 °C in a humidified incubator with 5% CO_2 for 20 minutes. 2 mL of DMEM with 10% FBS and pen/strep was added to the top chamber. 48 hours later, NHEK were seeded onto the collagen plug at 1.0e6 cells per plug in 2 mL E-Media supplemented with 5 ng/mL EGF. To the bottom chamber, 13 mL of the same E-Media with EGF was added. The media was changed 24 hours later. 24 h after the media change, the cultures were lifted to the air interface (day 0) and placed onto a custom metal grid on a culture dish. The media was changed every 2 days and the cultures allowed to proliferate at 37 °C in a humidified incubator with 5% CO_2 for 10 days.

Once the cultures were mature, the experiment was performed. 150 μL of 1.0 mg/mL AMNP-1 in water was carefully added to the top of the cultures, or water as the vehicle-treated control (VTC). This suspension was left to sit for 1 h. The tissues were then subjected to a 365 nm UV lamp for 50 minutes to achieve a dose of 13.5 J/cm^2. They were then immediately fixed in 10% neutral buffered formalin. This was followed by paraffin-embedding, sectioning to 4 μm thick, and then mounting on microscope slides. The night before staining, slides warmed on a warming plate at 65 °C overnight to melt the paraffin. The sections were de-paraffinized using xylenes followed by a series of graded ethanol solutions (5 min each at xylenes x3, then for 3 min each: ethanol at 100%, 100%, 95%, 70%, followed by Milli-Q water x2). Antigen retrieval was performed by

placing the slides in 10 mM citrate buffer (pH 6.0) in a plastic slide chamber, which was then placed in a water bath heated to 99 °C for 35 min. The slides were cooled slowly in a room temperature (RT) water bath over 1 h. Cool water was slowly added, and the slides were rinsed with tap water at RT and then exchanged into PBS. A region around the tissue sections on each slide was drawn with a hydrophobic PAP pen. The tissue was blocked with Dako protein block serum-free (Agilent X0909) for 25 minutes at RT. Phospho-Histone H2A.X (Ser139) (20E3) rabbit monoclonal antibody (Cell Signaling Technology #9718) was applied in a 1:50 dilution in wash buffer (0.3% Triton X-100 in 1x PBS) with 1% bovine serum albumin (BSA) heat shock fraction for 90 minutes at RT. The slides were rinsed 3 times for 5 min each in wash buffer. The secondary antibody (IgG, highly cross-adsorbed, donkey anti-rabbit coupled to Alexa Fluor 647) (Invitrogen) was then applied at a 1:300 dilution in wash buffer supplemented with 1% BSA for 45 min at RT. The slides were rinsed 3 times for 5 min each in wash buffer. Lastly, they were stained with 20:1 DAPI in PBS for 5 minutes at RT and then rinsed with slowly running DI water for 1 min. Coverslips were mounted onto the slides using a homemade Gelvatol mounting medium and left to harden overnight before imaging.

For image analysis, the raw, single channel pH2AX images were thresholded to 800 in ImageJ/FIJI, and the region of interest (ROI) was chosen and applied to the non-thresholded image. The Integrated Density ("IntDen") calculation was used to measure product of the area and the mean gray value, and then the total averaged over the number of images analyzed to get the average signal per image frame.

5.4.3 Human Skin Explants

Preparation and Maintenance of Human Skin Explants. Excised human skin was obtained from the Skin Tissue Engineering and Morphology Core of the Northwestern Feinberg School of Medicine following an abdominoplasty and prepared for experimentation within approximately 4-8 hours following surgery. Tissue was collected under a protocol approved by the Northwestern University Institutional Review Board (IRB# STU00009443). Patients' consent for human truncal skin (obtained from abdominoplasty) were not required as these tissues are de-identified and considered discarded material per IRB policy. The skin was prepared in one of two ways. The first method was to excise fat from the entire section of skin and then use a 12 mm biopsy punch to remove skin punches. The second method was to take the full thickness skin with attached fat layer and use a 12 mm biopsy punch to cut a circle into the skin, which was then removed from the fat layer with scissors. After either method, the punches were plated epidermal side up onto metal grids placed in culture dishes containing high glucose Dulbecco's Modified Eagle Medium (DMEM) supplemented with 10% FBS and 6x penicillin-streptomycin.

Explant Irradiation Studies. Nanoparticles stored in Milli-Q water were centrifuged at 10,000 rpm to remove most of the water. The pellets were re-suspended in the vehicles at a concentration of 2 mg/mL and mixed well using a pipette tip. Prior to application, skin punches were removed from their gridded dishes, set onto a piece of fresh filter paper using a pair of forceps, and the epidermal surface blotted gently with a fresh piece of filter paper. Immediately after application of the material, they were re-deposited onto the gridded dishes, with care not to disturb the epidermal coating. For experiments using thicker vehicles (CeraVe®), 40 μL of the particle suspension was applied and spread onto the skin using a large-orifice pipette tip. For experiments

involving thinner vehicles and the spraying technique, 2 mL (excess) of 2 mg/mL particles were loaded into the airbrush spray gun (Cool Runner II, Master Airbrush). The gun was set to a height of 14 cm using a metal clamp and the trigger mechanism depressed five times with one second pulses. Dishes containing treated skin punches were placed under a 365 nm UV lamp for 50 minutes to achieve a dose of 13.5 J/cm^2. Immediately following irradiation, they were either fixed immediately (in the case of the earlier timepoint) or put back into the incubator, to be fixed at a later timepoint. For the fixation process, punches were removed from their gridded dishes and gently blotted dry with a fresh piece of filter paper. Excess nanomaterial/vehicle on the epidermal surface of the punches was also gently blotted with fresh filter paper. The punches were placed onto a strip of dental wax and bisected using a fresh razor blade. Each half of a single punch was placed on a piece of fresh filter paper which was placed into a plastic cage. The cages were dropped into 10% neutral buffered formalin and left to sit for 48 hours. The skin was dehydrated through a graded series of ethanol solutions and then embedded in paraffin, sectioned to 4μm, and mounted onto microscope slides.

Immunostaining. Slides containing mounted, paraffin-embedded skin tissue sections were warmed on a warming plate at 65 °C overnight, the day before the staining protocol, to melt the paraffin. The sections were de-paraffinized using xylenes followed by a series of graded ethanol solutions (5 min each at xylenes x3, then for 3 min each: ethanol at 100%, 100%, 95%, 70%, followed by Milli-Q water x2). Antigen retrieval was performed by placing the slides in 10 mM citrate buffer (pH 6.0) in a plastic slide chamber, which was then placed in a water bath heated to 99 °C for 35 min. The slides were cooled slowly in a room temperature (RT) water bath over 1 h. Cool water was slowly added, and the slides were rinsed with tap water at RT and then exchanged

into PBS. A region around the tissue sections on each slide was drawn with a hydrophobic PAP pen. The tissue was blocked with Dako protein block serum-free (Agilent X0909) for 25 minutes at RT. Cleaved caspase-3 (Asp175) rabbit monoclonal antibody (Cell Signaling Technology #9664) was applied in a 1:50 dilution in wash buffer (0.3% Triton X-100 in 1x PBS) with 1% bovine serum albumin (BSA) heat shock fraction for 90 minutes at RT. The slides were rinsed 3 times for 5 min each in wash buffer. The secondary antibody (IgG, highly cross-adsorbed, donkey anti-rabbit coupled to Alexa Fluor 647) (Invitrogen) was then applied at a 1:300 dilution in wash buffer supplemented with 1% BSA for 45 min at RT. The slides were rinsed 3 times for 5 min each in wash buffer. Lastly, they were stained with 20:1 DAPI in PBS for 5 minutes at RT and then rinsed with slowly running DI water for 1 min. Coverslips were mounted onto the slides using a homemade Gelvatol mounting medium and left to harden overnight before imaging.

Fluorescence Imaging and Quantification. Sections were imaged using a Zeiss AxioImager Z.1 microscope. Multi-channel (DAPI and 647 channel for CC3) images were quantified using either ImageJ (FIJI), or MATLAB for the automated analysis. In ImageJ, cells were hand counted and the number of positive cells (magenta signal for CC3) at the basal layer of the epidermis were divided by the total number of cells at the basal layer. For the automated analysis, MATLAB was used in the following manner:

Automated Cell Counting Using MATLAB. Tissue sections were analyzed by using a series of transformations to locate and isolate the basal layer of epidermal cells in the following two steps:

Segmentation of the Stratum Basale: First, montage images of the DAPI and CC3 channels were converted to 8-bit grayscale images and cropped to appropriate dimensions. Next, intensity

distribution of the DAPI channel was binarized by setting all pixel values $I \geq 1$ as 1, and $I = 0$ as 0. The resulting binarized map reveals the global signal distribution from the epidermis across the map. To segment the epidermis from the entire map, the global signal map was further thresholded using the *"Otsu"* method and the connected components within the largest area (epidermis) were extracted. This resulted in a binary map of the isolated epidermis. To identify the stratum basale, the basal layer boundary was traced along this binary map, and then it was segmented from the rest of the epidermis. To avoid strict conditions to identify the positive skin cells only based on 1-pixel lateral margins within the stratum basale, this segmented layer was dilated by 15 pixels laterally.

Identifying Positive Cells in the Stratum Basale: To identify positive skin cells in the stratum basale, the overall intensity distribution of the DAPI channel was subtracted from the intensity distribution of the CC3 channel. The subtracted intensity distribution of the CC3 channel was binarized by *"Otsu"* thresholding, and further noise from the thresholded image was removed by morphological operations. This results in a binarized map containing only the CC3 positive signal. This binarized map was then overlaid onto the map of the dilated stratum basale to identify positive cells. By extracting the overlapping intensity distribution, we quantified the ratio of positivity.

5.4.4 Animal Studies

All animal studies were approved by the Northwestern University IACUC. Six to eight-week-old C57BL/6J female mice were purchased from Jackson Laboratories.

Nitrogen Mustard Skin Injury Model. The dorsal area of the mice was shaved and chemically depilated 48 hours before skin injury induction. Mice were anesthetized and placed on

a heat pad under a chemical fume hood. 0.5% of mechloroethamine hydrochloride (nitrogen mustard, NM) (Sigma, 122564) solution in 1.5% DMSO-PBS was prepared immediately before the application. Total of 40 µl of NM solution was applied to a circular (12 mm diameter) area in two consecutive applications. After application, the mice were placed in a temporary housing space under a chemical fume hood for two hours.

UV Radiation Skin Injury Model. Mice were exposed to UV radiation as described previously.[184] Briefly, a 12 mm diameter circular area of back skin depilated of hair was exposed to UVB irradiation from six FS-40 fluorescent lamps filtered through Kodacel (Eastman Kodak Co., Rochester, NY). UVB emission was measured with an IL-443 phototherapy radiometer (International Light, Newburyport, MA) furnished with an IL SED 240 detector. Mice were exposed to a single UVB dose of 100 mJ/cm^2 to induce skin inflammation.

Treatment with PDA NPs. PDA NPs (PDA Solid) were synthesized according to the protocol in section 4.2.1. Porous PDA NPs were synthesized according to our recent publication (5% loaded SPM).[45]

PDA NPs were diluted in Milli-Q water at concentration of 50 µg/µl. Total amount of 1 mg of particles were applied to the injured skin area two hours after the injury induction, and then 24 and 48 hours later. Milli-Q water was used as a vehicle in control groups. During the treatment mice were anesthetized using isoflurane.

Monitoring Skin Injury and Measurement of Wound Healing. Mice were followed up non-invasively after induction of skin injury. Monitoring was performed daily, starting at the day of skin injury. Photographs of the injured area were taken, the bi-fold skin thickness of the injured area was measured using digital calipers (Mitutoyo, PK0505CPX), and weight was measured. The

area of the inflammation/wound was measured using ImageJ and QuPath software. GraphPad Prism V.8.3.0 software (San Diego, CA) was used to create visual graphics and to calculate the statistical significance. One-way ANOVA and t-test were used to calculate the p-values.

References

1.   D'Alba, L.; Shawkey, M. D., Melanosomes: Biogenesis, Properties, and Evolution of an Ancient Organelle. *Physiol Rev* **2019,** *99* (1), 1-19.

2.   Maia, R.; Rubenstein, D. R.; Shawkey, M. D., Key ornamental innovations facilitate diversification in an avian radiation. *P Natl Acad Sci USA* **2013,** *110* (26), 10687-10692.

3.   Hong, L.; Simon, J. D., Current understanding of the binding sites, capacity, affinity, and biological significance of metals in melanin. *J Phys Chem B* **2007,** *111* (28), 7938-47.

4.   Goiran, C.; Bustamante, P.; Shine, R., Industrial Melanism in the Seasnake Emydocephalus annulatus. *Curr Biol* **2017,** *27* (16), 2510-2513.

5.   Price, R. J.; Lee, J. S., Paralytic Shellfish Poison and Melanin Distribution in Fractions of Toxic Butter Clam (Saxidomus-Giganteus) Siphon. *J Fish Res Board Can* **1972,** *29* (11), 1657-1658.

6.   Pacelli, C.; Bryan, R. A.; Onofri, S.; Selbmann, L.; Shuryak, I.; Dadachova, E., Melanin is effective in protecting fast and slow growing fungi from various types of ionizing radiation. *Environ Microbiol* **2017,** *19* (4), 1612-1624.

7.   Rogalla, S.; D'Alba, L.; Verdoodt, A.; Shawkey, M. D., Hot wings: thermal impacts of wing coloration on surface temperature during bird flight. *Journal of the Royal Society Interface* **2019,** *16* (156).

8.   Smith, K. R.; Cadena, V.; Endler, J. A.; Kearney, M. R.; Porter, W. P.; Stuart-Fox, D., Color Change for Thermoregulation versus Camouflage in Free-Ranging Lizards. *Am Nat* **2016,** *188* (6), 668-678.

9.   Brush, L.; Money, N. P., Invasive hyphal growth in Wangiella dermatitidis is induced by stab inoculation and shows dependence upon melanin biosynthesis. *Fungal Genet Biol* **1999,** *28* (3), 190-200.

10.   Bonser, R. H. C., Melanin and the Abrasion Resistance of Feathers. *Condor* **1995,** *97* (2), 590-591.

11.   Meredith, P.; Sarna, T., The physical and chemical properties of eumelanin. *Pigm Cell Res* **2006,** *19* (6), 572-594.

12.   Liu, Y. L.; Ai, K. L.; Lu, L. H., Polydopamine and Its Derivative Materials: Synthesis and Promising Applications in Energy, Environmental, and Biomedical Fields. *Chemical Reviews* **2014,** *114* (9), 5057-5115.

13.   Ju, K. Y.; Lee, J. W.; Im, G. H.; Lee, S.; Pyo, J.; Park, S. B.; Lee, J. H.; Lee, J. K., Bio-inspired, melanin-like nanoparticles as a highly efficient contrast agent for T1-weighted magnetic resonance imaging. *Biomacromolecules* **2013,** *14* (10), 3491-7.

14.   Liu, Y. L.; Ai, K. L.; Liu, J. H.; Deng, M.; He, Y. Y.; Lu, L. H., Dopamine-Melanin Colloidal Nanospheres: An Efficient Near-Infrared Photothermal Therapeutic Agent for In Vivo Cancer Therapy. *Adv Mater* **2013,** *25* (9), 1353-1359.

15.   Xu, R.; Gouda, A.; Caso, M. F.; Soavi, F.; Santato, C., Melanin: A Greener Route To Enhance Energy Storage under Solar Light. *ACS Omega* **2019,** *4* (7), 12244-12251.

16.   Li, L.; Smitthipong, W.; Zeng, H. B., Mussel-inspired hydrogels for biomedical and environmental applications. *Polym Chem-Uk* **2015,** *6* (3), 353-358.

17.   Cao, W.; McCallum, N. C.; Ni, Q. Z.; Li, W.; Boyce, H.; Mao, H.; Zhou, X.; Sun, H.; Thompson, M. P.; Battistella, C.; Wasielewski, M. R.; Dhinojwala, A.; Shawkey, M. D.; Burkart, M. D.; Wang, Z.; Gianneschi, N. C., Selenomelanin: An Abiotic Selenium Analogue of Pheomelanin. *J Am Chem Soc* **2020,** *142* (29), 12802-12810.

18.   Brenner, M.; Hearing, V. J., The protective role of melanin against UV damage in human skin. *Photochem Photobiol* **2008,** *84* (3), 539-549.

19.   de Galvez, M. V.; Aguilera, J.; Bernabo, J. L.; Sanchez-Roldan, C.; Herrera-Ceballos, E., Human Hair as a Natural Sun Protection Agent: A Quantitative Study. *Photochem Photobiol* **2015,** *91* (4), 966-970.

20.   Herrling, T.; Jung, K.; Fuchs, J., The role of melanin as protector against free radicals in skin and its role as free radical indicator in hair. *Spectrochim Acta A* **2008,** *69* (5), 1429-1435.

21.   Stoddard, M. C.; Prum, R. O., How colorful are birds? Evolution of the avian plumage color gamut. *Behav Ecol* **2011,** *22* (5), 1042-1052.

22.   Pihet, M.; Vandeputte, P.; Tronchin, G.; Renier, G.; Saulnier, P.; Georgeault, S.; Mallet, R.; Chabasse, D.; Symoens, F.; Bouchara, J. P., Melanin is an essential component for the integrity of the cell wall of Aspergillus fumigatus conidia. *Bmc Microbiol* **2009,** *9*.

23.   d'Ischia, M.; Napolitano, A.; Ball, V.; Chen, C. T.; Buehler, M. J., Polydopamine and Eumelanin: From Structure-Property Relationships to a Unified Tailoring Strategy. *Accounts Chem Res* **2014,** *47* (12), 3541-3550.

24.   Liebscher, J.; Mrowczynski, R.; Scheidt, H. A.; Filip, C.; Hadade, N. D.; Turcu, R.; Bende, A.; Beck, S., Structure of polydopamine: a never-ending story? *Langmuir* **2013,** *29* (33), 10539-48.

25.   Hong, S.; Na, Y. S.; Choi, S.; Song, I. T.; Kim, W. Y.; Lee, H., Non-Covalent Self-Assembly and Covalent Polymerization Co-Contribute to Polydopamine Formation. *Adv Funct Mater* **2012,** *22* (22), 4711-4717.

26.   Hong, S.; Wang, Y.; Park, S. Y.; Lee, H., Progressive fuzzy cation-pi assembly of biological catecholamines. *Sci Adv* **2018,** *4* (9).

27.   Solano, F., Melanins: Skin Pigments and Much More—Types, Structural Models, Biological Functions, and Formation Routes. *New Journal of Science* **2014,** *2014*, 1-28.

28.   Cao, W.; Zhou, X.; McCallum, N. C.; Hu, Z.; Ni, Q. Z.; Kapoor, U.; Heil, C. M.; Cay, K. S.; Zand, T.; Mantanona, A. J.; Jayaraman, A.; Dhinojwala, A.; Deheyn, D. D.; Shawkey, M. D.; Burkart, M. D.; Rinehart, J. D.; Gianneschi, N. C., Unraveling the Structure and Function of Melanin through Synthesis. *J Am Chem Soc* **2021**.

29.   Hu, D. N.; Simon, J. D.; Sarna, T., Role of ocular melanin in ophthalmic physiology and pathology. *Photochem Photobiol* **2008,** *84* (3), 639-644.

30.   Bartels, S.; Ito, S.; Trune, D. R.; Nuttall, A. L., Noise-induced hearing loss: the effect of melanin in the stria vascularis. *Hearing Res* **2001,** *154* (1-2), 116-123.

31.   Zucca, F. A.; Segura-Aguilar, J.; Ferrari, E.; Munoz, P.; Paris, I.; Sulzer, D.; Sarna, T.; Casella, L.; Zecca, L., Interactions of iron, dopamine and neuromelanin pathways in brain aging and Parkinson's disease. *Prog Neurobiol* **2017,** *155*, 96-119.

32.   Simon, J. D.; Peles, D. N., The Red and the Black. *Accounts Chem Res* **2010,** *43* (11), 1452-1460.

33.   Xu, H. Y.; Zhang, G.; Xu, K. G.; Wang, L. Y.; Yu, L.; Xing, M. M. Q.; Qiu, X. Z., Mussel-inspired dual-functional PEG hydrogel inducing mineralization and inhibiting infection in maxillary bone reconstruction. *Mat Sci Eng C-Mater* **2018,** *90*, 379-386.

34.   Bernsmann, F.; Ball, V.; Addiego, F. D. R.; Ponche, A.; Michel, M.; Gracio, J. J. D. A.; Toniazzo, V. R.; Ruch, D., Dopamine−Melanin Film Deposition Depends on the Used Oxidant and Buffer Solution. *Langmuir* **2011,** *27* (6), 2819-2825.

35.   Ito, S., Encapsulation of a reactive core in neuromelanin. *P Natl Acad Sci USA* **2006,** *103* (40), 14647-14648.

36.   Langfelder, K.; Streibel, M.; Jahn, B.; Haase, G.; Brakhage, A. A., Biosynthesis of fungal melanins and their importance for human pathogenic fungi. *Fungal Genet Biol* **2003,** *38* (2), 143-158.

37.   Chatterjee, S.; Prados-Rosales, R.; Itin, B.; Casadevall, A.; Stark, R. E., Solid-state NMR Reveals the Carbon-based Molecular Architecture of Cryptococcus neoformans Fungal Eumelanins in the Cell Wall. *J Biol Chem* **2015,** *290* (22), 13779-13790.

38.   Zhong, J. Y.; Frases, S.; Wang, H.; Casadevall, A.; Stark, R. E., Following fungal melanin biosynthesis with solid-state NMR: Biopolyrner molecular structures and possible connections to cell-wall polysaccharides. *Biochemistry-Us* **2008,** *47* (16), 4701-4710.

39.   Shawkey, M. D.; D'Alba, L.; Xiao, M.; Schutte, M.; Buchholz, R., Ontogeny of an Iridescent Nanostructure Composed of Hollow Melanosomes. *J Morphol* **2015,** *276* (4), 378-384.

40.   Eliason, C. M.; Bitton, P. P.; Shawkey, M. D., How hollow melanosomes affect iridescent colour production in birds. *P Roy Soc B-Biol Sci* **2013,** *280* (1767).

41.   Azab, M. M.; Cherif, R.; Finnie, A. L.; Abou El-Alamin, M. M.; Sultan, M. A.; Wark, A. W., Optimized polydopamine coating and DNA conjugation onto gold nanorods for single nanoparticle bioaffinity measurements. *Analyst* **2018,** *143* (7), 1635-1643.

42.   Obare, S. O.; Jana, N. R.; Murphy, C. J., Preparation of polystyrene- and silica-coated gold nanorods and their use as templates for the synthesis of hollow nanotubes. *Nano Lett* **2001,** *1* (11), 601-603.

43.   Yi, B.; Shen, H. F., Liquid-immune structural colors with angle-independence inspired from hollow melanosomes. *Chem Commun* **2017,** *53* (66), 9234-9237.

44.   Wang, Y.; Su, J.; Li, T.; Ma, P. M.; Bai, H. Y.; Xie, Y.; Chen, M. Q.; Dong, W. F., A Novel UV-Shielding and Transparent Polymer Film: When Bioinspired Dopamine-Melanin Hollow Nanoparticles Join Polymers. *ACS Applied Materials & Interfaces* **2017,** *9* (41), 36281-36289.

45.   Siwicka, Z. E.; Son, F. A.; Battistella, C.; Moore, M. H.; Korpanty, J.; McCallum, N. C.; Wang, Z.; Johnson, B. J.; Farha, O. K.; Gianneschi, N. C., Synthetic Porous Melanin. *J Am Chem Soc* **2021**.

46.   McCallum, N. C. S., F. A.; Clemons, T. D.; Weigand, S. J.; Gnanasekaran, K.; Battistella, C.; Barnes, B. B.; Abeyratne-Perera, H.; Siwicka, Z. E.; Forman, C. J.; Zhou, X.; Moore, M. H.; Savin, D. A.; Stupp, S. I.; Wang, Z.; Vora, G. J.; Johnson, B. J.; Farha, O. K.; Gianneschi, N. C., Allomelanin: A Biopolymer of Intrinsic Microporosity. *J. Am. Chem. Soc.* **2021**.

47.   Huang, Y. R.; Li, Y. W.; Hu, Z. Y.; Yue, X. J.; Proetto, M. T.; Jones, Y.; Gianneschi, N. C., Mimicking Melanosomes: Polydopamine Nanoparticles as Artificial Microparasols. *Acs Central Sci* **2017,** *3* (6), 564-569.

48.   Wang, C. P.; Wang, D.; Dai, T. J.; Xu, P.; Wu, P. L.; Zou, Y.; Yang, P.; Hu, J. J.; Li, Y. W.; Cheng, Y. Y., Skin Pigmentation-Inspired Polydopamine Sunscreens. *Adv Funct Mater* **2018,** *28* (33).

49.   Robertson, K. L.; Mostaghim, A.; Cuomo, C. A.; Soto, C. M.; Lebedev, N.; Bailey, R. F.; Wang, Z., Adaptation of the Black Yeast Wangiella dermatitidis to Ionizing Radiation: Molecular and Cellular Mechanisms. *Plos One* **2012,** *7* (11).

50.   Dadachova, E.; Casadevall, A., Ionizing radiation: how fungi cope, adapt, and exploit with the help of melanin. *Current Opinion in Microbiology* **2008,** *11* (6), 525-531.

51.   Dadachova, E. Oral administration of melanin for protection against radiation. 2017.

52.   Van Dolah, F. M., Marine algal toxins: Origins, health effects, and their increased occurrence. *Environ Health Persp* **2000,** *108*, 133-141.

53.   Marin, S.; Ramos, A. J.; Cano-Sancho, G.; Sanchis, V., Mycotoxins: Occurrence, toxicology, and exposure assessment. *Food Chem Toxicol* **2013,** *60*, 218-237.

54.   Carolin, C. F.; Kumar, P. S.; Saravanan, A.; Joshiba, G. J.; Naushad, M., Efficient techniques for the removal of toxic heavy metals from aquatic environment: A review. *J Environ Chem Eng* **2017,** *5* (3), 2782-2799.

55.   Kim, K.; Tsay, O. G.; Atwood, D. A.; Churchill, D. G., Destruction and Detection of Chemical Warfare Agents. *Chemical Reviews* **2011,** *111* (9), 5345-5403.

56.   Cook, L. M.; Saccheri, I. J., The peppered moth and industrial melanism: evolution of a natural selection case study. *Heredity* **2013,** *110* (3), 207-212.

57.   Manirethan, V.; Raval, K.; Rajan, R.; Thaira, H.; Balakrishnan, R. M., Kinetic and thermodynamic studies on the adsorption of heavy metals from aqueous solution by melanin nanopigment obtained from marine source: Pseudomonas stutzeri. *J Environ Manage* **2018,** *214*, 315-324.

58.   Chen, W.; Hashimoto, K.; Omata, Y.; Ohgami, N.; Tazaki, A.; Deng, Y. Q.; Kondo-Ida, L.; Intoh, A.; Kato, M., Adsorption of molybdenum by melanin. *Environ Health Prev* **2019,** *24* (1).

59.   Woertz, J. R.; Kinney, K. A.; McIntosh, N. D. P.; Szaniszlo, P. J., Removal of toluene in a vapor-phase bioreactor containing a strain of the dimorphic black yeast Exophiala lecanii-corni. *Biotechnol Bioeng* **2001,** *75* (5), 550-558.

60.   Solano, F., Melanins: Skin Pigments and Much More-Types, Structural Models, Biological Functions, and Formation Routes. *New J. Sci.* **2014,** *2014*, 28.

61.   Hong, L.; Simon, J. D., Current Understanding of the Binding Sites, Capacity, Affinity, and Biological Significance of Metals in Melanin. *J. Phys. Chem. B* **2007,** *111* (28), 7938-7947.

62.   Liu, Y.; Hong, L.; Kempf, V. R.; Wakamatsu, K.; Ito, S.; Simon, J. D., Ion-Exchange and Adsorption of Fe(III) by Sepia Melanin. *Pigm. Cell Res.* **2004,** *17* (3), 262-269.

63.   Lian, H.; Yan, L.; D., S. J., Binding of Metal Ions to Melanin and Their Effects on the Aerobic Reactivity¶. *Photochem. Photobiol.* **2004,** *80* (3), 477-481.

64.   Tada, M.; Kohno, M.; Niwano, Y., Scavenging or Quenching Effect of Melanin on Superoxide Anion and Singlet Oxygen. *J. Clin. Biochem. Nutr.* **2010,** *46* (3), 224-228.

65.   Seagle, B.-L. L.; Rezai, K. A.; Gasyna, E. M.; Kobori, Y.; Rezaei, K. A.; Norris, J. R., Time-Resolved Detection of Melanin Free Radicals Quenching Reactive Oxygen Species. *J. Am. Chem. Soc.* **2005,** *127* (32), 11220-11221.

66.   Boulton, M.; Różanowska, M.; Różanowski, B., Retinal Photodamage. *J. Photochem. Photobiol. B: Biol.* **2001,** *64* (2), 144-161.

67.   Brenner, M.; Hearing, V. J., The Protective Role of Melanin Against UV Damage in Human Skin†. *Photochem. Photobiol.* **2007,** *84* (3), 539-549.

68.   Kobayashi, N.; Muramatsu, T.; Yamashina, Y.; Shirai, T.; Ohnishi, T.; Mori, T., Melanin Reduces Ultraviolet-Induced DNA Damage Formation and Killing Rate in Cultured Human Melanoma Cells. *J. Invest. Dermatol.* **1993,** *101* (5), 685-689.

69.   Tadokoro, T.; Kobayashi, N.; Zmudzka, B. Z.; Ito, S.; Wakamatsu, K.; Yamaguchi, Y.; Korossy, K. S.; Miller, S. A.; Beer, J. Z.; Hearing, V. J., UV-Induced DNA Damage and Melanin Content in Human Skin Differing in Racial/Ethnic Origin. *FASEB J.* **2003,** *17* (9), 1177-1179.

70.   Park, J.-Y.; Kim, S.-N.; Yoo, J.; Jang, J.; Lee, A.; Oh, J.-Y.; Kim, H.; Oh, S. T.; Park, S.-U.; Kim, J.; Park, H.-J.; Jeon, S., Novel Neuroprotective Effects of Melanin-Concentrating Hormone in Parkinson's Disease. *Mol. Neurobiol.* **2017,** *54* (10), 7706-7721.

71.   Marco, d. I.; Kazumasa, W.; Fabio, C.; Eduardo, D. M.; Carlos, G. B. J.; Stephane, C.; Ismael, G.; Ghanem, G.; Koike, K.; Paul, M.; Alessandro, P.; Clara, S.; Tadeusz, S.; D., S. J.; Luigi, Z.; A., Z. F.; Alessandra, N.; Shosuke, I., Melanins and Melanogenesis: from Pigment Cells to Human Health and Technological Applications. *Pigm. Cell Melanoma Res.* **2015,** *28* (5), 520-544.

72.   Hunt, G.; Kyne, S.; Ito, S.; Wakamatsu, K.; Todd, C.; Thody, A. J., Eumelanin and Phaeomelanin Contents of Human Epidermis and Cultured Melanocytes. *Pigm. Cell Res.* **1995,** *8* (4), 202-208.

73.   Alison, H.; Carol, O.; Brian, D.; Kazumasa, W.; Shosuke, I.; Jonathan, R., Eumelanin and Pheomelanin Concentrations in Human Epidermis before and after UVB Irradiation. *Pigm. Cell Res.* **2005,** *18* (3), 220-223.

74.   Wakamatsu, K.; Fujikawa, K.; Zucca, F. A.; Zecca, L.; Ito, S., The Structure of Neuromelanin as Studied by Chemical Degradative Methods. *J. Neurochem.* **2003,** *86* (4), 1015-1023.

75.   Schmaler-Ripcke, J.; Sugareva, V.; Gebhardt, P.; Winkler, R.; Kniemeyer, O.; Heinekamp, T.; Brakhage, A. A., Production of Pyomelanin, a Second Type of Melanin, via the Tyrosine Degradation Pathway in Aspergillus fumigatus. *Appl. Environ. Microbiol.* **2009,** *75* (2), 493-503.

76.   Haining, R.; Achat-Mendes, C., Neuromelanin, One of the Most Overlooked Molecules in Modern Medicine, is not a Spectator. *Neural Regen. Res.* **2017,** *12* (3), 372-375.

77.   D'Alba, L.; Shawkey, M. D., Melanosomes: Biogenesis, Properties, and Evolution of an Ancient Organelle. *Physiol. Rev.* **2019,** *99* (1), 1-19.

78.   Lee, H.; Dellatore, S. M.; Miller, W. M.; Messersmith, P. B., Mussel-Inspired Surface Chemistry for Multifunctional Coatings. *Science* **2007,** *318* (5849), 426-430.

79.   Huang, L.; Liu, M. Y.; Huang, H. Y.; Wen, Y. Q.; Zhang, X. Y.; Wei, Y., Recent Advances and Progress on Melanin-like Materials and Their Biomedical Applications. *Biomacromolecules* **2018,** *19* (6), 1858-1868.

80.   Tokura, Y.; Harvey, S.; Chen, C.; Wu, Y.; Ng, D. Y. W.; Weil, T., Fabrication of Defined Polydopamine Nanostructures by DNA Origami-Templated Polymerization. *Angew. Chem. Int. Ed. Engl.* **2018,** *57* (6), 1587-1591.

81.   Lampel, A.; McPhee, S. A.; Park, H. A.; Scott, G. G.; Humagain, S.; Hekstra, D. R.; Yoo, B.; Frederix, P. W. J. M.; Li, T. D.; Abzalimov, R. R.; Greenbaum, S. G.; Tuttle, T.; Hu, C. H.; Bettinger, C. J.; Ulijn, R. V., Polymeric Peptide Pigments with Sequence-Encoded Properties. *Science* **2017,** *356* (6342), 1064-1068.

82.   Huang, Y.; Li, Y.; Hu, Z.; Yue, X.; Proetto, M. T.; Jones, Y.; Gianneschi, N. C., Mimicking Melanosomes: Polydopamine Nanoparticles as Artificial Microparasols. *ACS Cent. Sci.* **2017,** *3* (6), 564-569.

83.   Wang, C.; Wang, D.; Dai, T.; Xu, P.; Wu, P.; Zou, Y.; Yang, P.; Hu, J.; Li, Y.; Cheng, Y., Skin Pigmentation-Inspired Polydopamine Sunscreens. *Adv. Funct. Mater.* **2018,** *28* (33), 1802127.

84.   Liu, X.; Cao, J.; Li, H.; Li, J.; Jin, Q.; Ren, K.; Ji, J., Mussel-Inspired Polydopamine: a Biocompatible and Ultrastable Coating for Nanoparticles in vivo. *ACS Nano* **2013,** *7* (10), 9384-95.

85.   Zhang, X.; Wang, S.; Xu, L.; Feng, L.; Ji, Y.; Tao, L.; Li, S.; Wei, Y., Biocompatible Polydopamine Fluorescent Organic Nanoparticles: Facile Preparation and Cell Imaging. *Nanoscale* **2012,** *4* (18), 5581-5584.

86.   Wang, Z.; Xie, Y.; Li, Y.; Huang, Y.; Parent, L. R.; Ditri, T.; Zang, N.; Rinehart, J. D.; Gianneschi, N. C., Tunable, Metal-Loaded Polydopamine Nanoparticles Analyzed by Magnetometry. *Chem. Mater.* **2017,** *29* (19), 8195-8201.

87.   Xiao, M.; Li, Y.; Allen, M. C.; Deheyn, D. D.; Yue, X.; Zhao, J.; Gianneschi, N. C.; Shawkey, M. D.; Dhinojwala, A., Bio-Inspired Structural Colors Produced via Self-Assembly of Synthetic Melanin Nanoparticles. *ACS Nano* **2015,** *9* (5), 5454-5460.

88.   Nosanchuk, J. D.; Casadevall, A., The Contribution of Melanin to Microbial Pathogenesis. *Cell. Microbiol.* **2003,** *5* (4), 203-223.

89.   Nosanchuk, J. D.; Stark, R. E.; Casadevall, A., Fungal Melanin: What do We Know About Structure? *Front. Microbiol.* **2015,** *6* (1463).

90.   Pihet, M.; Vandeputte, P.; Tronchin, G.; Renier, G.; Saulnier, P.; Georgeault, S.; Mallet, R.; Chabasse, D.; Symoens, F.; Bouchara, J.-P., Melanin is an Essential Component for the Integrity of the Cell Wall of Aspergillus Fumigatus Conidia. *BMC Microbiol.* **2009,** *9* (1), 177.

91.   Eisenman, H. C.; Nosanchuk, J. D.; Webber, J. B. W.; Emerson, R. J.; Camesano, T. A.; Casadevall, A., Microstructure of cell wall-associated melanin in the human pathogenic fungus cryptococcus neoformans. *Biochemistry-Us* **2005,** *44* (10), 3683-3693.

92.   Dadachova, E.; Bryan, R. A.; Huang, X. C.; Moadel, T.; Schweitzer, A. D.; Aisen, P.; Nosanchuk, J. D.; Casadevall, A., Ionizing Radiation Changes the Electronic Properties of Melanin and Enhances the Growth of Melanized Fungi. *Plos One* **2007,** *2* (5).

93.   Schweitzer, A. D.; Revskaya, E.; Chu, P.; Pazo, V.; Friedman, M.; Nosanchuk, J. D.; Cahill, S.; Frases, S.; Casadevall, A.; Dadachova, E., Melanin-Covered Nanoparticles for Protection of Bone Marrow during Radiation Therapy of Cancer. *Int. J. Radiat. Oncol. Biol. Phys.* **2010,** *78* (5), 1494-502.

94.   Cecchini, M. M.; Reale, S.; Manini, P.; d'Ischia, M.; De Angelis, F., Modeling Fungal Melanin Buildup: Biomimetic Polymerization of 1,8-Dihydroxynaphthalene Mapped by Mass Spectrometry. *Chem-Eur J* **2017,** *23* (33), 8092-8098.

95.   Manini, P.; Bietti, M.; Galeotti, M.; Salamone, M.; Lanzalunga, O.; Cecchini, M. M.; Reale, S.; Crescenzi, O.; Napolitano, A.; De Angelis, F.; Barone, V.; d'Ischia, M.,

Characterization and Fate of Hydrogen-Bonded Free-Radical Intermediates and Their Coupling Products from the Hydrogen Atom Transfer Agent 1,8-Naphthalenediol. *ACS Omega* **2018,** *3* (4), 3918-3927.

96. Song, B.; Wei, H.; Wang, Z.; Zhang, X.; Smet, M.; Dehaen, W., Supramolecular Nanofibers by Self-Organization of Bola-amphiphiles through a Combination of Hydrogen Bonding and π–π Stacking Interactions. *Adv. Mater.* **2007,** *19* (3), 416-420.

97. Ju, K. Y.; Lee, Y.; Lee, S.; Park, S. B.; Lee, J. K., Bioinspired Polymerization of Dopamine to Generate Melanin-Like Nanoparticles Having an Excellent Free-Radical-Scavenging Property. *Biomacromolecules* **2011,** *12* (3), 625-632.

98. Kobayashi, N.; Nakagawa, A.; Muramatsu, T.; Yamashina, Y.; Shirai, T.; Hashimoto, M. W.; Ishigaki, Y.; Ohnishi, T.; Mori, T., Supranuclear melanin caps reduce ultraviolet induced DNA photoproducts in human epidermis. *J Invest Dermatol* **1998,** *110* (5), 806-810.

99. Byers, H. R.; Maheshwary, S.; Amodeo, D. M.; Dykstra, S. G., Role of cytoplasmic dynein in perinuclear aggregation of phagocytosed melanosomes and supranuclear melanin cap formation in human keratinocytes. *J Invest Dermatol* **2003,** *121* (4), 813-820.

100. Bikle, D. D.; Xie, Z.; Tu, C. L., Calcium regulation of keratinocyte differentiation. *Expert Rev Endocrinol Metab* **2012,** *7* (4), 461-472.

101. Xiao, M.; Hu, Z.; Wang, Z.; Li, Y.; Tormo, A. D.; Le Thomas, N.; Wang, B.; Gianneschi, N. C.; Shawkey, M. D.; Dhinojwala, A., Bioinspired Bright Noniridescent Photonic Melanin Supraballs. *Sci. Adv.* **2017,** *3* (9), e1701151.

102. Hong, L.; Simon, J. D., Current understanding of the binding sites, capacity, affinity, and biological significance of metals in melanin. *J Phys Chem B* **2007,** *111* (28), 7938-7947.

103. Lee, B. P.; Messersmith, P. B.; Israelachvili, J. N.; Waite, J. H., Mussel-Inspired Adhesives and Coatings. *Annu Rev Mater Res* **2011,** *41*, 99-132.

104. Lynge, M. E.; van der Westen, R.; Postma, A.; Stadler, B., Polydopamine-a nature-inspired polymer coating for biomedical science. *Nanoscale* **2011,** *3* (12), 4916-4928.

105. Ju, K.-Y.; Lee, Y.; Lee, S.; Park, S. B.; Lee, J.-K., Bioinspired Polymerization of Dopamine to Generate Melanin-Like Nanoparticles Having an Excellent Free-Radical-Scavenging Property. *Biomacromolecules* **2011,** *12* (3), 625-632.

106. Manini, P.; Lino, V.; Franchi, P.; Gentile, G.; Sibillano, T.; Giannini, C.; Picardi, E.; Napolitano, A.; Valgimigli, L.; Chiappe, C.; D'Ischia, M., A Robust Fungal Allomelanin Mimic: An Antioxidant and Potent pi-Electron Donor with Free-Radical Properties that can be Tuned by Ionic Liquids. *Chempluschem* **2019,** *84* (9), 1331-1337.

107. Zhou, X. H.; McCallum, N. C.; Hu, Z. Y.; Cao, W.; Gnanasekaran, K.; Feng, Y. N.; Stoddart, J. F.; Wang, Z.; Gianneschi, N. C., Artificial Allomelanin Nanoparticles. *ACS Nano* **2019,** *13* (10), 10980-10990.

108. Budd, P. M.; Ghanem, B. S.; Makhseed, S.; McKeown, N. B.; Msayib, K. J.; Tattershall, C. E., Polymers of intrinsic microporosity (PIMs): robust, solution-processable, organic nanoporous materials. *Chem Commun (Camb)* **2004,** (2), 230-1.

109. Li, C. Y.; Ward, A. L.; Doris, S. E.; Pascal, T. A.; Prendergast, D.; Helms, B. A., Polysulfide-Blocking Microporous Polymer Membrane Tailored for Hybrid Li-Sulfur Flow Batteries. *Nano Lett* **2015,** *15* (9), 5724-5729.

110.   Weng, X. L.; Baez, J. E.; Khiterer, M.; Hoe, M. Y.; Bao, Z. B.; Shea, K. J., Chiral Polymers of Intrinsic Microporosity: Selective Membrane Permeation of Enantiomers. *Angew Chem Int Edit* **2015,** *54* (38), 11214-11218.

111.   Kapoor, U.; Jayaraman, A., Self-Assembly of Allomelanin Dimers and the Impact of Poly(ethylene glycol) on the Assembly: A Molecular Dynamics Simulation Study. *J Phys Chem B* **2020,** *124* (13), 2702-2714.

112.   Manini, P.; Lino, V.; D'Errico, G.; Reale, S.; Napolitano, A.; De Angelis, F.; d'Ischia, M., "Blackness" is an index of redox complexity in melanin polymers. *Polym Chem-Uk* **2020,** *11* (31), 5005-5010.

113.   Franke, D.; Petoukhov, M. V.; Konarev, P. V.; Panjkovich, A.; Tuukkanen, A.; Mertens, H. D. T.; Kikhney, A. G.; Hajizadeh, N. R.; Franklin, J. M.; Jeffries, C. M.; Svergun, D. I., ATSAS 2.8: a comprehensive data analysis suite for small-angle scattering from macromolecular solutions. *J Appl Crystallogr* **2017,** *50*, 1212-1225.

114.   Moribe, S.; Chen, Z. J.; Alayoglu, S.; Syed, Z. H.; Islamoglu, T.; Farha, O. K., Ammonia Capture within Isoreticular Metal-Organic Frameworks with Rod Secondary Building Units. *ACS Mater Lett* **2019,** *1* (4), 476-480.

115.   Rieth, A. J.; Dinca, M., Controlled Gas Uptake in Metal-Organic Frameworks with Record Ammonia Sorption. *J Am Chem Soc* **2018,** *140* (9), 3461-3466.

116.   Chen, Y. W.; Zhang, X.; Ma, K. K.; Chen, Z. J.; Wang, X. J.; Knapp, J.; Alayoglu, S.; Wang, F. F.; Xia, Q. B.; Li, Z.; Islamoglu, T.; Farha, O. K., Zirconium-Based Metal-Organic Framework with 9-Connected Nodes for Ammonia Capture. *ACS Appl Nano Mater* **2019,** *2* (10), 6098-6102.

117.   Chen, Z.; Wang, X.; Cao, R.; Idrees, K. B.; Liu, X.; Wasson, M. C.; Farha, O. K., Water-Based Synthesis of a Stable Iron-Based Metal–Organic Framework for Capturing Toxic Gases. *ACS Mater Lett* **2020,** *2*, 1129-1134.

118.   Van Humbeck, J. F.; McDonald, T. M.; Jing, X.; Wiers, B. M.; Zhu, G.; Long, J. R., Ammonia capture in porous organic polymers densely functionalized with Bronsted acid groups. *J Am Chem Soc* **2014,** *136* (6), 2432-40.

119.   Barin, G.; Peterson, G. W.; Crocella, V.; Xu, J.; Colwell, K. A.; Nandy, A.; Reimer, J. A.; Bordiga, S.; Long, J. R., Highly effective ammonia removal in a series of Bronsted acidic porous polymers: investigation of chemical and structural variations. *Chem Sci* **2017,** *8* (6), 4399-4409.

120.   Dawson, R.; Stockel, E.; Holst, J. R.; Adams, D. J.; Cooper, A. I., Microporous organic polymers for carbon dioxide capture. *Energ Environ Sci* **2011,** *4* (10), 4239-4245.

121.   Simon, C. M.; Smit, B.; Haranczyk, M., pyIAST: Ideal adsorbed solution theory (IAST) Python package. *Comput Phys Commun* **2016,** *200*, 364-380.

122.   Spanopoulos, I.; Xydias, P.; Malliakas, C. D.; Trikalitis, P. N., A Straight Forward Route for the Development of Metal-Organic Frameworks Functionalized with Aromatic -OH Groups: Synthesis, Characterization, and Gas (N-2, Ar, H-2, CO2, CH4, NH3) Sorption Properties. *Inorg Chem* **2013,** *52* (2), 855-862.

123.   Chen, Z. X.; Xiang, S. C.; Arman, H. D.; Li, P.; Zhao, D. Y.; Chen, B. L., Significantly Enhanced CO2/CH4 Separation Selectivity within a 3D Prototype Metal-Organic Framework Functionalized with OH Groups on Pore Surfaces at Room Temperature. *Eur J Inorg Chem* **2011,** (14), 2227-2231.

124. Venna, S. R.; Carreon, M. A., Highly permeable zeolite imidazolate framework-8 membranes for CO2/CH4 separation. *J Am Chem Soc* **2010,** *132* (1), 76-8.

125. Li, Y.; Wang, S.; Wang, B.; Wang, Y.; Wei, J., Sustainable Biomass Glucose-Derived Porous Carbon Spheres with High Nitrogen Doping: As a Promising Adsorbent for CO2/CH4/N2 Adsorptive Separation. *Nanomaterials (Basel)* **2020,** *10* (1), 1-17.

126. Bae, Y. S.; Mulfort, K. L.; Frost, H.; Ryan, P.; Punnathanam, S.; Broadbelt, L. J.; Hupp, J. T.; Snurr, R. Q., Separation of CO2 from CH4 using mixed-ligand metal-organic frameworks. *Langmuir* **2008,** *24* (16), 8592-8.

127. Bartelt-Hunt, S. L.; Knappe, D. R. U.; Barlaz, M. A., A review of chemical warfare agent simulants for the study of environmental behavior. *Crit Rev Env Sci Tec* **2008,** *38* (2), 112-136.

128. Johnson, B. J.; Malanoski, A. P.; Leska, I. A.; Melde, B. J.; Taft, J. R.; Dinderman, M. A.; Deschamps, J. R., Adsorption of organophosphates from solution by porous organosilicates: Capillary phase-separation. *Micropor Mesopor Mat* **2014,** *195*, 154-160.

129. Dolgin, E., Syrian gas attack reinforces need for better anti-sarin drugs. *Nat Med* **2013,** *19* (10), 1194-1195.

130. John, H.; van der Schans, M. J.; Koller, M.; Spruit, H. E. T.; Worek, F.; Thiermann, H.; Noort, D., Fatal sarin poisoning in Syria 2013: forensic verification within an international laboratory network. *Forensic Toxicol* **2018,** *36* (1), 61-71.

131. Martin, B. D.; Justin, G. A.; Moore, M. H.; Naciri, J.; Mazure, T.; Melde, B. J.; Stroud, R. M.; Ratna, B., An Elastomeric Poly(Thiophene-EDOT) Composite with a Dynamically Variable Permeability Towards Organic and Water Vapors. *Adv Funct Mater* **2012,** *22* (15), 3116-3127.

132. Wang, S.; Pomerantz, N. L.; Dai, Z.; Xie, W.; Anderson, E. E.; Miller, T.; Khan, S. A.; Parsons, G. N., Polymer of intrinsic microporosity (PIM) based fibrous mat: combining particle filtration and rapid catalytic hydrolysis of chemical warfare agent simulants into a highly sorptive, breathable, and mechanically robust fiber matrix. *Materials Today Advances* **2020,** *8*.

133. Wheeler, M. H.; Abramczyk, D.; Puckhaber, L. S.; Naruse, M.; Ebizuka, Y.; Fujii, I.; Szaniszlo, P. J., New Biosynthetic Step in the Melanin Pathway of Wangiella (Exophiala) dermatitidis: Evidence for 2-Acetyl-1,3,6,8-Tetrahydroxynaphthalene as a Novel Precursor. *Eukaryot Cell* **2008,** *7* (10), 1699-1711.

134. Geis, P. A.; Wheeler, M. H.; Szaniszlo, P. J., Pentaketide Metabolites of Melanin Synthesis in the Dematiaceous Fungus Wangiella-Dermatitidis. *Arch Microbiol* **1984,** *137* (4), 324-328.

135. Wang, Z.; Tschirhart, T.; Schultzhaus, Z.; Kelly, E. E.; Chen, A.; Oh, E.; Nag, O.; Glaser, E. R.; Kim, E.; Lloyd, P. F.; Charles, P. T.; Li, W.; Leary, D.; Compton, J.; Phillips, D. A.; Dhinojwala, A.; Payne, G. F.; Vora, G. J., Melanin Produced by the Fast-Growing Marine Bacterium Vibrio natriegens through Heterologous Biosynthesis: Characterization and Application. *Appl Environ Microb* **2019,** *86* (5), 1-18.

136. Chatterjee, S.; Prados-Rosales, R.; Frases, S.; Itin, B.; Casadevall, A.; Stark, R. E., Using Solid-State NMR To Monitor the Molecular Consequences of Cryptococcus neoformans Melanization with Different Catecholamine Precursors. *Biochemistry-Us* **2012,** *51* (31), 6080-6088.

137. Garcia-Rivera, J.; Eisenman, H. C.; Nosanchuk, J. D.; Aisen, P.; Zaragoza, O.; Moadel, T.; Dadachova, E.; Casadevall, A., Comparative analysis of Cryptococcus neoformans acid-

resistant particles generated from pigmented cells grown in different laccase substrates. *Fungal Genet Biol* **2005,** *42* (12), 989-998.

138.   Vikrant, K.; Kumar, V.; Kim, K. H.; Kukkar, D., Metal-organic frameworks (MOFs): potential and challenges for capture and abatement of ammonia. *J Mater Chem A* **2017,** *5* (44), 22877-22896.

139.   DeCoste, J. B.; Peterson, G. W., Metal-Organic Frameworks for Air Purification of Toxic Chemicals. *Chemical Reviews* **2014,** *114* (11), 5695-5727.

140.   Yang, Y. J.; Faheem, M.; Wang, L. L.; Meng, Q. H.; Sha, H. Y.; Yang, N.; Yuan, Y.; Zhu, G. S., Surface Pore Engineering of Covalent Organic Frameworks for Ammonia Capture through Synergistic Multivariate and Open Metal Site Approaches. *ACS Central Sci* **2018,** *4* (6), 748-754.

141.   Romero, V.; Fernandes, S. P. S.; Rodriguez-Lorenzo, L.; Kolen'ko, Y. V.; Espina, B.; Salonen, L. M., Recyclable magnetic covalent organic framework for the extraction of marine biotoxins. *Nanoscale* **2019,** *11* (13), 6072-6079.

142.   Kanehashi, S.; Chen, G. Q.; Scholes, C. A.; Ozcelik, B.; Hua, C.; Ciddor, L.; Southon, P. D.; D'Alessandro, D. M.; Kentish, S. E., Enhancing gas permeability in mixed matrix membranes through tuning the nanoparticle properties. *J Membrane Sci* **2015,** *482*, 49-55.

143.   Sabetghadam, A.; Liu, X. L.; Benzaqui, M.; Gkaniatsou, E.; Orsi, A.; Lozinska, M. M.; Sicard, C.; Johnson, T.; Steunou, N.; Wright, P. A.; Serre, C.; Gascon, J.; Kapteijn, F., Influence of Filler Pore Structure and Polymer on the Performance of MOF-Based Mixed-Matrix Membranes for CO2 Capture. *Chem-Eur J* **2018,** *24* (31), 7949-7956.

144.   Ilavsky, J.; Jemian, P. R., Irena: tool suite for modeling and analysis of small-angle scattering. *J Appl Crystallogr* **2009,** *42*, 347-353.

145.   Petoukhov, M. V.; Konarev, P. V.; Kikhney, A. G.; Svergun, D. I., ATSAS 2.1 - towards automated and web-supported small-angle scattering data analysis. *J Appl Crystallogr* **2007,** *40*, S223-S228.

146.   Franke, D.; Svergun, D. I., DAMMIF, a program for rapid ab-initio shape determination in small-angle scattering. *J Appl Crystallogr* **2009,** *42*, 342-346.

147.   Volkov, V. V.; Svergun, D. I., Uniqueness of ab initio shape determination in small-angle scattering. *J Appl Crystallogr* **2003,** *36*, 860-864.

148.   Gebreegzi, Y. T.; Foster, G. D.; Khan, S. U., Simultaneous determination of carbaryl, malathion, fenitrothion, and diazinon residues in sesame seeds (Sesamum indicum L.). *Journal of Agricultural and Food Chemistry* **2000,** *48* (11), 5165-5168.

149.   Johnson, B. J.; Melde, B. J.; Charles, P. T.; Cardona, D. C.; Dinderman, M. A.; Malanoski, A. P.; Qadri, S. B., Imprinted nanoporous organosilicas for selective adsorption, of nitroenergetic targets. *Langmuir* **2008,** *24* (16), 9024-9029.

150.   Johnson, B. J.; Melde, B. J.; Charles, P. T.; Dinderman, M. A.; Malanoski, A. P.; Leska, I. A.; Qadri, S. B., Macroporous silica for concentration of nitroenergetic targets. *Talanta* **2010,** *81* (4-5), 1454-1460.

151.   Johnson, B. J.; Melde, B. J.; Moore, M. H.; Malanoski, A. P.; Taft, J. R., Improving Sorbents for Glycerol Capture in Biodiesel Refinement. *Materials* **2017,** *10* (6).

152.   Battistella, C.; McCallum, N. C.; Gnanasekaran, K.; Zhou, X.; Caponetti, V.; Montalti, M.; Gianneschi, N. C., Mimicking Natural Human Hair Pigmentation with Synthetic Melanin. *ACS Central Sci* **2020,** *6* (7), 1179-1188.

153.   D'Onofrio, T. G. *Development of a Contact Permeation Test Fixture and Method*; ECBC-TR-1141; U.S. Army Research, Development and Engineering Command: 2013.

154.   Kar, F.; Fan, J. T.; Yu, W., Comparison of different test methods for the measurement of fabric or garment moisture transfer properties. *Meas Sci Technol* **2007,** *18* (7), 2033-2038.

155.   Pushpadass, H. A.; Marx, D. B.; Hanna, M. A., Effects of Extrusion Temperature and Plasticizers on the Physical and Functional Properties of Starch Films. *Starch-Starke* **2008,** *60* (10), 527-538.

156.   Nordlund, J. J., The melanocyte and the epidermal melanin unit: An expanded concept. *Dermatol Clin* **2007,** *25* (3), 271-+.

157.   Kortum, G. V., W.; Andrussow, K., *Dissociation Constants of Organic Acids in Aqueous Solution*. Butterworths: London, 1961.

158.   Jablonski, N. G., The Colour of Our Past and Present: The Evolution of Human Skin Pigmentation. *Colour of Our Future: Does Race Matter in Post-Apartheid South Africa?* **2015**, 17-24.

159.   van der Pols, J. C.; Williams, G. M.; Pandeya, N.; Logan, V.; Green, A. C., Prolonged prevention of squamous cell carcinoma of the skin by regular sunscreen use. *Cancer Epidem Biomar* **2006,** *15* (12), 2546-2548.

160.   Svarc, F., A brief illustrated history on sunscreens and sun protection. *Pure Appl Chem* **2015,** *87* (9-10), 929-936.

161.   Osterwalder, U.; Sohn, M.; Herzog, B., Global state of sunscreens. *Photodermatol Photo* **2014,** *30* (2-3), 62-80.

162.   Kollias, N., The absorption properties of "physical" sunscreens. *Arch Dermatol* **1999,** *135* (2), 209-210.

163.   Jansen, R.; Osterwalder, U.; Wang, S. Q.; Burnett, M.; Lim, H. W., Photoprotection Part II. Sunscreen: Development, efficacy, and controversies. *Journal of the American Academy of Dermatology* **2013,** *69* (6).

164.   Ruszkiewicz, J. A.; Pinkas, A.; Ferrer, B.; Peres, T. V.; Tsatsakis, A.; Aschner, M., Neurotoxic effect of active ingredients in sunscreen products, a contemporary review. *Toxicol Rep* **2017,** *4*, 245-259.

165.   Schneider, S. L.; Lim, H. W., Review of environmental effects of oxybenzone and other sunscreen active ingredients. *Journal of the American Academy of Dermatology* **2019,** *80* (1), 266-271.

166.   Siller, A.; Blaszak, S. C.; Lazar, M.; Olasz Harken, E., Update About the Effects of the Sunscreen Ingredients Oxybenzone and Octinoxate on Humans and the Environment. *Plast Surg Nurs* **2019,** *39* (4), 157-160.

167.   Smijs, T. G.; Pavel, S., Titanium dioxide and zinc oxide nanoparticles in sunscreens: focus on their safety and effectiveness. *Nanotechnol Sci Appl* **2011,** *4*, 95-112.

168.   Gallagher, M., Exposure to Dihydroxyacetone in Sunless Tanning Products Understanding the Risks. *J Dermat Nurses Asso* **2018,** *10* (1), 11-17.

169.   Garone, M.; Howard, J.; Fabrikant, J., A review of common tanning methods. *J Clin Aesthet Dermatol* **2015,** *8* (2), 43-7.

170.   Gudjonsson, J. E.; Johnston, A.; Dyson, M.; Valdimarsson, H.; Elder, J. T., Mouse models of psoriasis. *J Invest Dermatol* **2007,** *127* (6), 1292-1308.

171.	Gerber, P. A.; Buhren, B. A.; Schrumpf, H.; Homey, B.; Zlotnik, A.; Hevezi, P., The top skin-associated genes: a comparative analysis of human and mouse skin transcriptomes. *Biol Chem* **2014,** *395* (6), 577-591.

172.	Zhou, X.; McCallum, N. C.; Hu, Z.; Cao, W.; Gnanasekaran, K.; Feng, Y.; Stoddart, J. F.; Wang, Z.; Gianneschi, N. C., Artificial Allomelanin Nanoparticles. *ACS Nano* **2019,** *13* (10), 10980-10990.

173.	Fitzpatrick, T. B.; Breathnach, A. S., The Epidermal Melanin Unit System. *Dermatol Wochenschr* **1963,** *147*, 481-9.

174.	Wasmeier, C.; Hume, A. N.; Bolasco, G.; Seabra, M. C., Melanosomes at a glance. *J Cell Sci* **2008,** *121* (24), 3995-3999.

175.	Michaels, A. S.; Chandrasekaran, S. K.; Shaw, J. E., Drug Permeation through Human Skin - Theory and Invitro Experimental Measurement. *Aiche J* **1975,** *21* (5), 985-996.

176.	Rawlings, A. V., Molecular basis for stratum corneum maturation and moisturization. *Brit J Dermatol* **2014,** *171*, 19-28.

177.	Moore, D. J.; Rawlings, A. V., The chemistry, function and (patho)physiology of stratum corneum barrier ceramides. *Int J Cosmetic Sci* **2017,** *39* (4), 366-372.

178.	Watkinson, A. C.; Bunge, A. L.; Hadgraft, J.; Lane, M. E., Nanoparticles Do Not Penetrate Human Skin-A Theoretical Perspective. *Pharm Res-Dordr* **2013,** *30* (8), 1943-1946.

179.	Konrad, K.; Wolff, K., Hyperpigmentation, Melanosome Size, and Distribution Patterns of Melanosomes. *Arch Dermatol* **1973,** *107* (6), 853-860.

180.	Smijs, T. G. M.; Bouwstra, J. A., Focus on Skin as a Possible Port of Entry for Solid Nanoparticles and the Toxicological Impact. *J Biomed Nanotechnol* **2010,** *6* (5), 469-484.

181.	Prow, T. W.; Grice, J. E.; Lin, L. L.; Faye, R.; Butler, M.; Becker, W.; Wurm, E. M. T.; Yoong, C.; Robertson, T. A.; Soyer, H. P.; Roberts, M. S., Nanoparticles and microparticles for skin drug delivery. *Adv Drug Deliver Rev* **2011,** *63* (6), 470-491.

182.	Weigmann, H. J.; Schanzer, S.; Patzelt, A.; Bahaban, V.; Durat, F.; Sterry, W.; Lademann, J., Comparison of human and porcine skin for characterization of sunscreens. *J Biomed Opt* **2009,** *14* (2).

183.	Arnette, C.; Koetsier, J. L.; Hoover, P.; Getsios, S.; Green, K. J., In Vitro Model of the Epidermis: Connecting Protein Function to 3D Structure. *Method Enzymol* **2016,** *569*, 287-308.

184.	Das, L. M.; Binko, A. M.; Traylor, Z. P.; Peng, H.; Lu, K. Q., Vitamin D improves sunburns by increasing autophagy in M2 macrophages. *Autophagy* **2019,** *15* (5), 813-826.